Fire in Tunnel Collaborative Project

FINAL REPORT
February 2021

Submitted by:

Negar Elhami-Khorasani
Assistant Professor

Anthony Tessari
Assistant Professor

Department of Civil, Structural and Environmental Engineering
University at Buffalo

Bruno Goncalves da Silva
Assistant professor

Department of Civil and Environmental Engineering
New Jersey Institute of Technology

External Project Manager:

Harry Capers, Vice President
Arora and Associates, P.C.

In cooperation with

Rutgers, The State University of New Jersey
And
U.S. Department of Transportation
Federal Highway Administration

Disclaimer Statement

The contents of this report reflect the views of the authors, who are responsible for the facts and the accuracy of the information presented herein. This document is disseminated under the sponsorship of the Department of Transportation, University Transportation Centers Program, in the interest of information exchange. The U.S. Government assumes no liability for the contents or use thereof.

The Center for Advanced Infrastructure and Transportation (CAIT) is a Regional UTC Consortium led by Rutgers, The State University. Members of the consortium are Atlantic Cape Community College, Columbia University, Cornell University, New Jersey Institute of Technology, Polytechnic University of Puerto Rico, Princeton University, Rowan University, SUNY - Farmingdale State College, and SUNY - University at Buffalo. The Center is funded by the U.S. Department of Transportation.

TECHNICAL REPORT STANDARD TITLE PAGE

1. Report No.	2. Government Accession No.	3. Recipient's Catalog No.
CAIT-UTC-REG16		

4. Title and Subtitle	5. Report Date
Fire in Tunnel Collaborative Project	February 2021
	6. Performing Organization Code CAIT/University at Buffalo

7. Author(s)	8. Performing Organization Report No.
[1]Nan Hua (https://orcid.org/0000-0002-3046-9331); [2]Anthony Tessari (https://orcid.org/0000-0003-0231-345X); [3]Negar Elhami-Khorasani (https://orcid.org/0000-0003-3228-0097) Chapter 4: [4]Ehsan Mehryaar (https://orcid.org/0000-0002-1036-7987); [5]Bruno Goncalves da Silva (https://orcid.org/0000-0003-2052-2562)	CAIT-UTC-REG16

9. Performing Organization Name and Address	10. Work Unit No.
[1-3]Department of Civil, Structure and Environmental Engineering, University at Buffalo. [4-5]Department of Civil and Environmental Engineering, New Jersey Institute of Technology	11. Contract or Grant No. 69A3551847102

12. Sponsoring Agency Name and Address	13. Type of Report and Period Covered
Center for Advanced Infrastructure and Transportation Rutgers, The State University of New Jersey 100 Brett Road, Piscataway, NJ 08854	Final Report 10/01/2018 – 11/30/2020
	14. Sponsoring Agency Code

15. Supplementary Notes
U.S. Department of Transportation/OST-R
1200 New Jersey Avenue, SE, Washington, DC 20590-0001

16. Abstract
Extreme fire events in tunnels may have catastrophic consequences, which include loss of life, structural damage, and major socioeconomic impacts due to service disruptions. In this report, a traveling fire model for a railway tunnel is established to evaluate the evolution of temperatures considering fire spread between train cars. Uncertainties in the amount of fuel, ventilation velocity, tunnel slope, ignition point, and criteria for fire spread are incorporated to capture distributions of fire temperature and duration in the tunnel. The generated demand fire scenarios are used to quantify the potential damage to a concrete tunnel lining in terms of the volume of concrete that would require replacement after a fire event. A finite element modeling approach is developed to incorporate the effects of concrete spalling on the structural response. Further, realistic soil conditions and overburden pressures are modelled and verified using soil-specific simulation software and analytical solutions. The evolution of moments during the heating and cooling phases of a fire are modelled and the results demonstrate the importance of capturing the cooling phase during both simulation and experimental testing. Small-scale element testing of concrete spalling is performed at the New Jersey Institute of Technology, which considers concrete mixtures with polypropylene (PP) and steel fibers, and demonstrates the effectiveness of the PP fibers. Four large-scale concrete slabs are tested using the large furnace at the University at Buffalo. Three test specimens contain fiber reinforcement, which prevented spalling during testing. The last specimen did not contain fibers, and the specimen experienced significant spalling during the heating phase. Evolution of temperature within the cross section, displacements of the four concrete slabs, and damage in terms of cracking, spalling, and reduced strength are reported. The outcomes of this report provide insight on the likelihood of fire damage to the concrete liner of railway tunnels.

17. Key Words	18. Distribution Statement
Tunnel, concrete liner, fire, damage, spalling, modeling, experiment	

19. Security Classification (of this report)	20. Security Classification (of this page)	21. No. of Pages	22. Price
Unclassified	Unclassified	Total # 150	

Form DOT F 1700.7 (8-69)

Acknowledgments

The authors gratefully acknowledge the Region 2 UTC Consortium led by the Center for Advanced Infrastructure and Transportation (CAIT) at the Rutgers University and the Institute of Bridge Engineering (IBE) at the University at Buffalo for their generous support. Any opinions, findings, and conclusions, or recommendations expressed in this material are those of the authors and do not necessarily reflect the views of the CAIT Region 2 UTC Consortium.

The authors would like to thank Professor Maria Garlock of Princeton University, who served as the project collaborator and provided advice on the technical research approach and the experimental program. The inputs and guidance of Mr. Harry Capers, the primary project stakeholder, are greatly appreciated. The authors thank the other project stakeholders, Mr. Gary English, Dr. Conrad Felice, and Mr. Louis Ruzzi, for their provided insight at different phases of this project.

Table of Contents

List of Figures

List of Tables

CHAPTER 1 INTRODUCTION

Fire hazard is a major threat and can cause severe damages to tunnel structures. The rapid rise of gas temperature exceeding 1000 °C inside a confined tunnel space and the long fire duration due to limited fire-fighting access can result in significant material deterioration and intense heat-reduced concrete spalling. There is a long list of historical tunnel fires, including extreme events with a large number of fatalities, injuries, and significant socioeconomic impacts. On March 24, 1999, a Belgian truck carrying flour and margarine caught fire in the Mont Blanc Tunnel. The fire lasted for 50 hours and affected 900 m of the tunnel, with the crown area mostly damaged [1]. The estimated financial loss of the Mont Blanc Road Tunnel fire was € 392 million (464 million US dollars) [2]. On the 11th of September 2008, a major fire occurred in the Channel Tunnel connecting the UK and France, involving many heavy goods vehicles (HGV) on carrier wagons. After the fire, the concrete tunnel lining required repairs along 650 meters of the tunnel length, and a 20-meter long section of the tunnel was reported to be severely damaged with the maximum damaged depth of 400 mm [1]. The financial loss from the fire was estimated as € 250-286 million (296-339 million US dollars) [2]. Although collapse of a tunnel structure due to fire is not observed in historic events, the serviceability and resilience of the tunnel structure are challenged, as a major fire event could lead to months of downtime and millions of dollars of losses from repair and affected operations.

Tunnel fire has become more of a concern and received a growing attention in the recent decades. On one hand, an increasing density in the transport of goods, especially of flammable materials, increases the amount of potential fuel, and the likelihood for a fast fire spread in the case of a fire within a tunnel space. On the other hand, modern tunnel design uses higher strength concrete and thinner linings. Although the use of high-strength concrete saves cost of materials, it may cause severe spalling and consequently loss of a large fraction of lining sections in the case of a fire. While the historical events identified the disastrous consequences of tunnel fires, the

newly raised concerns associated with modern tunnels further emphasize the need to design tunnels for fire.

There is a relatively large body of literature available on fire propagation and smoke control inside tunnels (as introduced in Chapter 2), as well as relevant provisions on evacuation routes in tunnel spaces to ensure passenger safety [3]. However, less research focus has been placed on damage assessment of tunnel structures due to fire, and there is no available guideline or established methodology to design the tunnel liner for loss of functionality following a fire event.

The procedure to study a structure-fire interactive problem typically includes three steps: (1) determining the fire scenario (temperature-time curve), (2) performing thermal (heat transfer) analysis, and (3) performing structural analysis that considers the thermal load. For the evaluation of fire damage to the tunnel structure, each of the steps requires the analysis of numerous factors and involves many uncertainties. For example, the fire scenario can be influenced by the tunnel geometry, the amount of combustible materials, the ventilation condition during fire, etc. Considering the uncertainties of thermal and mechanical properties of both concrete and steel, as well as the surrounding ground conditions, in step 2 and 3 is not an easy task. While the material-level studies on property reductions at high temperatures are available, the methodology to combine and apply such findings to characterize tunnel fire damages has not been developed.

Meanwhile, engineered solutions to achieve an acceptable fire safety leads to more efficient and cost-effective designs while safety is explicitly verified. The application of a performance-based design (PBD) methodology, for which the benefits have been demonstrated for building applications, can be used in the fire design of tunnels to ensure safe and economic solutions. The PBD framework for tunnel fires should start with the definition of performance objectives (e.g., the level of acceptable damage for a given fire scenario). Hence, developing an understanding of tunnel fire damage, while accounting for the uncertainties in the influencing parameters, would contribute significantly to establishing PBD methodology/guidelines for design of tunnels under fire.

1.1 State-of-the-art review

This section provides a review of the state-of-art of the existing research and guidelines on the fire damage to tunnel structures. An introduction on characterization of tunnel fire scenarios is firstly presented, followed by a summary of existing experimental and numerical studies. Then, the available guidelines on concrete damage assessment of structures are reviewed to provide reference for defining a fire damage assessment methodology specific to tunnels. Finally, the knowledge gaps are identified based on the review.

1.1.1 Tunnel fire scenarios

Understanding the spatial and temporal distribution of temperature inside a tunnel is important for fire damage assessment. The rapid rise of gas temperature in excess of 1000 °C inside a confined tunnel space and the long fire duration due to limited fire-fighting access may lead to severe damage to the tunnel lining and affect the overall structural integrity of the tunnel. A fire scenario describes the evolution of gas temperature over time during a fire event. A tunnel fire scenario is typically characterized by a fast heating rate and a high peak temperature. Although defining a tunnel fire scenario requires inputs from a number of factors and involves a high level of uncertainty due to variation in fuel, ventilation, tunnel geometry, etc., the most common approach in engineering practice today is the application of standard design curves and deterministic procedures. One widely adopted example in the US and Europe is the standard hydrocarbon fire curve, which reaches 1000 °C within a few minutes and keeps increasing through the fire duration. Other fire curves for tunnel fire design include: (1) the modified hydrocarbon curve, developed in France, which has a larger maximum temperature in comparison with the standard hydrocarbon fire; (2) the RWS (Rijkswaterstaat) fire curve, developed in Netherlands, which has a peak temperature of 1350 °C and assumes a worst-case scenario of a petrol tanker fire with a fire load of 300 MW; and (3) the RABT-ZTV curves, developed from a series of test programs such as the EUREKA-499 FIRETUN project in Germany, that reach the peak temperature of 1200°C within 5 minutes [4]. Among the listed design curves,

only the RABT-ZTV curves include a decaying phase and consider car fire and train fire scenarios separately, where the duration of a car fire is 30 minutes shorter than a train fire.

Rather than using standard fire curves, the performance-based design (PBD) method provides improved and more flexible engineered solutions based on a realistic characterization of fire hazard and the quantified fire damage to the tunnel structure. A comprehensive PBD approach requires a clear definition of design objectives, performance criteria, and demonstration of compliance with the required performance objectives. In recent years, the US standards also consider PBD as a valid approach to be used for the fire safety design of a structure. For example, NFPA 502 [5] puts forward PBD criteria for tunnel fires by providing data on fuel load of typical vehicles (passenger car, bus, heavy goods truck, and flammable liquid tank), the requirements for emergency ventilation, and water-based firefighting systems. As part of the National Cooperative Highway Research Program, NCHRP Synthesis 415 [6] introduces PBD of tunnel fires in a standalone section and points out the need for a greater focus on the definition of appropriate fire scenarios dealing with tunnel fire safety. Both of the official documents constitute a step towards a comprehensive PBD framework focusing on roadway tunnels. However, these guidelines do not provide quantified frameworks to calculate the spatial and temporal distribution of fire temperature inside the tunnel, and such guidance on railway tunnels are even less available. There is still a long way to go to establish a comprehensive PBD methodology for tunnel fire scenarios, especially for railway tunnels.

Defining design fire scenarios for railway tunnels requires an understanding of a number of factors and the associated uncertainties, which can be summarized as follows: (1) the tunnel geometry, e.g. tunnel shape, height, width and slope, (2) the variety of car materials, consisting of the car body itself as well as any internal equipment, components, and furnishings, resulting in a wide range of combustible load, (3) ventilation conditions, including the design of fans if they are present in the tunnel, or tunnel location if naturally vented, and (4) fire spread between railcars, which has been observed in real events but has not been well quantified.

Li [7, 8] proposed a widely acknowledged equation (Eq. 1.1) to calculate the maximum temperature of a tunnel fire based on an axisymmetric fire plume theory, which was calibrated

using a large set of experimental data. Heat release rate, ceiling height, fire source dimension, and ventilation velocity were identified as the main parameters influencing the maximum temperature.

$$\Delta T_{max} = \begin{cases} 17.5\dfrac{Q^{2/3}}{H_{ef}^{5/3}}, & V' \le 0.19 \\ \dfrac{Q}{V b_{f0}^{1/3} H_{ef}^{5/3}}, & V' > 0.19 \end{cases}, \Delta T_{max} \le 1350\ ^{\circ}C \qquad (1.1)$$

$$V' = V \Big/ \left(\frac{gQ}{b_{f0}\rho_0 c_p T_0}\right)^{\frac{1}{3}}$$

Where b_{f0} is the radius of the fire source (m), g is the gravitational acceleration (m/s^2), H_{ef} is the vertical distance between the bottom of fire source and tunnel ceiling (m), c_p is the heat capacity of air (kJ/kg K), Q is the heat release rate (kW), T_0 is the ambient temperature (K), ΔT_{max} is the maximum temperature (with reference to the ambient temperature) beneath the ceiling (K), V is the longitudinal ventilation velocity (m/s), V' is the dimensionless ventilation velocity, and ρ_0 is the ambient density (kg/m^3).

The equation was obtained from a single fire plume model and works well for pool fires and single-vehicle fires. However, the equation may no longer accurately represent reality when accounting for fire spread, given that the ignition conditions can be complex when extensive spreading occurs, and the energy released by each train car does not necessarily reach its peak at the same time as the neighboring cars. Experimental data on fire spreading between train cars is also limited because of the inherent dangers involved during such tests. Considering all the challenges and uncertainties of tunnel fires, a probabilistic-based approach is needed to capture the range of potential scenarios.

While experimental studies are necessary for model validation and to capture the real response of engineered systems, they are costly in terms of both monetary value and time to successful execution. Numerical modeling can be used to run a series of simulations with a range of input parameters, the results of which can be used in making design recommendations and assisting with the decision-making process. A number of computational fluid dynamics (CFD) software packages are available to study temperature-time evolution of fire inside a tunnel. While

a CFD simulation usually involves a relatively high computational cost, it enables the possibility to capture the fire spreading phenomenon inside tunnels and to provide spatial temperature distributions. Due to the complexity of CFD modeling, the method has not been widely adopted for designs.

1.1.2 Damage assessment of tunnel fires

Historical tunnel fires have confirmed the need to minimize the downtime following a fire event as well as the resulted economic loss. Thus, fire damage to the tunnel structure should be characterized for adjusting the fire protection design of the tunnel liner and achieving an optimum design. Although a framework, as detailed as those for buildings, is not available, scattered experimental and numerical studies for tunnel fire damage assessment have provided insight to the problem.

(i) Experimental studies

Existing experimental studies are mostly focused on the heat-induced spalling phenomenon. Heat-induced spalling is a major and common issue for fire performance of concrete structures, and is defined as the violent ejection of pieces from the surface of concrete elements when exposed to rising temperatures. A combination of factors, such as concrete mixture, moisture content, external loading, geometry of the element or the whole structure, as well as the rate and duration of heat exposure, can influence spalling of concrete at high temperatures. However, a consensus has not been reached as of which parameter governs this mechanism, if indeed it is only one parameter or a combination of different interrelated parameters. Moreover, it has been experimentally proven that adding a small amount of polypropylene (PP) fibers in the concrete mix could effectively reduce or prevent heat-induced spalling [9-12], but the modeling process of the mechanism is not well understood. Meanwhile, no finite element software has built-in functions for heat-induced spalling prediction to date.

Given the numerous influencing factors on the spalling process, full- or large-scale experiments provide the best support for design of new tunnels and help the research community

understand heat-induced concrete spalling. Experiments conducted on full-scale tunnel segments or slabs in the last two decades are listed in Table 1.1, most of which served as fire resistance tests during the design phase of tunnel projects.

Table 1.1 Recent full-scale fire tests on tunnel segments/slabs

Ref.	Country	Test Specimen Dimension	Test Fire Curve	Restraint and Loading Condition	Major Results/Conclusions
[13]	Austria	Length = 1.2 m Width = 0.8 m Thickness = 0.3m (flat)	RWS/ ISO 834	Restrained, unloaded	Spalling occurs gradually, constant spalling rates (mm/min) are reported for each test. The time when spalling starts is essentially dependent on the heating rate in the furnace within the first few minutes. Spalling rate increases with increasing compressive stress and moisture content.
[14]	Turkey	Length = 1.5 m Width = 1.1 m Thickness = 0.32m (curved)	HC	Unrestrained, unloaded	Average spalling depth (20mm) and aggregate colorization depth (80-90mm) are observed from core samples taken after the test. The loss of compressive strength is about 30% and 15% on average for the top and bottom parts when compared to the compressive strength of cores taken from reference specimen, after four hours of exposure to hydrocarbon fire.
[15, 16]	China	Length = 5 m Width = 1.2 m Thickness = 0.35 m (curved)	ISO 834	Restrained, loaded	Spalling mainly occurs between 6 to 20 min. Maximum spalling depth: 6-51 mm, spalled area: 13.1%-55.7%. Investigated post-fire performance by loading the specimen after cooling.
[17]	UK	Length = 1.5 m Width = 0.75 m Thickness = 0.3 m (flat)	RABT	Restrained, unloaded	Polypropylene (PP) fiber reduces spalling more effectively than polyvinyl alcohol (PVA) fibers.
[18]	Germany	Length = 1.84 m Width = 1.22 m Thickness = 0.3 m (flat)	RABT	Unrestrained, unloaded	A spalling depth of 100mm is reported.

[19]	France	Length = 4.1 m Width = 1.7 m Thickness = 0.4 m (flat)	HC	Unrestrained, unloaded	Intense spalling is observed among all the experiments. The almost constant and very high spalling rates are mostly between 5 to 7 mm /min. The result can be partly explained by the silica fume addition and the high-water content of the mix.
[20]	Australia	Length = 1.55 m Width = 1.55 m Thickness = 0.3 m (flat) & Length = 3.45 m Width = 1.7 m Thickness = 0.3 m (curved)	RABT	Restrained, loaded	The average spalling depth is 22 mm within the central area of 800 mm x 800 mm, whilst the average spalling for the entire surface exposed to fire is approximately 11 mm. Concrete is more susceptive to spalling when significant compressive stress is applied. The fly ash-based blended concrete has less spalling when subjected to fire.

Note: HC stands for the Hydrocarbon fire curve.

When conducting spalling tests, except for the material properties and scale, the loading protocol and constraint levels should also be designed with caution to imitate real conditions of a tunnel segment in situ. Only two of the experiments listed in Table 1.1 considered the influences of both constraint and loading conditions. More fire spalling tests of intermediate- and small-scale concrete elements are available compared to real-scale tests. Despite the small-scale, they also provide valuable insight, and facilitate repetition and variations in test parameters. A rich set of collections can be found in the proceedings of a bi-annually held workshop, the "International Workshops on Concrete Spalling due to Fire Exposure" [21], which publishes recent research results to advance the understanding of spalling under various conditions.

(ii) Numerical studies

Once a credible demand fire scenario is determined, temperatures within the sections can be obtained by completing heat-transfer analysis. Advanced thermal and structural analysis, performed with finite-element software packages such as Abaqus and SAFIR [22], can help determine the residual capacity of the damaged structure. Limited numerical studies on tunnel

performance under fire are available in the literature, focusing on 2D tunnel structural models. The following paragraphs present a summary of these studies.

In 1999, Ulm et al. [23] performed a 2D finite-element analysis of the Channel Tunnel rings exposed to a 10-hour ISO 834 fire. The study developed a material model for concrete that accounts explicitly for the dehydration of concrete and its cross-effects with deformation and temperature. The chalk substratum was modeled with continuum elastic elements. The aim of this study was to find out the reason for the intense spalling after the 1996 Channel Tunnel fire. It was concluded that the initiation of thermal spalling was related to the chemo-plastic softening behavior at the concrete constitutive material level. It was also shown that reinforcement on the cold-side, as well as steel fiber reinforcement, in the tunnel rings may increase the risk of thermal spalling.

In 2002, Schrefler et al. [24] carried out a 2D simulation of a concrete horseshoe-shape tunnel using heat fluxes as thermal input. A concrete material model was proposed, which considered concrete as a porous material and accounted for both the mechanical damage (cracks) and thermo-chemical damage describing the material degradation at elevated temperatures (mainly due to micro-cracking and cement dehydration). The results of this analysis included mechanical and thermo-mechanical damage depth of cross-sections located at three different heights of the tunnel. Soil and spalling behavior were not investigated in this study.

In 2005, Savov et al. [25] developed a 2D beam-spring model to assess the stability of a shallow reinforced concrete tunnel under fire. The tunnel model was adapted from a circular tunnel, the Lainzer tunnel in Austria. The stiffness and strength degradation functions of both concrete and steel were adopted from standards. In order to assess the influence of spalling on the stability of the tunnel, four spalling scenarios characterized by different final spalling depths were considered in the study. As the result shows, one extreme spalling scenario (where 75% of the total lining thickness spalled) resulted in the collapse of the tunnel after a three-hour fire. In 2008, the same group published another paper [26], focusing on an updated coupled thermo-hydro-chemical analysis by simulating the heat and mass transfer in concrete under fire loading.

Results showed that the consideration of mass transport within the coupled analysis led to lower thermal loading of the tunnel lining compared to the uncoupled thermal analysis.

In 2009, Feist et al. [27] numerically evaluated the load-carrying behavior of a double-track, cut-and-cover railway tunnel with a double-box section. The shallow RC tunnel model was investigated under 90 min of modified hydrocarbon fire exposure. The 2D structural model was constructed using continuum elements. The temperature-dependent thermal and mechanical material properties of the concrete and reinforcing steel were accounted for in the transient thermal and mechanical analyses. A concrete model using the combination of plasticity and damage theory was proposed and validated using fire tests of plate-type specimens.

In 2009, Caner et al. [14] analytically investigated structural fire safety of a circular tunnel lining, using a 2D beam-spring model. The study investigated a total of 36 tunnel sections under RWS and hydrocarbon fires for four hours, varied by tunnel buried depth, inner radius, lining thickness, and water loads. A gradual concrete spalling function was built in the model where spalling trigger was a function of the total strain of each lining layer across its thickness. The study concluded that the tunnel had better fire endurance in soft soils than in stiff soils, and the crown sagging was either neutralized or reversed during the fire. Therefore, bending and shear forces were never significant compared to the axial forces induced by the fire.

In 2013, Lilliua and Medab [28] analyzed a typical TBM (tunnel boring machine) constructed tunnel, built in soft soil, with the finite element program DIANA. In their analysis, the excavation of tunnel was first modeled to predict stresses in the lining due to the soil pressure, and a fire load was applied afterward. The reinforced concrete tunnel was modeled in 2D, under the assumption of plane strain, and subjected to the RWS fire curve for two hours. The temperature-dependent nonlinear material properties were defined in DIANA. The results showed that, despite cracking and yielding of reinforcements, structural stability of the tunnel was ensured up to 120 minutes of the fire duration.

In 2019, Sun et al. [29] performed a stability analysis of a fire-loaded shallow tunnel using a thermo-hydro-chemo-mechanical model, following the same approach as [26]. This study presented a “stress vs strength” criterion for determination of the initiation of spalling. The study

concluded that, although fire loading exhibited very limited influence on the stability of the tunnel, the stability of the tunnel could have been greatly affected if spalling had occurred.

In summary, various finite element codes were developed to capture the complex thermal and mechanical behavior of tunnel structures under fire. Except for the fire load, other service loads, such as water, earth pressure (vertical and horizontal), and surcharges are also captured in most of the models. The soil-structure system is modeled using two methods: (1) beam-spring model, where the tunnel is modeled by a number of connected beam elements while the surrounding soil is modeled as a set of springs, (2) continuum method, where the tunnel structure and the soil are both modeled as continuum solid elements. The tunnel stability is generally maintained according to the results of simulations in existing studies. However, nearly all of the studies adopt the standard fire curves, which would not reflect a realistic fire scenario and consequently the assessment results may not provide true estimates of damage. Further, soil properties under elevated temperatures and their influence on the tunnel structure are not studied in detail. Modeling of concrete spalling is still a subject of research. Post-fire assessment frameworks, such as residual deformation and capacity, are not well established.

1.1.3 Post-fire damage assessment procedures

The aim of post-fire assessment is to identify proper repair methods and decide whether or not a structural member or the whole structure needs to be demolished. The outcome of an assessment should include an estimation of the extent and degree of damage to each member, such as the spalled/deteriorated depth of a cross-section, the maximum temperature reached in fire-affected areas, and the residual strength of concrete. Identifying proper damage levels and a corresponding repairing classification system are needed to set up performance objectives for design and assessment of tunnels under fire.

Since no detailed damage assessment framework is available for tunnel structures, this section includes a review of fire damage assessment and repair techniques, methods, and guidelines as available for general reinforced concrete structures. Two major official documents developed in the UK [30] and the US [31] are referenced in this section.

As recommended by the Concrete Society [30], a general fire damage assessment framework for fire-damaged structures should follow three major steps: (1) carry out preliminary and on-site assessment of the structure to determine the extent of damage; (2) determine the residual strength of material samples and confirm depth of fire-damage; (3) determine structural capacity of members and select appropriate repair methods. A combination of following methods is typically used to complete the three steps.

(i) Visual inspection and hammer sounding

Visual inspection provides recordings of features such as concrete color, concrete spalling, cracking, surface crazing, distortion, deflections, and collapse. A small hammer may be used to conduct a tapping survey on concrete surfaces to detect concrete damage. According to the UK concrete society [30], a "ring" from the hammer tap indicates sound concrete, while a "dull thud" indicates weak concrete.

The surface appearance of concrete provides engineers the first indication of which elements require cosmetic repairs, and which, if any, will need further assessment. The color of concrete can change because of heating, which is apparent upon visual inspection. Concrete shows pink/red discoloration due to oxidation of ferric salts in aggregates above 300 °C, also indicating a strength loss of the material [30, 31].

Heat-induced spalling is a major and common issue for fire performance of concrete structures [32]. Spalling conditions range from localized popping-off of small and thin chips to dramatically breaking away of large pieces of concrete and exposing reinforcement. Spalling also enables the fire frontier to propagate deeper into the concrete and thus increases the deteriorating depth. The visual inspection after fire should include an assessment of spalling, documented as the spalling depth across the affected area, as well as the total weight/volume of spalled concrete.

(ii) Non-destructive testing (NDT)

While visual inspections serve as the most direct assessment, numerous NDT techniques are used to provide a more reliable evaluation of damage. The NDT method is not only used for fire damage assessment, but also applies to other disciplines, such as corrosion detection of

embedded rebars. Details of implementation and reliability of more than 20 applicable NDT methods are reported in the ACI 228.2R [33]. The mostly used NDT methods for fire damage assessment are the rebound (Schmidt hammer) test and the ultrasonic pulse velocity (UPV) test [30, 31, 34].

The Schmidt hammer test provides a measure of the surface hardness of concrete, which was developed by a Swiss engineer, Ernst Schmidt in 1948 [35]. A guided procedure of this method is available in the ASTM C805 [36]. Although there is little apparent theoretical relationship between the rebound number and concrete strength, empirical correlations, with some limitations, exist between the two. The results of the rebound test are influenced by smoothness of the test surface, size and shape of the test specimens, type of aggregate, etc. [35]. Due to uncertainties, the results of rebound hammer tests are not always consistent; however, the test is widely used because of its common availability and ease of application [30].

The UPV method can be used to estimate the residual concrete strength in situ. A guided procedure of this method is available in the ASTM C597 [37]. The method also requires a flat surface, and as such, only applicable to unspalled elements [30, 31]. Since the UPV method provides results based on the ultrasonic pulse transmission time, the assessed damage would be an average estimate across the section depth. This measure is recommended as a relative measurement, i.e. based on a comparison of damaged and undamaged parts of the structure to facilitate mapping of the damaged areas [34].

The NDT techniques are fast growing these days as a result of technology developments across multiple disciplines. For example, digital image processing can be used to map cracks on a concrete surface after cooling [38], machine learning algorithms and image texture analyses can be adapted to automatically detect concrete spalling [39], and short pulse radar method using electromagnetic waves can be used instead of the UPV method [34]. More details on NDT methods can be found in the NDT & E International Journal, which focuses on developments in nondestructive testing.

(iii) Sampling of material and subsequent laboratory testing

Samples of damaged material, together with undamaged references, may be removed for laboratory investigation. Concrete samples are typically obtained by drilling of cores or by careful extraction of lump samples [40]. Concrete core samples can be taken for petrographic examination and compression tests. The petrographic analysis is mainly concerned with the damage and property change of concrete at high temperatures, i.e., depth of microcracking, paste alteration (color change and strength softening), and carbonation. The petrographic analysis should be conducted in accordance with the ASTM C856 [41].

(iv) Damage and repair classifications

Coded damage classification criteria in national and international standards have two major benefits: (1) for in situ repair, the degree of damage and levels of repair to various elements/locations of the structure can be effectively evaluated, (2) for performance-based fire design of tunnel structures, a basis is provided for quantification of performance objectives, which can be correlated to tunnel resilience against fire.

Two major standard documents, from the Concrete Society and the *fib* [30, 31], provide fire damage classification for building structures, where the one by the UK concrete society [30] also includes a categorized repair requirement for the defined damage classes. Table 1.2, Table 1.3, and Table 1.4 provide a summary of the available guided damage classifications and repair requirements (only the information related to reinforced concrete structures is presented here).

Table 1.2 Fire damage classifications of concrete structures according to *fib* [31]

Class	Characterization	Description
1	Cosmetic damage, surface	Characterized by soot deposits and discoloration. In most cases soot and color can be washed off. Uneven distribution of soot deposits may occur. Permanent discoloration of high-quality surfaces may cause their replacement. Odors are included in the class (they can hardly be removed, but chemicals are available for their elimination).
2	Technical damage, surface	Characterized by damage on surface treatments and coatings. Limited extent of concrete spalling or corrosion of unprotected metals. Painted surfaces can be repaired. Plastic-coated surfaces need replacement or protection. Minor damages due to spalling may be left in place or may be replastered.

3	Structural damage, surface	Characterized by some concrete cracking and spalling, some deformation of metal surfaces or moderate corrosion. This type of damage includes also class 2 damages, and can be repaired in similar ways.
4	Structural damage, cross-section	Characterized by major concrete cracking and spalling in the web of I-beams and deformed flanges.
5	Structural damage to members and components	Characterized by severe damages to structural members and components, with local failures in the materials and large deformations. Concrete constructions are characterized by extensive spalling, exposed reinforcement and damaged compression zones. Mechanical decay in materials may occur as a consequence of the fire. Class 5 damages usually will cause the dismissal of the structure.

Table 1.3 Fire damage classifications according to the Concrete Society [30]

Class	Element	Surface appearance of concrete			Structural condition			
		Condition of plaster/ finish	**Color**	**Crazing**	**Spalling**	**Exposure and condition of main reinforcement**	**Cracks**	**Deflection/ distortion**
0	Any	Unaffected or beyond extent of fire						
1	Column	Some peeling	Normal	Slight	Minor	None exposed	None	None
	Wall							
	Floor							
	Beam					Very minor exposure		
2	Column	Substantial loss	Pink/ red	Moderate	Localized to corners	Up to 25% exposed, none buckled	None	None
	Wall				Localized to patches	Up to 10% exposed, all adhering		
	Floor							
	Beam				Localized to corners, minor to soffit	Up to 25% exposed, none buckled		
3	Column	Total loss	Pink/ red Whitish grey	Extensive	Considerable to corners	Up to 50% exposed, not more than one bar buckled	Minor	None
	Wall				Considerable to surface	Up to 20% exposed, generally adhering	Small	Not significant
	Floor				Considerable to soffit			

	Beam				Considerable to corners, sides, soffit	Up to 50% exposed, not more than one bar buckled		
4	Column	Destroyed	Whitish grey	Surface lost	Almost all surface spalled	Over 50% exposed, more than one bar buckled	Major	Any distortion
	Wall					Over 20% exposed, much separated from concrete	Severe and significant	Severe and significant
	Floor							
	Beam					Over 50% exposed, more than one bar buckled		

Table 1.4 Repair classifications according to the Concrete Society [30]

Class of damage	Repair classification	Repair requirements
0	Decoration	Redecoration if required
1	Superficial	Superficial repair of slight damage not needing fabric reinforcement
2	General repair	Non-structural or minor structural repair restoring cover to reinforcement where this has been partly lost
3	Principal repair	Strengthening repair reinforced in accordance with the load-carrying requirement of the member. Concrete and reinforcement strength may be significantly reduced requiring check by design procedure.
4	Major repair	Major strengthening repair with original concrete and reinforcement written down to zero strength, or demolition and recasting

The above tables provide guidance for fire damage assessment practices of reinforced concrete building structures. Different extents of fire damages are characterized using concrete cracks, color, crazing and spalling, reinforcement exposure condition, deformation of structural members, etc. The corresponding repair requirements can be related to estimating the time of service interruptions, as well as evaluating the resilience of the structure subjected to fire.

1.1.4 Knowledge gaps

Based on the provided review on fire damage assessment of tunnels, the knowledge gaps are identified and summarized into the following three categories: (1) assessment methodology, (2) framework for performance-based design, and (3) incorporation of uncertainties.

(i) Assessment methodology

The existing studies generally focus on extreme fire demands by using the standard fire curves as the input temperature. The potential damage to tunnel liner, caused by smaller-scale or more realistic fires are not well-investigated. Intermediate-scale fires also lead to deformations that could, for example, cause cracking on the back side of the tunnel lining where inspection is not possible, and long-term corrosion due to cracking could be an issue.

Tunnel linings are generally subjected to various loads including self-weight, vehicle load, soil, water pressure, surcharges, and influences from adjacent foundation works. Moreover, tunnels with different shapes of cross-sections (circular, horseshoe, rectangular, etc.) have complex and varied internal force distributions under a combination of thermal and mechanical loads. Although the material deterioration of concrete and steel at elevated temperatures have been largely investigated using small-scale tests, there is no established methodology to evaluate residual capacity and serviceability of tunnels after fire.

No specific guideline for tunnel fire damage assessment is currently available. Although some findings from building fires can be adapted for this application, the fire rate and intensity, classification of fire damage, and repair techniques are not necessarily the same. For example, corner spalling is commonly found in fire-damaged beams and columns in buildings, however, this does not hold true for tunnel segments. Finally, the assessment to re-open a tunnel after a fire is mainly based on ad hoc procedures.

(ii) Framework for performance-based design

Since tunnel stability has not been identified as a major issue based on most of the historic fire events, performance-based fire design of tunnels, focusing on quantifying the damage, downtime, and the corresponding losses, is needed to achieve more cost-effective designs. An

initial framework [42] can be adapted from other fields and applications; however, a number of factors, from fire scenario to structural behavior, have not been carefully investigated and incorporated in the analyses. Very limited studies or official documents provide references on damage classes, acceptable thresholds for design, and performance objectives.

(iii) Incorporation of uncertainties

Deterministic approaches, and the application of standard fire curves, are widely used in the design and assessment procedures. However, design or assessment of tunnel structures under fire involves a large level of uncertainty at multiple levels, such as the fuel type and amount, ventilation conditions, thermal and mechanical properties of concrete and steel reinforcement, heat-induced spalling, geologic conditions, applied load at the time of fire, etc. Neglecting these uncertainties will lead to unrealistic results or not capturing the full spectrum of potential outcomes.

1.2 Objective and scope

The objective of this report is to establish a scenario-based assessment methodology to quantify fire damage to tunnel lining considering soil-liner interaction. The research outcomes are used to make recommendations for design or assessment of structural fire resistance of tunnels given a fire demand and considering performance requirements. In particular: (1) a range of fire scenarios for passenger railway tunnels are simulated to characterize the spatial and temporal distributions of fire temperature within the tunnel considering uncertainties in fuel and fire spread, (2) a methodology is developed to quantify fire damage to the tunnel concrete lining and evaluate structural stability of the tunnel section taking concrete spalling into account, and (3) results of fire experiments on four loaded and restrained reinforced concrete slabs are reported, which provide insight on the level of fire damage and can be used for model verification. Parts of this report, such as the studied fire scenarios, focuses on passenger railway tunnels, while the developed methodology can be expanded and applied to other tunnel types.

The outcomes of this study can be used to make recommendations and propose design guidelines for structural fire resistance of tunnels based on performance requirements, such as acceptable downtime duration or repair cost for a given fire demand. The proposed framework can be further integrated within probabilistic risk-assessment methods to guide the design of fire protection systems to improve the life-long serviceability of concrete lining and resilience of a tunnel structure.

1.3 Outline of the report

Based on the defined objective, the following report is organized in six chapters:

Chapter 2 "Tunnel fire scenarios": establishes a methodology to investigate the uncertainties of tunnel fire scenarios through a series of computational fluid dynamics simulations.

Chapter 3 "Damage assessment": proposes a framework to quantify concrete damage due to fire, considering influences of heat-induced spalling.

Chapter 4 "Experimental investigation of heat-induced spalling of concrete": investigates heat-induced spalling behaviors of concrete mixed with polypropylene or steel fibers using intermediate-scale specimens.

Chapter 5 "Experimental study on fire damage of reinforced concrete slabs": reports experimental results of fire damage to four loaded and restrained reinforced concrete tunnel slabs.

Chapter 6 "Conclusions and recommendations": provides a summary of research findings, conclusions, and recommendations.

CHAPTER 2 TUNNEL FIRE SCENARIOS

The first step in the design or assessment of a tunnel structure subjected to fire is to define the fire scenario. The tunnel fire scenario describes the evolution of gas temperatures over time during a fire event. Although the procedure of defining the fire scenario involves a high level of uncertainty due to variation in fuel, ventilation, tunnel geometry, etc., the design fire curves currently being used are deterministic [4], which do not consider the fire duration, spread of fire within the tunnel, and the unique environmental conditions during a tunnel fire. Limited studies are available in the literature on quantifying uncertainties in tunnel fire demand (e.g., heat release rate) [43-45]; however, the uncertainty in temperature-time evolution of a tunnel fire has not been investigated. Meanwhile, the evolving spatial distribution of fire temperatures within the tunnel space has not been widely studied, which brings difficulties to obtain a realistic quantification of fire damages to the whole structure.

Characterizing realistic fire scenarios are also motivated by the compelling need to develop a performance-based fire design (PBD) framework for tunnel structures. The performance-based methodology requires a better understating of influencing factors and considerations of uncertainties, and allows for more innovative and cost- effective designs. The concept of PBD was first developed in earthquake engineering and has been adopted by other disciplines, such as wind engineering. However, a framework for performance-based fire design (PBFD) has not been well established while some progress has been made on PBFE for building structures. Hence, there is a necessity to strengthen the knowledge on tunnel fire scenario for implementation in PBFD process of infrastructures.

This section begins with a discussion of the key parameters that influence a railway tunnel fire scenario, collects available experimental data for relevant parameters, and quantifies uncertainties in said parameters. A series of railway tunnel fire scenario, considering fire spread between train cars, are then studied. The numerical simulations are conducted in Fire Dynamics

Simulator (FDS), a computational fluid dynamics (CFD) software package developed by the National Institute of Standards and Technology [46]. The use of FDS, a high fidelity CFD tool, in a probabilistic context with repeated sampling requires significant computational power to arrive at an unbiased approximation of a metric of interest. Considering the computational cost of the simulations, a total of 540 passenger railway tunnel fire scenarios are simulated by varying ventilation velocities, amount of fuel, tunnel slopes, starting ignition location, and ignition criteria for the fire spread. The resulting temperature-time curves are standardized, and the statistics of the fire curves are reported. The results provide insight on the overall trend in the obtained fire curves over time and space. The spatial distribution of fire temperatures is studied to reflect location-dependent fire damages to the lining.

2.1 Influencing parameters on fire scenario

To define realistic demand fire scenarios, the following steps will be completed to understand and characterize temporal and spatial distributions of temperature in railway tunnel fire events:

Step 1: Determine the major parameters influencing a railway tunnel fire scenario.

Step 2: Collect experimental data (if available) or identify a practical range for parameters that influence the fire scenario.

Step 3: Assign an appropriate probability distribution function to each parameter to quantify associated uncertainties.

Step 4: Generate random realizations for each parameter and simulate a fire scenario for a given set of inputs.

Step 5: Aggregate and process the results to obtain the potential range of fire temperature-time curves within the tunnel to guide the design process.

A fire event inside a tunnel is primarily influenced by the fire size (i.e., energy released), ventilation conditions, tunnel geometry, and characteristics of fire spread [47]. The rest of this section will discuss each parameter in detail and quantify the associated uncertainties.

2.1.1 Tunnel geometry

The geometry of tunnel section affects the heat feedback to the burning materials as well as the available amount of oxygen for combustion. A series of studies have focused on the influence of tunnel height, width, and slope on the fire dynamics and smoke movement by conducting reduced-scale experiments [48-51].

(i) Cross-sectional geometry

Considering the high computational cost of the FDS analysis, all the simulations in this report are based on a prototype railway tunnel cross-section in the US. The geometry of the prototype cross-section is adapted from the Howard Street Tunnel [52, 53] in Baltimore, Maryland, which serves as an integral part of the CSX operations on the eastern coast of the US. As shown in Figure 2.1, the cross-section is horseshoe-shape, 6.7-meter tall and 8.2-meter wide. The real Howard Street Tunnel was built in 1895 and is made out of a thick masonry section. In this study, it is assumed that the tunnel is instead made of concrete with a thickness of 0.3 m to reflect a modern design. The adopted tunnel cross-section for the prototype is based on the previous survey of geometries in the CSX and Amtrak tunnels [54, 55]. Among the seven investigated rail tunnels (Long Dock tunnel, Virginia Avenue tunnel, Patterson Viaduct tunnel, Howard Street tunnel, Henryton tunnel, B&P tunnel, and the East River Mountain tunnel), six are 6 - 7 m high, and all are 7.9 - 9.1 m wide.

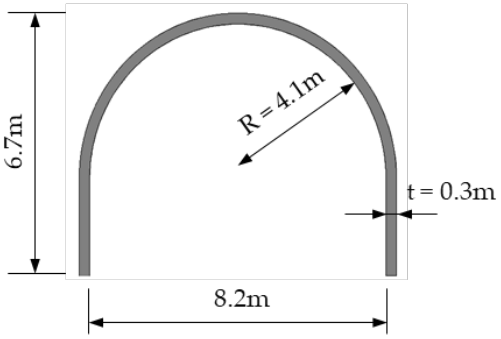

Figure 2.1 Cross-section of the prototype tunnel (adapted from [52])

(ii) Tunnel slope

The tunnel slope, as another geometric parameter, affects the buoyancy force of the smoke flow and back-layering length, and consequently alters the fire demand by influencing ventilation [49, 50]. Three different tunnel slopes are considered in this study to investigate the influence of slope on fire gas temperature: upward 2.2%, downward 2.2%, and zero slopes. The selected values cover the range of practical and allowable slopes: 2.2% slope corresponds to the steepest section of the Cascade Tunnel in Washington State, which serves both passenger and freight trains.

2.1.2 Heat release rate

Fire size in tunnels is typically characterized using the heat release rate (HRR) evolution over time. The HRR describes the rate of energy released during a fire and reflects the magnitude and development of a fire. For train fires, HRR largely depends on the combustion load of carriages while it can also be influenced by the tunnel geometry, ventilation conditions, and the fire propagation rate [47]. The heat feedback of the burning train in a tunnel fire tends to be more effective than that of an open fire due to the confined nature of the tunnel. As a result of the confined enclosure, train carriages burn more intensely in tunnels, leading to a rapid increase and high peak of the HRR. Carvel et al. [56, 57] concluded that the HRR of a fire within a tunnel increases by a factor of 4 compared with that of the same material burning in an open setting.

Although the combustion load of a passenger train car may be more moderate when compared to freight cargo, a variety of train body types, geometry of windows and openings, and the amount of combustible material in the interior introduce a large uncertainty in determining the load [58]. Several large-scale test programs have been conducted worldwide to measure the HRR of passenger railcars [59-63]. The measured HRRs as a function of time are presented in Figure 2.2.

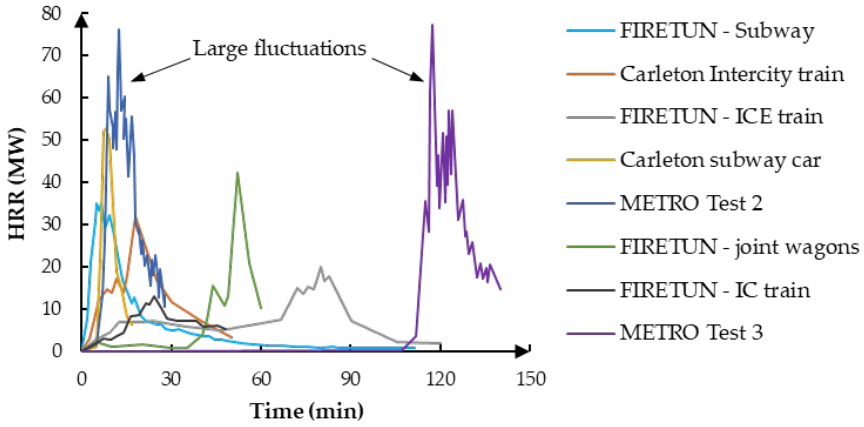

Figure 2.2 Measured HRR for passenger railcars (adapted from [59-63])

Figure 2.2 shows that the HRRs obtained from experiments vary significantly. The first set of tests are from the EUREKA 499-FIRETUN program [61], which included four types of passenger rail and metro cars: (1) two joint half-railcars with half steel and half aluminum bodies, (2) a German Intercity-Express (ICE) railcar, (3) a German Intercity (IC) railcar, and (4) a German subway car. The two tests conducted at Carleton University [62] reported the HRR histories of an intercity railcar and a subway train car. The SP Institute METRO project [60] reported the HRR of two Swedish X1 commuter trains, where one was an original X1 carriage with combustible wall linings (Test 2) and the other was a modified X1 carriage with non-combustible linings (Test 3). The ventilation velocity in these experiments varied from 0.5 m/s to 8 m/s. The data shows that the peak HRR of a passenger carriage ranges from 10 to 60 MW, taking into account the large fluctuations at peak values (for example the absolute peak HRR for METRO Test 2 in Figure 2.2 is 77 MW, while the average peak HRR is taken as 60 MW considering the fluctuation around the peak value).

In order to study and quantify the variability in the HRR curves, the experimental measurements are idealized using a standard curve fit with t-squared growth rate, a plateau, and a linear decaying rate (Figure 2.3). The eight curves in Figure 2.2 are transformed to a set of standard curves shown in Figure 2.3, and are characterized with the four parameters of a, HRR_{max}, t_{dur}, and b, where a and b define the growth and decaying rates, HRR_{max} is the maximum value of the HRR, and t_{dur} specifies the length of HRR plateau. The area under the originally measured and fitted standard curves is kept approximately the same to ensure an equivalent total energy. Considering the large fluctuations in the experimental results, the HRR_{max} is calculated as the average of peak values that are within 70% of the maximum HRR. Similarly, the duration of HRRmax plateau is determined as the time period for which the measured HRR undergoes fluctuations within 70% of the maximum HRR. The growing and decaying rates, a and b, can then be defined knowing the maximum HRR and its duration, the total duration, and the total energy released in each HRR curve. It is notable that the flashover in METRO Test 3 was delayed by 119 minutes due to the aluminum lining of the tested train car. For the purpose of standardization, the start time of this particular curve is taken as the time the fire starts to grow (i.e., at 119 minutes). The four parameters for the fitted standardized HRR curves to the experimental data are summarized in Table 2.1.

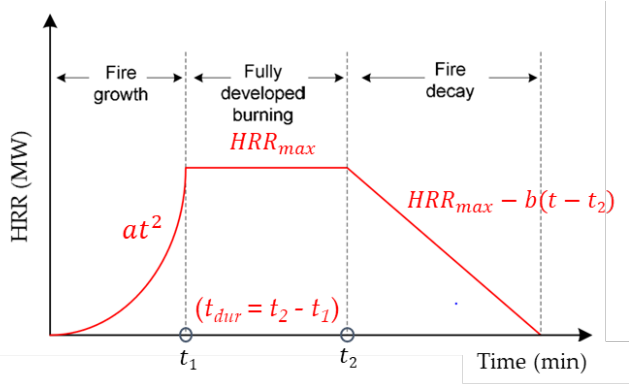

Figure 2.3 Idealized HRR curve as a function of time

Table 2.1 A summary of the HRR curve parameters of Figure 2.3 when fitted to the experimental data of Figure 2.2

Full-scale tests	a	HRR_{max} (MW)	t_{dur} (min)	b
FIRETUN - Subway	1.494	33	4.5	0.802
Carleton Intercity train	0.207	25	10.0	0.748
FIRETUN - ICE train	0.003	17	11.0	0.648
Carleton subway car	0.931	51	2.0	5.960
METRO Test 2	0.775	60	7.9	4.541
FIRETUN - joint wagons	0.370	30	10.0	3.333
FIRETUN IC train	0.037	10	10.2	0.305
METRO Test 3	0.632	57	7.5	2.650

After studying a series of distributions (including Normal, Lognormal, Gamma, Logistic and Weibull distributions), it was concluded that the scaled Beta distribution provides an acceptable fit to the four parameters to quantify the uncertainty. The Beta distribution is flexible, bounded, and provide a description for different types of data. The choice of Beta distribution permitted application of the same distribution type to all the parameters. Figure 2.4 shows the cumulative distribution functions (CDF) of the scaled Beta distributions for the four parameters under study. The range and shape parameters (α, β) of the scaled Beta distributions are presented in Table 2.2. The fitted distributions are based on eight data points only (from the 8 experiments); the distribution types and/or parameters can be updated in future upon availability of more data from large-scale experiments.

Figure 2.4 shows the cumulative distribution functions (CDF) of the scaled Beta distributions for the four parameters under study

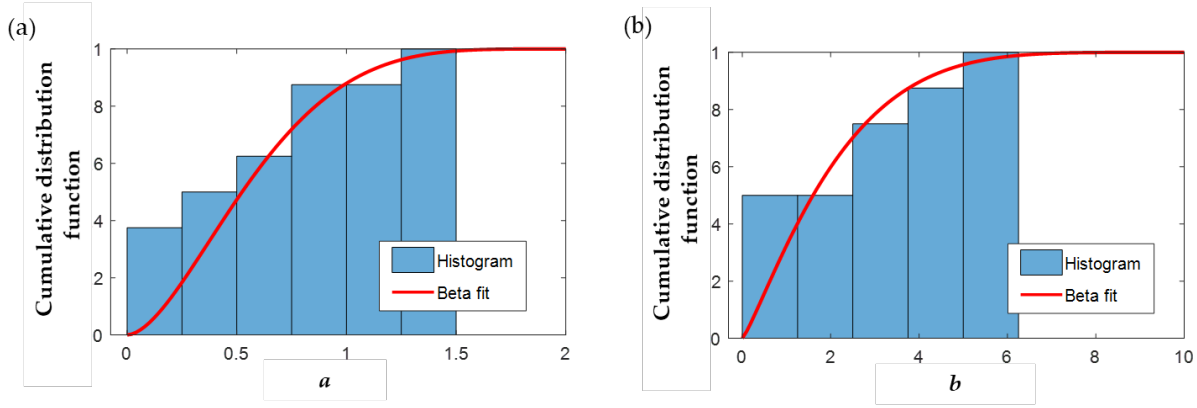

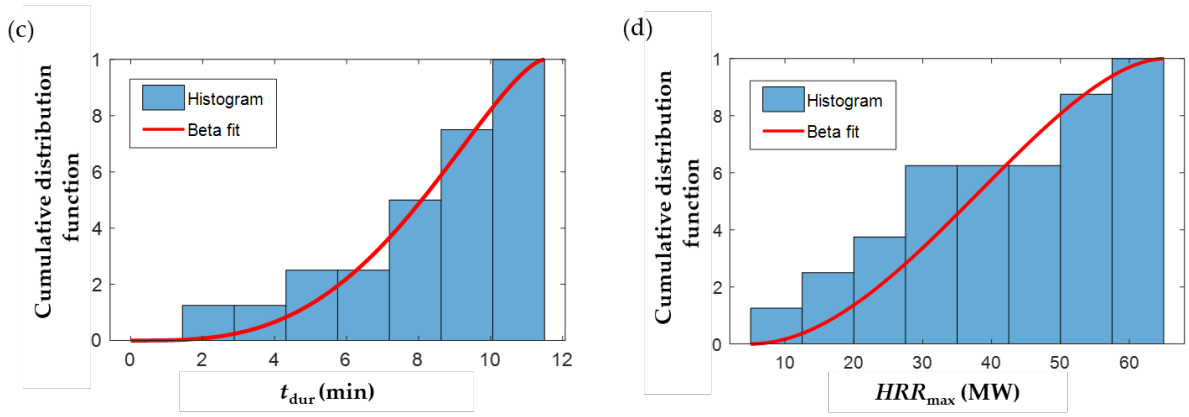

Figure 2.4 Scaled Beta fits for the four parameters of HRR evolution curves

Table 2.2 Parameters of the scaled Beta distribution for characterizing HRR demand

Parameter	Distribution	Considered Range	α	β
a	Scaled Beta	(0,2)	1.80	4.50
HRR_{max} (MW)	Scaled Beta	(5,65)	2.00	1.80
t_{dur} (min)	Scaled Beta	(0,11.5)	3.25	1.55
b	Scaled Beta	(0,10)	1.20	5.00

To investigate the range of potential fire scenarios, ten HRR curves are generated using the scaled Beta distributions of the four parameters as reported in Table 2.2. The Latin hypercube sampling (LHS) method is used to reduce the number of necessary runs to capture the full range of potential outcomes. The sampling results of the four parameters are presented in Table 2.3 and the ten generated corresponding HRR curves are shown in Figure 2.5. These ten curves are consistent with the data from large-scale tests in terms of the peak values and durations. The generated curves also capture both "long, low-intensity" and "short, high-intensity" fires as featured in the experimental data. As discussed later, the ten HRR curves will be used as an input to the FDS analysis to investigate a series of potential fire scenarios.

Table 2.3 The generated realizations of HRR curve parameters using scaled Beta distribution

HRR sample	a	HRR_{max} (MW)	t_{dur} (min)	b	E_{tot} (GJ)
HRR 1	0.173	37	10.0	0.693	82
HRR 2	0.426	58	5.8	1.062	115
HRR 3	1.033	55	8.6	0.570	188
HRR 4	0.589	28	4.9	4.849	13

HRR 5	1.165	46	9.2	1.787	61
HRR 6	0.668	43	6.7	1.246	62
HRR 7	0.445	31	9.4	2.070	31
HRR 8	0.784	11	3.8	0.020	184
HRR 9	0.120	22	7.6	3.364	14
HRR 10	0.305	35	10.9	2.839	36

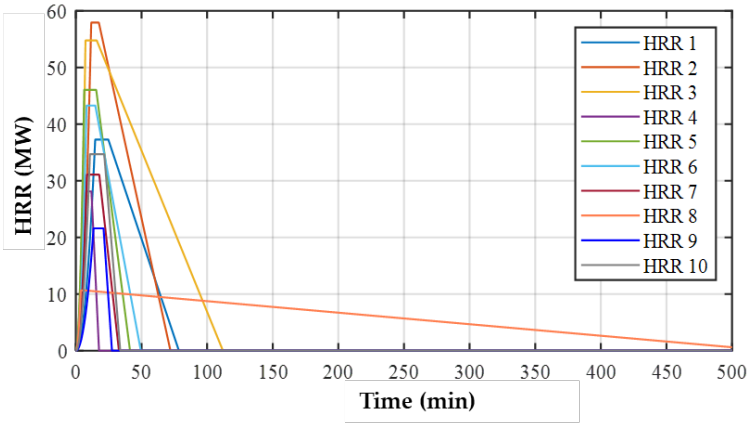

Figure 2.5 The generated HRR curves

2.1.3 Ventilation condition

Ventilation of a tunnel can be achieved by either natural or mechanical (forced) means. Natural systems rely on the piston-effect of moving vehicles, external wind, as well as the pressure differentials between the portals to produce airflow through the tunnel. Natural ventilation exists in all tunnels to a varying extent. While mechanical ventilation systems are driven by fixed fans to produce the airflow [64].

Mechanical ventilation systems are generally classified as longitudinal or transverse based on the direction of airflow in the traffic space. Longitudinal systems ensure a longitudinal flow along the axis of the tunnel with fans at portals or distributed along the tunnel, whereas transverse systems use air ducts to circulate polluted and fresh air perpendicular to the tunnel axis. Practically, longitudinal ventilation systems are easier to adopt and cheaper compared to transverse systems. PIARC [65] provided a summary of typical practices in 17 countries for design-fire assumptions and ventilation. In the majority of the countries, the longitudinal

ventilation systems are designed to control fires with higher HRRs, as this mode of ventilation can deal with larger fires more economically. Considering the above, this research only investigates tunnel fires under longitudinal ventilation.

NFPA 502 [5] requires emergency ventilation in tunnels with lengths exceeding 1000 m. For life safety concerns in the tunnels operating with passenger trains, the ventilation system should be designed to create an air velocity exceeding the critical velocity (V_c) in the tunnel. The critical velocity is defined as "the minimum steady-state velocity of the ventilation airflow moving towards the fire, within a tunnel or passageway, that is required to prevent back-layering at the fire site (back-layering refers to the flow of smoke in the upper cross-section of the tunnel in the opposite direction of the forced ventilation air)" [5]. This requirement is imposed to allow evacuation of passengers to one end of the tunnel while the fire is burning and spreading in the opposite direction. Therefore, the design of emergency ventilation system for longitudinal airflow should be based on the critical velocity. For this study, it is assumed that a train will stop as soon as a fire emergency is detected. Thus, no airflow is produced by the piston-effect of a moving train, and the fans are activated soon to allow evacuation. The generated longitudinal ventilation velocity should be equal to or greater than the critical velocity.

The influencing factors on the critical ventilation velocity (V_c) have been widely studied and relevant predictive models have been developed [66-71]. The most applicable and commonly used equations for calculating critical velocity are listed in Table 2.4 [5, 51, 67, 71]. The equation for critical velocity from NFPA 502 is taken from the 2017 edition of the code. The table also summarizes the parameters that each equation considers. Several observations can be made by comparing the four equations: (1) they are all based on the theory of Froude number and are semi-empirical equations, (2) they all show a trend that the critical velocity stops increasing after HRR reaches a certain threshold, and (3) the HRR and tunnel height are considered as the major parameters influencing the value of critical velocity in all the equations, but other influencing factors vary from one model to another. Only Li's model considers both the tunnel slope and blockage as additional influencing factors, where blockage captures the influence of disturbed air flow due to presence of the railcars.

Table 2.4 Summary of available formulations to calculate the critical velocity for a tunnel fire

Authors	Equations		Parameters
Oka and Atkinson [51]	$V^* = \begin{cases} k_v \left(\frac{Q^*}{0.12}\right)^{1/3}, & Q^* \le 0.12 \\ k_v, & Q^* > 0.12 \end{cases}$ $Q^* = \frac{Q}{\rho_a C_p T_a g^{1/2} H^{5/2}}$ $V^* = \frac{V_c}{(gH)^{1/2}}$	(2.1)	HRR, tunnel height, blockage
Wu and Bakar [71]	$V^* = \begin{cases} 0.4 \left(\frac{Q^*}{0.20}\right)^{1/3}, & Q^* \le 0.20 \\ 0.4, & Q^* > 0.20 \end{cases}$ $Q^* = \frac{Q}{\rho_a C_p T_a g^{1/2} \overline{H}^{5/2}}$ $V^* = \frac{V_c}{(g\overline{H})^{1/2}}$	(2.2)	HRR, tunnel hydraulic diameter
Li et al. [67]	$V^* = \begin{cases} 0.81 Q^{*1/3}, & Q^* \le 0.15 \\ 0.43, & Q^* > 0.15 \end{cases}$	(2.3)	HRR, tunnel height, blockage, slope
	$V^* = \begin{cases} 0.63 Q^{*1/3}, & Q^* \le 0.15 \\ 0.33, & Q^* > 0.15 \end{cases}$ $(20\%\ blockage)$	(2.4)	
	$Q^* = \frac{Q}{\rho_a C_p T_a g^{1/2} H^{5/2}}$ $V^* = \frac{V_c}{(gH)^{1/2}}$ $V_{cs} = V_c(1 + 0.014\theta)$		
NFPA 502 [5]	$V_c = K_1 K_g \left(\frac{gHQ}{\rho_a C_p A T_f}\right)^{1/3}$ $T_f = \left(\frac{Q}{\rho_a C_p A V_c}\right) + T$	(2.5)	HRR, tunnel height, cross-section area, slope

where:

A = tunnel cross-section area (m²)

C_p = thermal capacity of air (kJ/kg K)

g = gravitational acceleration (m/s²)

H = tunnel height (m)

$\overline{H}$ = mean hydraulic tunnel height defined as the ratio of four times the tunnel cross-section area to the tunnel perimeter (m)

k_v = coefficient in Eq. 2.1, varying with geometry and location of the fire source

K_1 = coefficient in Eq. 2.5, varying with HRR

K_g = grade factor

Q = heat release rate (kW)

Q^* = dimensionless heat release rate

T = temperature of the approach air (K)

T_f = average temperature of the fire site gases (K)

V_c = critical velocity (m/s)

V_{cs} = critical velocity in a sloping tunnel (m/s)

V^* = dimensionless critical velocity

θ = tunnel slope in degrees (deg)

ρ_a = ambient air density (kg/m^3)

Based on the above observations, several case studies were completed as part of this work to investigate the consistency between the results of listed equations and an FDS model. The results show that Li's equation, which is the most recent published study among the listed research papers, and considers the influence of both blockage and slope, matches results of the FDS model well. Hence, Li's equation (with blockage) is selected to calculate the critical velocity for the tunnel geometry of Figure 2.1. However, in practice, fans may be controlled by the tunnel operator, adding uncertainty due to human-element in the process. Given the lack of data to quantify the uncertainty in ventilation velocity during a tunnel fire, and given the variation in detection time, operator reaction, and the time needed to change fan's operation mode, a uniform distribution with a range of $0.8V_c$ to $1.5V_c$ is assumed for the ventilation velocity. The critical velocity (V_c) of 2.65 m/s is calculated using Eq. 2.4, with the HRR curves of Figure 2.5 (limiting to HRR values larger than 20 MW) and the tunnel slope of zero. The random realizations for ventilation velocity are generated using LHS and based on a uniform distribution with the range between 2.1 m/s (0.8 V_c) and 4.0 m/s (1.5 V_c). The three generated values for ventilation velocity are 2.45 m/s, 3.08 m/s, and 3.70 m/s, which will be used in conjunction with the 10 HRR curves to define a range of fire events. The assumption for ventilation conditions discussed above may not be suitable for tunnels without a fan system (e.g., freight tunnels), which is out of the scope of this report.

2.1.4 Ignition location and ignition criteria for fire spread

When a fire starts in a tunnel, the fire spread between railcars will exacerbate the fire size and the potential damage. Lessons can be learned from the Channel Tunnel fires [50,51]. The Channel Tunnel linking the UK and France, has experienced three major fire events in 1996, 2006, and 2008 since its opening in 1994. Uncontrollable spread of fire occurred in both the 1996 and 2008 fires. The 1996 fire ultimately involved the rearmost ten heavy goods vehicle (HGV) carriers and damaged the rear loader wagon and locomotive. The 2008 fire was even more destructive than the 1996 fire, with nearly all cars in that train being destroyed and 650 m of concrete lining was damaged. Fire spread has also been identified as a major reason for the uncontrollable fire size and duration in some extreme roadway tunnel fire events. The distance between carriages are relatively short. Hence, if a railcar catches fire, the adjacent cars, especially the ones positioned on the downstream side of the fire can easily become involved by heat radiation. Furthermore, it is hard to detach the intact railcars in a tunnel space during a fire emergency.

Although fire spread has been a major concern in train fires, the research on tunnel fire spread is quite limited. The only full-scale fire spread test inside a tunnel is the Runehamar tests [72-74], where several targets were placed at different locations downstream of a mimicked HGV fire. The targets were small wood or plastic panels placed at distances from 20 m to 70 m from the center of the simulated HGV setup. The test concluded that the wood crib and plastic materials placed on the floor level would ignite when the ceiling temperatures reach approximate 700 °C and 500 °C, respectively. The study also pointed out that it is much easier for the materials placed closer to the ceiling to ignite due to piloted ignition.

In the case of real passenger carriages, it is difficult to characterize the ignition condition. First, the ignition source varies, which can evolve into different paths of fire spread. Second, passenger trains have multiple types of carriages including seating, sleeping, and dining carriages, made from varying materials. Moreover, the window and door properties and configurations play an important role in the fire spread pattern. Considering all the uncertainties, it is impossible to determine a single value of ignition temperature or fire spread rate between

passenger carriages. Andreini et al. [75] provided ignition temperatures of six materials as the main components of a typical Italian passenger rail carriage, which were obtained from a series of cone calorimeter tests. The results are summarized in Table 2.5.

Table 2.5 Ignition temperatures of Italian passenger train materials [75]

	Seat (cover and foam)	Floor (rubber)	Curtain	Headrest (cover)	Wall	Ceiling
Ignition Temperature (°C)	352	419	436	398	427	462

In this study, a train carriage is considered as a lumped mass and modeled as an object with bulk thermal properties and an ignition temperature. When the surface of an object reaches the ignition temperature, it will ignite and follow one of the HRR evolution curves as defined earlier in Figure 2.5. To account for the uncertainty in the ignition temperature, a potential range of 300 °C to 500 °C is assumed considering that, the reported ceiling temperatures in Runehamar tests provide an upper bound while values in Table 2.5 provide a lower bound for ignition temperature. Further tests and data are needed to arrive at a proper distribution for ignition temperature of a railway car. Hence, three values of 300 °C, 400 °C, and 500 °C are selected as ignition temperatures when constructing fire scenarios in Section 2.2.3.

2.2 Modeling fire scenarios using computational fluid dynamics

2.2.1 Fire Dynamics Simulator

The computational fluid dynamics (CFD) simulations are conducted with the Fire Dynamics Simulator (FDS) to obtain the temporal and spatial distributions of gas temperatures from a series of fire scenarios. FDS is a large-eddy simulation code for low-speed flows, with an emphasis on smoke transport and heat transfer. FDS takes heat release rate, ventilation, and tunnel geometry as inputs and generates temperature evolution curves at measurement points that are specified by the user. A separate code called Smokeview (an OpenGL graphics program) [76] is used to visualize FDS output. The following sections will firstly present two verification

studies for the modeling method, then the details of the parametric studies for capturing railway tunnel fire scenarios are introduced.

2.2.2 Verification

Data from two sets of published experiments are selected to evaluate and verify the CFD modeling approach adapted in this report. The first experiment was a small-scale test conducted by the SP Institute [74] in a 12-meter long model tunnel, and the second experiment was a full-scale test from the Memorial Tunnel Ventilation Test Program (MTVTP) [77-79]. The simulations for both experiments in this verification study are conducted with FDS 6.7.2.

(i) SP small-scale test

The small-scale experiment [74] was carried out in a rectangular model tunnel with dimensions of 12 m (length) x 0.25 m (height) x 0.25 m (width). The tunnel lining was made of 1 mm thick stainless steel. The fire source was a 0.1 m diameter porous bed burner set on the floor level and 6 m away from the downstream exit. Propane was used as the fuel and the gas flow rate was measured by a rotameter with 1% accuracy. Ventilation was created by a 5.25 m long air supply duct and flow rate volume of the air was measured by a vortex flowmeter with 1% accuracy. Gas temperature inside the tunnel was measured with K-type thermocouples. The temperature measurement devices were located at both 0.9 m upstream and 1.8 m downstream. To capture the temperature difference along the tunnel height, each of the selected cross-sections was equipped with 11 measuring devices distributed from the floor level to the ceiling height.

The tunnel was modeled in FDS with the same dimensions. According to the reported data from the experiment, the ambient temperature and pressure were set to 24 °C and 95590 Pa, respectively. Air was blown from one side of the tunnel with a longitudinal velocity of 0.51 m/s during the test. The other side of the tunnel in the model was assigned an open surface. The fuel was modeled as propane with a constant HRR of 9.45 kW. The total time was set to 120 seconds to reach a steady state of fire. The FDS model output from Smokeview is shown in Figure 2.6, and

the comparison of gas temperatures between simulation results and test data is provided in Figure 2.7.

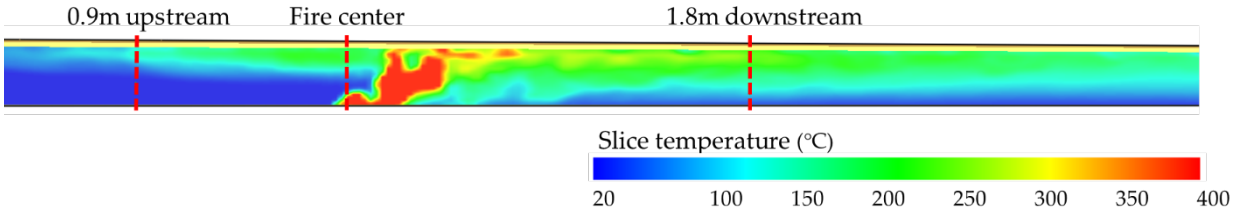

Figure 2.6 FDS simulation of SP model-scale test, slice temperature at 30 s from Smokeview

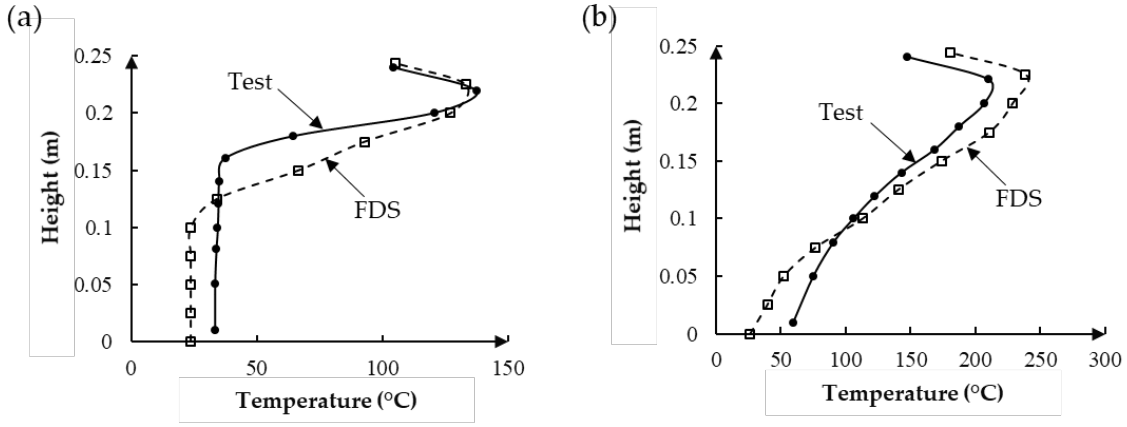

Figure 2.7 Comparison between FDS results and SP test data at (a) 0.9 m upstream from the fire center and (b) 1.8 m downstream from the fire center

Overall, the temperature output from FDS matches well with both upstream and downstream test data, and the temperature distribution pattern along the tunnel height is similar. The simulation slightly underestimates the gas temperature near floor level and slightly overestimates the temperature close to the ceiling. These differences can be explained by the ventilation conditions during the test. In the FDS simulation, it is assumed that the ventilation velocity is identical across the tunnel entrance, while in the real test, the ventilation velocity at the entrance might not be uniformly-distributed. Other details such as the assumed radiative fraction can also contribute to the observed discrepancies.

(ii) Memorial Tunnel Fire Ventilation Test No. 621A

The Memorial Tunnel Fire Ventilation Test (MTFVT) Program [77-79] was developed and conducted by the Federal Highway Administration (FHWA) and the Massachusetts Highway Department (MHD) in a decommissioned highway tunnel in West Virginia in 1990s. The two-lane tunnel was 853 m long and had a 3.2% upgrade from the south to the north portal. The cross-section of the tunnel is 8.8 m wide, and 7.9 m high with a semi-circular ceiling (shown in Figure 2.8). The main objective of the MTFVT was to understand temperature and smoke movement and to determine the effectiveness of various ventilation configurations, ventilation rates, and the operating modes in the management of the spread of smoke and heat for tunnel fires of varying intensities under full-scale fire test conditions. A series of fire tests with various fire sizes (the peak HRR ranges from 10MW-100MW) and ventilation schemes were completed to accomplish the objective of the test program.

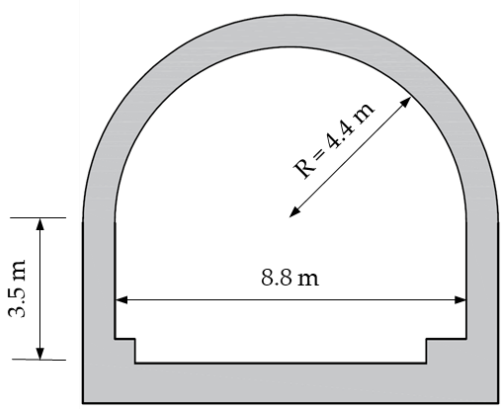

Figure 2.8 The Memorial Tunnel cross-section (adapted from [79])

Detailed experimental data of test No. 621A is available in published literature [80]. In this test, the fire site was located at about 615 m from the north portal, 238 m from the south portal, and 0.75 m above the floor. No. 2 fuel oil (as explained in [81]) was used to generate a fire of 100MW. Eight groups of three jet fans were used to create forced, transient, and longitudinal ventilation. The tunnel plan showing the arrangement of the jet fans and the fire site is shown in Figure 2.9. During the test, the jet fans generated airflow from north to south in the downgrade direction. The ventilation flow maintained its direction during the test, but the speed of airflow increased or decreased depending on the number of operating fans. As Figure 2.9 shows, a series

of instruments were installed along the tunnel to measure air temperature, air velocity, and gas concentrations.

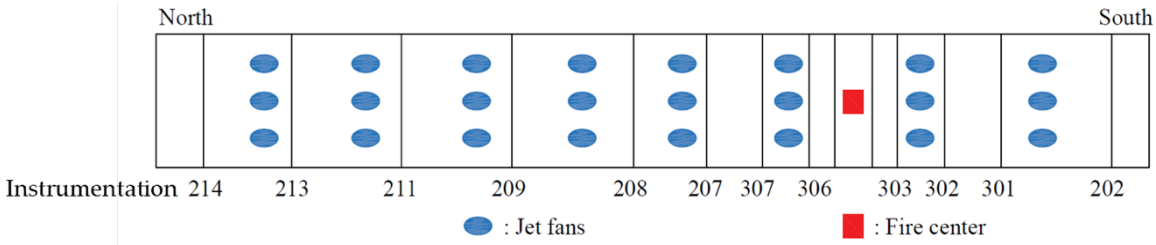

Figure 2.9 Layout of the ventilation systems in the Memorial Tunnel Test No. 621A (adapted from [80])

Based on the results of a previous study [82], the generated FDS model of the test 621A only includes 345 m of the tunnel length, considering the computational cost of the simulations and the jet fan arrangements in the ceiling. The north portal of the modeled tunnel is located at 107 m upstream from the fire site. Based on the experimental data, temperatures remained close to ambient beyond 107 m upstream of the fire. The ventilation velocity data measured from instrumentation 207 (at 107 m north of the fire and 6.3 m above the ground) is used as the inflow air velocity at the north entrance during the simulation. The south portal of the tunnel is set to be open to the ambient air. Figure 2.10 shows the FDS model of the test. The curved ceiling is constructed with multiple rectangular elements and the tunnel has a downward slope of 3.2% from north to south. Kim et al. [82] investigated the MTFVT No.621A using FDS, and performed the grid sensitivity analysis for the model, concluding that a grid size equal to 8% of the characteristic fire diameter (0.5m) is appropriate. A grid sensitivity analysis was completed by the authors, which confirmed the conclusion by [82]. Hence a grid size of 0.5m is selected in this study.

As for the fuel modeling, the Agency for Toxic Substances and Disease Registry (ATSDR) [81] provided the volume percentages of hydrocarbons of the No. 2 fuel oil that was used in this test. Based on the data, the No. 2 fuel oil consists of 75.3% saturated hydrocarbons and 24.7% aromatic hydrocarbons by volume. The formulas and combustion properties of different types of saturated and aromatic hydrocarbons can be found in the SFPE Handbook [83]. In the FDS model,

the simple chemistry model is used to capture the reaction. The fuel is specified as C10H18.7, which comes from the average volume proportions and the atomic numbers of each type of hydrocarbons. The surface area of fuel pool is taken as approximately 45 m^2. The other parameters, including the radiative fraction, heat of vaporization and the LES (Large Eddy Simulation) turbulence model related parameters are kept as default, as Kim et al. [82] suggested. Baroclinic torque is neglected in the FDS model.

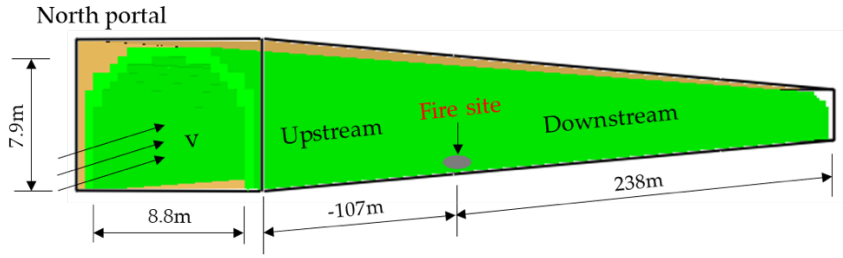

Figure 2.10 FDS model of the Memorial Tunnel test 621A

The duration of the MTFVT No.621A was 30 minutes. The measured inflow air velocity and HRR of the fire during the test are shown in Figure 2.11 (labeled as HRR-0 and v-0). An FDS simulation with the original inputs were conducted as the control case (Case 0). The results of the control model are first compared with the experimental data regarding ventilation velocities and gas temperatures at both downstream and upstream of the fire (Upstream: "-", Downstream: "+"), as shown in Figure 2.12 and Figure 2.13, where the black dashed line shows the test data and the red line shows the FDS results for Case 0. The air velocities and temperatures are measured at 6.3 m above the floor level, while the air velocity was not uniformly distributed across the tunnel section. The following observations are made: (1) the output ventilation velocity at -107m doesn't converge to the input value from 500s to 1500s, (2) the ventilation velocity at +66m matches the test data, and (3) the FDS model over-estimated the upstream gas temperature near the ceiling up to 250°C, and under-estimated the downstream temperature up to 300°C, (4) the temperature profile from the FDS model follows a similar shape to the input HRR curve, where two distinct peaks are observed at the beginning and the end of the test, while this trend is not observed in the test measurements.

The previously published FDS simulation of the same test reported similar results. Kim et al. [82] recorded discrepancies in the upstream, center, and downstream ceiling temperatures in the order of 250 ˚C (over-prediction), 440 ˚C (under-prediction), and 220 ˚C (under-prediction), respectively and observed similar trends using different grid sizes in the FDS model. The study also reported measurement errors for the HRR and air velocity as 8-15% and 3-4%, respectively.

To develop a better understanding of the model, four additional simulations (Cases 1 to 4) were completed using a combination of updated HRRs (HRR-1, HRR-2, HRR-3) and velocities (v-1, v-2, v-3). The updated HRR and velocity profiles stay within ± 15% (black dash line) of its original values to account for the possible errors as discussed above. The updated HRR cases are designed to slightly reduce the two distinct peaks towards the beginning and end of the test from the control case, to smoothen the temperature profiles according to the observed trend. The HRR profiles from 500s to 1500s are also adjusted to properly capture back-layering and improve the level of convergence. The updated input velocities at -107m are generally higher than the original input to reduce the upstream temperature and the duration of back-layering. Table 2.6 shows the input HRR and velocity corresponding to each case. The results of the updated FDS models are also compared with experimental data for ventilation velocities and gas temperatures as shown in Figure 2.12 and Figure 2.13.

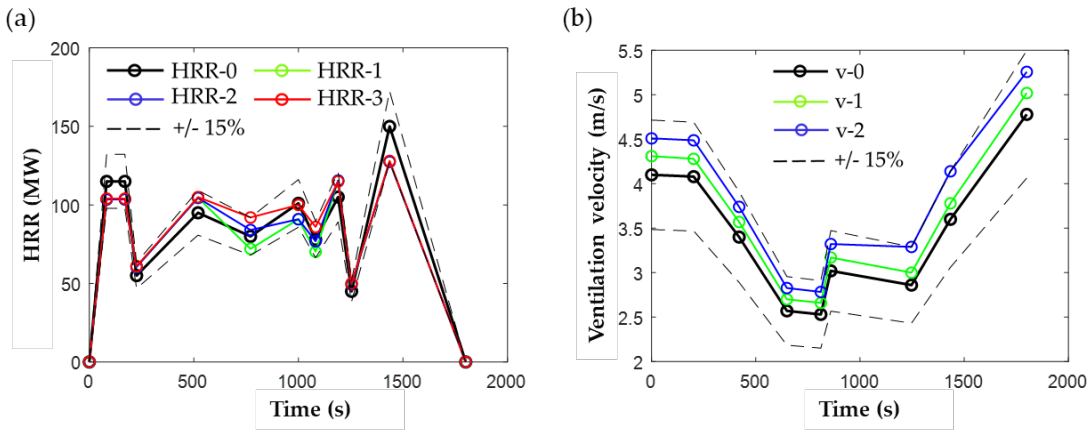

Figure 2.11 Input (a) HRR and (b) ventilation velocity for FDS simulations

Table 2.6 Considered FDS inputs to simulate the Test 621A

Case Number	HRR	Ventilation velocity
0	HRR-0	v-0
1	HRR-1	v-2
2	HRR-2	v-2
3	HRR-3	v-1
4	HRR-3	v-2

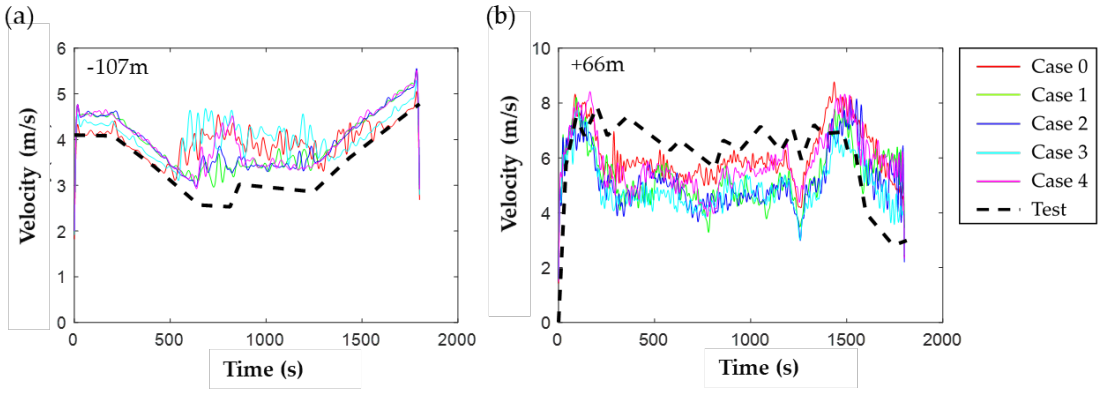

Figure 2.12 Comparison of results for air velocities at (a) 107m upstream and (b) 66m downstream from the Test 621A

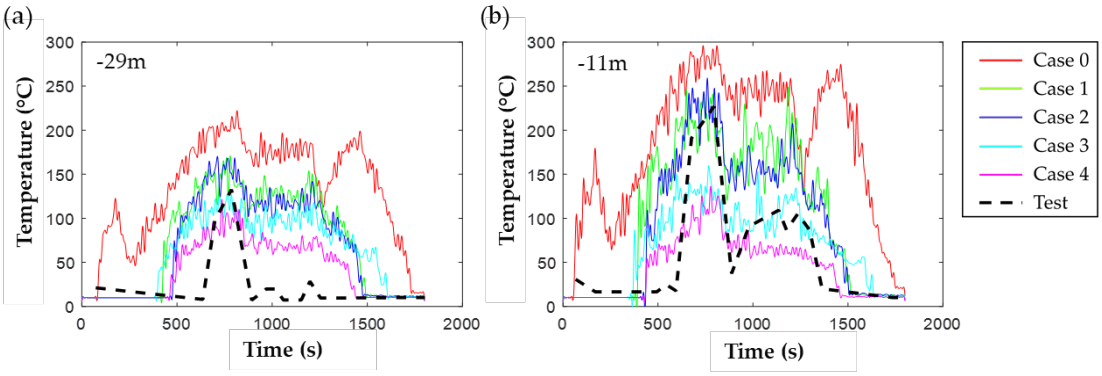

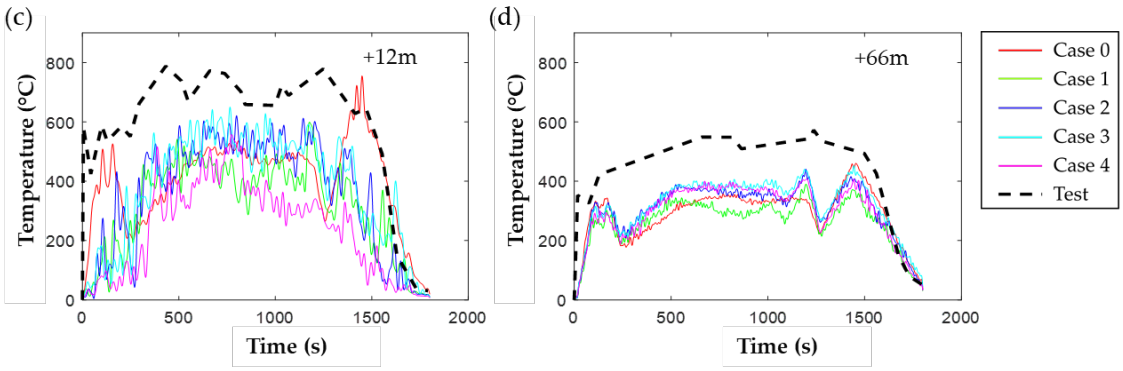

Figure 2.13 Comparison of results for gas temperatures at (a) 39m upstream, (b) 11m upstream, (c) 12m downstream, and (d) 66m downstream from the Test 621A

Overall, the air velocity outputs from the FDS model reasonably match the test data. In the additional four simulations, Cases 1, 2 and 4 have better converging performance (Figure 2.12a), compared to the input velocity profiles in Figure 2.11b. The updated simulations also show better agreement between test data and simulation results for downstream air velocities during the first 100s and the last 500s (Figure 2.12b), owing to the adjustments of input velocities.

The air temperatures are recorded at 29 m and 11 m upstream, as well as 12 m and 66 m downstream. As shown in Figure 2.13a and b, compared with Case 0, Cases 1-4 show better predictions of upstream temperatures and also capture the back-layering period with better accuracy. The results in Figure 2.13c and d show that the simulations underestimate the temperature downstream of the fire. At 66 m downstream of the fire location, the simulation results do not vary much with the change in HRR and the input velocity at the entrance. The upstream air temperatures are more sensitive to the input velocity and HRR conditions. The discrepancies can be related to the transient air velocity during the test, which was generated by operating jet fans distributed along the tunnel length, located 107 m upstream all the way to the south portal (Figure 2.9). However, the FDS model idealizes air velocity as an input at the tunnel entrance. In addition, the staged operation of fans, which occurred during the test, are not captured in the model. Based on the test report, a number of instruments and equipment were placed inside the tunnel during the fire tests, which could have formed some blockage but is not reflected in the model. Given: (1) the listed differences between the test arrangement and the

model, (2) the comparison of our results with those of a previously conducted FDS study of the same test with relevant simplifying assumptions [82], and (3) the validation study in part (i) of this section with the SP test setup, it is concluded that the modeling approach is verified and can be used to investigate a scenario-based study of fire events in a railway tunnel in the next section.

2.2.3 Parametric study

This section studies the influence of different parameters on the temperature-time evolution of fire in the prototype railway tunnel (Figure 2.1). Based on the discussion in Section 2.1, a total of 540 railway tunnel fire scenarios are modeled in FDS. The scenarios are defined considering three different tunnel slopes, two potential initial ignition points in the train, ten HRR curves (shown in Figure 2.5), three ventilation velocities in the tunnel, and finally three ignition temperature criteria for fire spread. While a scenario-based approach is adapted in this study, future research may investigate a full probabilistic study, where all parameters are randomly generated. However, covering the full spectrum of potential outcomes through a probabilistic study will require further data from large-scale experiments or questionnaires completed by experts on the subject, and increased computational calculation capacity.

The considered parameters are summarized in Table 2.7. The tunnel geometry is assumed to be that of the Howard Street Tunnel (Figure 2.1) with cross section of 0.3 m-thick concrete. The curved ceiling is constructed using rectangular obstructions in FDS (Figure 2.14). Thermal properties of the tunnel lining were defined in the FDS model to capture the influence of thermal conduction of tunnel lining on the surface gas temperature. The thermal conductivity of concrete is taken as 1 W/m-K, specific heat as 1000 J/Kg-K, and density as 2400 kg/m^3. The FDS model follows a similar modeling approach that was verified in Section 2.2.2. The model includes 260 m of the tunnel length with five passenger rail cars, as shown in Figure 2.15. The distance from the left portal of the tunnel to the left edge of the first train carriage is 50 m. The ambient temperature and background pressure are set as 20 °C and 101325 Pa in the simulations. The air flow is assumed to blow at a constant velocity from the left entrance of the tunnel, while the right portal is set to be open to ambient air.

Table 2.7 Summary of considered variables

Parameters	No. of realizations	Input value
HRR	Ten	HRR curves showed in Figure 2.5
Ventilation velocity	Three	2.45 m/s, 3.08 m/s, 3.70 m/s
Tunnel slope	Three	upward 2.2%, zero, downward 2.2%
Ignition point	Two	First or third car from the north entrance
Ignition temperature	Three	300 °C, 400 °C, 500 °C

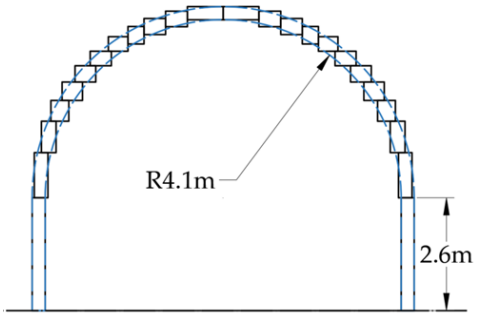

Figure 2.14 Modeled tunnel lining in FDS

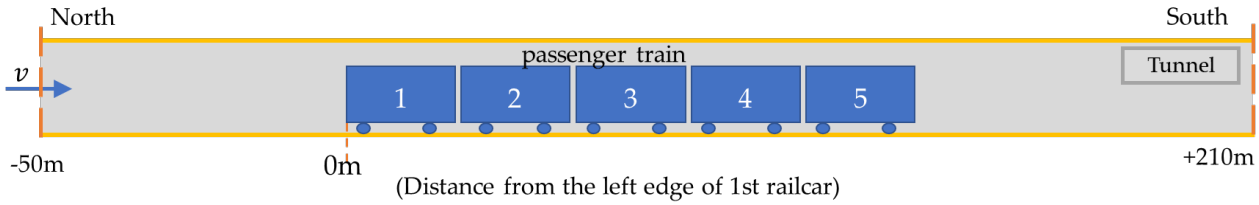

Figure 2.15 Schematic of the FDS model

The size of a railcar can also affect the gas temperature during a tunnel fire, as it influences the distance between the fire source to the ceiling and results in different blockage ratios. Considering that passenger railcar dimensions are relatively standard, even when compared worldwide, the dimension of an Amtrak "Superliner" railcar [84] was adopted in this study for the train model, which is 25.9 m long, 4.9 m tall, and 3.1 m wide. Five identical railcars are aligned longitudinally inside the tunnel to study the fire spread pattern (Figure 2.15). The distance between two adjacent railcars is 1 m. The surface material of the train cars is assumed to be stainless steel, with thermal conductivity of 15 W/m-K, specific heat of 500 J/Kg-K, and density of 7800 kg/m^3. The applied HRR values are normalized by the surface areas of each railcar (expect for the bottom surface), and the evolution of HRR over time is applied using piecewise linear

functions. The fire spread criterion, defined as the ignition temperature, is also assigned to the train surfaces.

For each simulation, the fire temperature-time histories were recorded at: (1) different cross-sections (10 m intervals) to reflect temperature distribution along tunnel length, and (2) three different heights (A-6.4 m, B-3.9 m and C-1.3 m) at each cross-section to account for non-uniform fire damage within a section. The layout of the measurement points around the tunnel lining is shown in Figure 2.16.

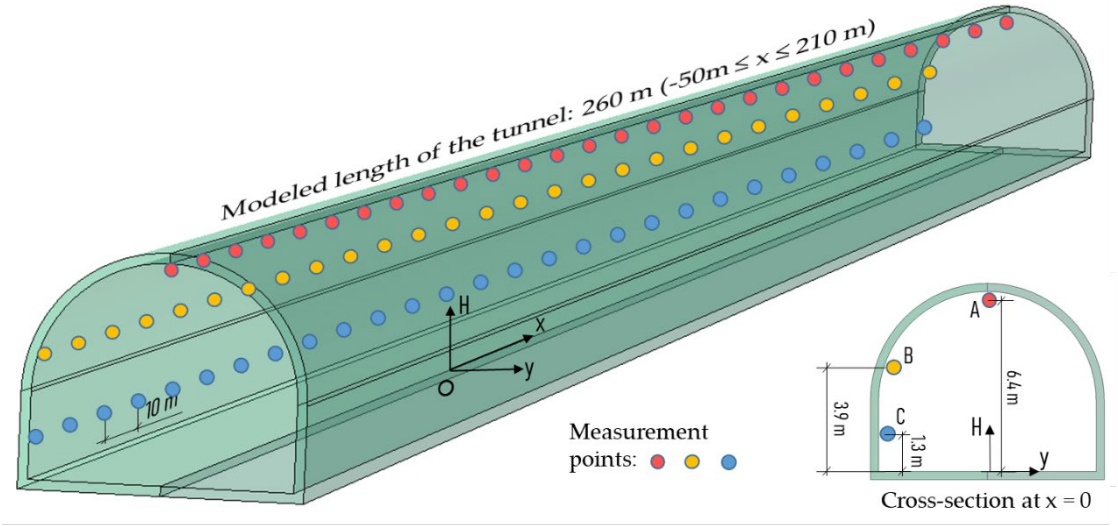

Figure 2.16 Locations of gas temperature measurement points

The results from 540 FDS simulations are organized and presented based on the following two categories:

(1) Temperature-time curves at the critical sections of the prototype tunnel. This part focuses on capturing the control fire demand for design recommendations. Details are introduced in Section 2.3.

(2) Spatial and temporal distributions along the length and across sections of the prototype tunnel. This part focuses on the unique characteristics of tunnel fire scenarios and provide a basis to quantify fire damage to the whole tunnel structure. Details are introduced in Section 2.4.

2.3 Temperature-time curve at critical section

Figure 2.17 shows 50 sample time-temperature curves (out of 540 scenarios) at critical sections of the tunnel. The critical section is defined as the location undergoes the highest peak temperature during a fire. The critical section of the modeled tunnel is typically located at 6.4 m above the ground (captured by point A in Figure 2.16), or 1.4 m above the top surface of the train model. Note that the cross section with the highest peak temperature changes along the length of the tunnel based on the fire scenario, location of ignition, etc. The 50 samples are randomly selected from the 540 scenarios to avoid a dense cluster in the figure and to illustrate the general observed pattern in the simulated temperature-time curves.

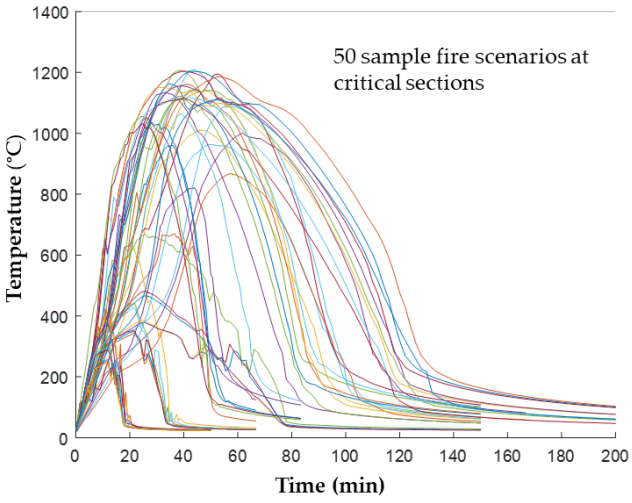

Figure 2.17 Sample results of temperature-time curves from the 540 considered scenarios

2.3.1 Tri-linear model

The objective is to study any trend in the obtained critical temperature-time curves and make recommendations for design considerations. A temperature-time curve can be characterized by its peak temperature, the total duration of fire, and the growth and decay rates of the temperature. Therefore, a tri-linear model is adapted to systematically quantify statistics of the aforementioned parameters in the temperature-time curves. The assumed idealization in this section is similar to the RABT-ZTV tri-linear standard curve [4] developed in Germany. The tri-

linear function captures both heating and cooling phases in a simple form that is convenient to adopt. Each fire curve from the 540 scenarios is idealized as a tri-linear model with the four parameters: α_g, α_d, T_{max} and t_D, as shown in Figure 2.18, where T_{max} is the peak temperature, t_D is the duration of maximum temperature, α_g is the growth rate of temperature, and α_d is the cooling rate. The next paragraph describes the curve-fitting method.

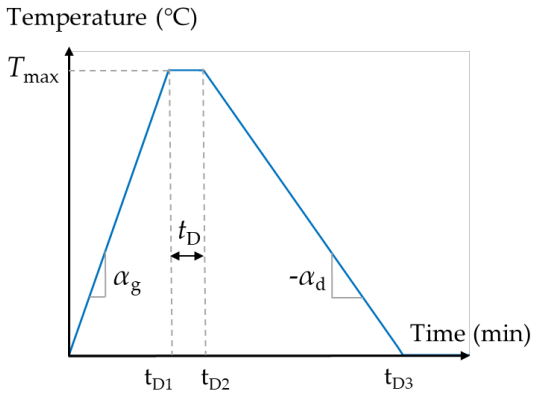

Figure 2.18 Tri-linear time-dependent temperature curve

Each curve in Figure 2.17 has a distinct peak, the value of which is set to be T_{max}. The growth phase of the fire is defined by the line connecting 20 °C (which is the assumed ambient temperature) at time zero to the point of $0.9T_{max}$ prior to reaching the peak temperature, as shown in Figure 2.19a. The decay phase is defined by the line connecting the two points of $0.9T_{max}$ and $0.25T_{max}$ after the peak temperature is reached. Figure 2.19b shows a sample idealized curve using the defined reference points. Figure 2.20 shows the tri-linear idealizations of the 50 temperature-time samples from Figure 2.17. Comparison between Figure 2.17 and Figure 2.20 shows that the tri-linear fit retains the peak temperature and fire duration from the original data set reasonably well. At this point, 540 fire temperature-time curves at critical sections are characterized using the four parameters of α_g, α_d, T_{max} and t_D, distributions of which can be obtained to make design recommendations.

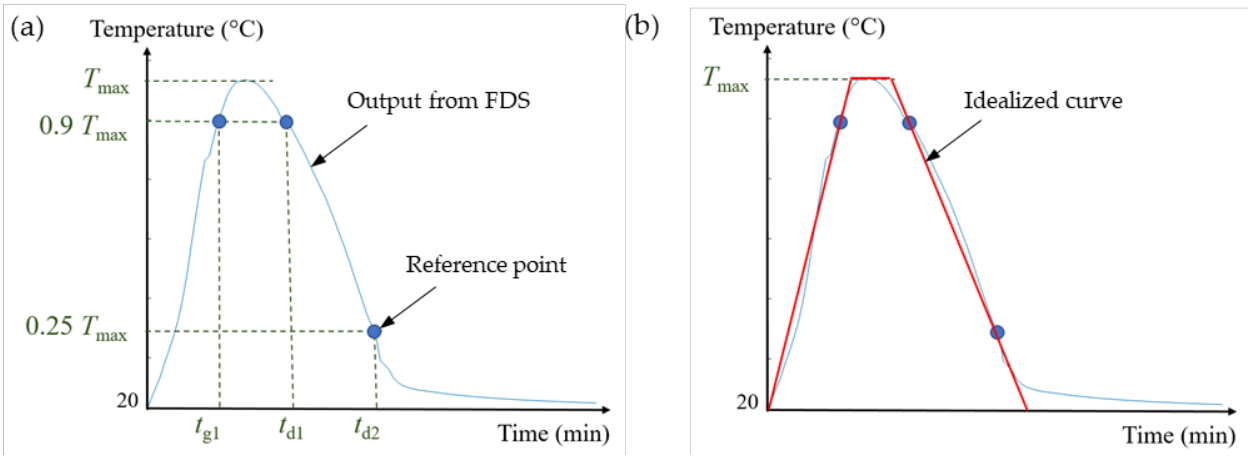

Figure 2.19 Tri-linear curve fitting

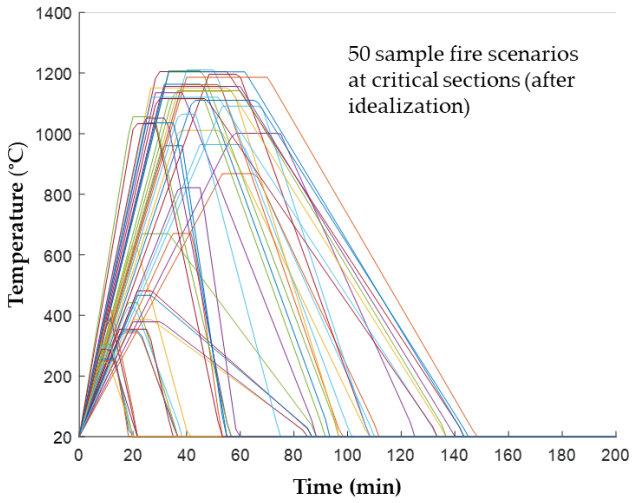

Figure 2.20 Tri-linear idealizations of sample fire curves from Figure 2.17

2.3.2 Distributions of T_{max}, α_g, α_d, and t_D

Figure 2.21 provides the distribution of peak ceiling temperatures (T_{max}) from the 540 scenarios. It is observed that T_{max} follows a bimodal distribution, with a minimum temperature of 100 °C, a maximum of 1250 °C, and two peaks at around 300 °C and 1000 °C, respectively. To investigate the reason behind the obtained bi-model distribution, the data for T_{max} is divided into three categories as a function of HRR, shown in Figure 2.22. The categorized data shows that if $HRR_{max} \leq 30$MW, the peak fire temperature stays relatively low with a mean temperature of 245°C;

this category is labeled as low-intensity fires. On the other hand, if HRR_{max} > 40MW, the fire peak temperature reaches high temperatures with a mean of 1007 ℃; this category is labeled as high-intensity fires. Fire scenarios having HRR values between 30MW and 40MW are controlled by the other parameters such as ventilation conditions and tunnel slopes. No clear trend can be observed in this range of data and thus, the set is labeled as intermediate-intensity fires. A series of distributions (including Normal, Lognormal, Gamma, Logistic, and Beta distributions) were investigated with an objective of finding a distribution type that provides a reasonable fit for all the parameters to streamline the results. It turns out that the Weibull distribution provided an acceptable fit to the four parameters (α_g, α_d, T_{max}, and t_D) and for both high- and low- intensity fire scenarios defined based on the HRR thresholds. Figure 2.22 also shows a Weibull distribution fit to the T_{max} data for both low and high intensity fires. Table 2.8 and Table 2.9 summarize the statistics of T_{max} for low and high intensity fires, and Table 2.10 lists the parameters of the fitted Weibull distributions.

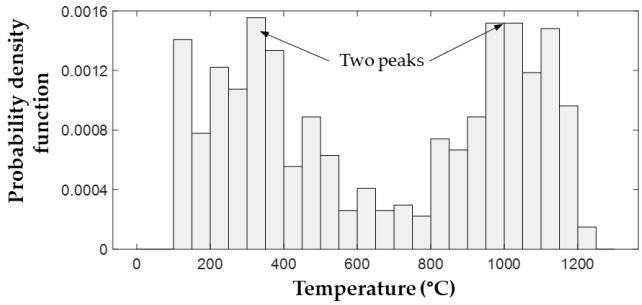

Figure 2.21 Probability density function of T_{max} from 540 fire scenarios

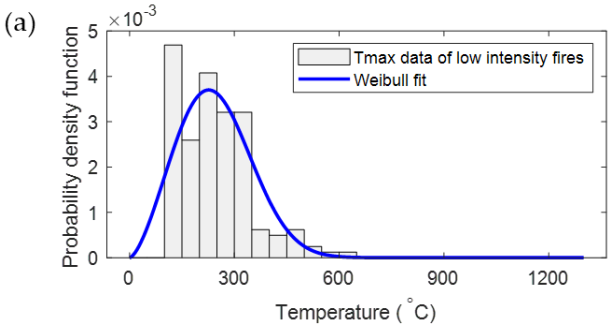

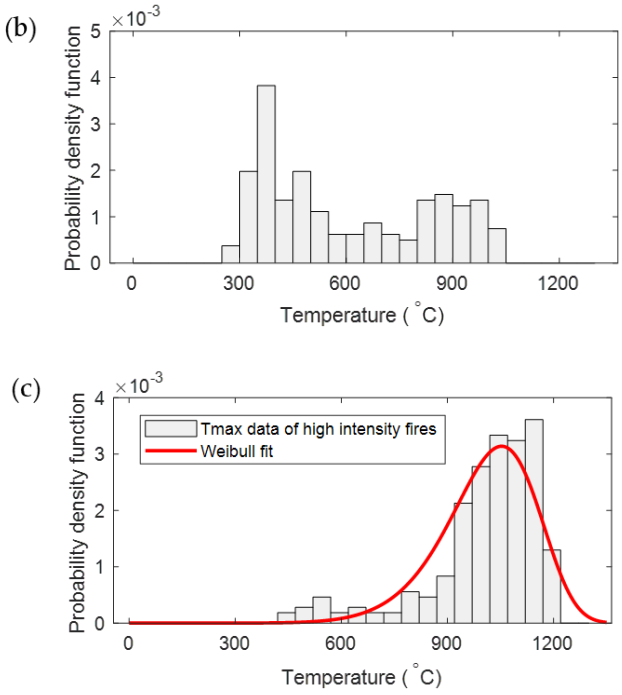

Figure 2.22 Sub-division of fire scenarios based on HRR: (a) low-intensity fires ($HRR_{max} \leq 30$MW), (b) intermediate-intensity fires (30MW < $HRR_{max} \leq 40$MW) and (c) high-intensity fires ($HRR_{max} > 40$MW)

Figure 2.23 shows the distributions of α_g, α_d, and t_D for low and high intensity fires and the corresponding Weibull distribution fits. The probability density function (PDF) plots of α_g and α_d show that the growth and decay rates of high intensity fires are larger than those of low intensity fires. As for the duration of the peak temperature plateau, low intensity fires cover a wider range with a larger mean value. This implies that the results included long low-temperature fire scenarios as well as short hot fires, similar to what could happen in building fires. Table 2.8 and Table 2.9 summarizes statistics of distributions for α_g, α_d, and t_D.

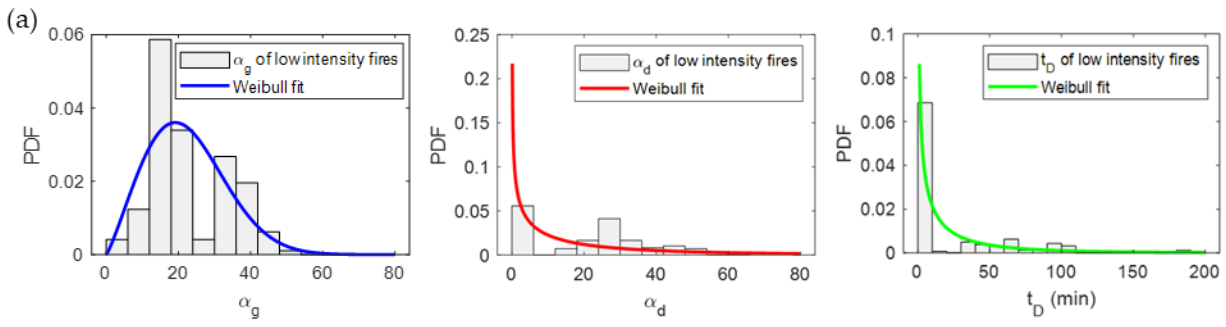

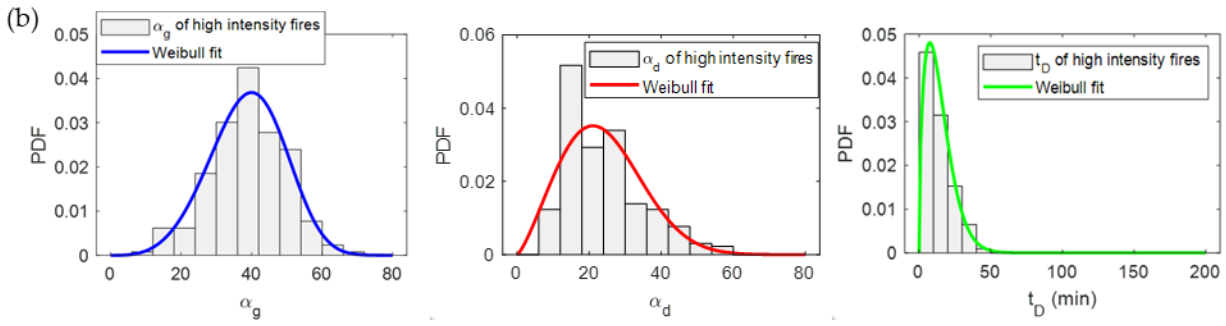

Figure 2.23 Distributions of α_g, α_d, and t_D for (a) low and (b) high intensity fires

Table 2.8 Statistics of temperature-time curve parameters for low intensity fires

Parameter	Min.	Max.	Mean	Std.
α_g	0.9	48.2	22.5	10.7
α_d	0.2	99.7	21.7	19.0
T_{max} (°C)	120	633	245	102
t_D (min)	~0	223.4	27.4	43.6

Table 2.9 Statistics of temperature-time curve parameters for high intensity fires

Parameter	Min.	Max.	Mean	Std.
α_g	10.7	70.4	38.9	10.5
α_d	6.8	59.9	23.8	11.1
T_{max} (°C)	453	1210	1007	163
t_D (min)	~0	44.8	14.1	9.2

2.3.3 Design recommendations

The PDFs of the four parameters and their corresponding Weibull distribution fits can be used to understand and characterize demand fires for passenger railway tunnels. Table 2.10 shows the Weibull parameters of α_g, α_d, T_{max}, and t_D and Table 2.11 provides the quantiles of T_{max} for low and high intensity fires based on the Weibull distributions (values are within ±10% of the generated data). During the design or assessment process, the expected threshold on the HRR of the passenger rail cars going through the tunnel is known, and the performance requirements are agreed upon discussions with stakeholders. The designer can select the appropriate quantile for the maximum fire temperature given the expected performance level, where performance could be defined as the amount of damage in the concrete liner that requires repair or structural

performance of the tunnel. The results of this study provide an insight on the distribution of expected fire temperature-time scenarios, and demonstrates a clear trend among the proposed low- intermediate- and high-intensity fires. For design or assessment purposes, the intermediate-intensity fires with HRR values between 30 and 40 MW can be conservatively assumed as high intensity fires. The results presented in this chapter are valid for railway tunnels with similar geometries as Figure 2.1, and can be used within risk assessment frameworks.

Table 2.10 Weibull parameters of α_g, α_d, T_{max}, and t_D

Weibull parameters	α_g		α_d		T_{max} (°C)		t_D (min)	
	Low	High	Low	High	Low	High	Low	High
A_w	25.3	42.8	17.5	26.9	276	1067	18.5	15.5
B_w	2.2	4.1	0.7	2.3	2.5	9.0	0.6	1.5

Table 2.11 Quantiles of T_{max} for low and high intensity fires

Quantile	T_{max} (°C) for low intensity fires	T_{max} (°C) for high intensity fires
80th	333	1125
85th	356	1145
90th	384	1170
95th	426	1204

2.4 Spatial and temporal temperature distributions

This section will firstly describe a sample "traveling fire" scenario generated in the tunnel as an example of the 540 simulations. Then all the 540 fire scenarios will be statistically presented together to show the overall pattern in obtained temperatures from the passenger train fires. This part of results provides probabilistic-based time-dependent temperature boundaries for the tunnel lining, and serves as the input for analyzing heat propagation within the tunnel segments at different locations, and the consequent fire damage assessment.

2.4.1 Characteristics of tunnel fire scenarios

Figure 2.24 shows temperature recordings from a sample fire scenario, reflecting the spatial and temporal patterns of temperature within the tunnel. The input parameters for the sample case are: HRR_{max} of 37MW, ventilation velocity of 2.45 m/s, tunnel slope of 0.0, ignition temperature of 500 °C, and fire initiating at the first railcar from the North portal.

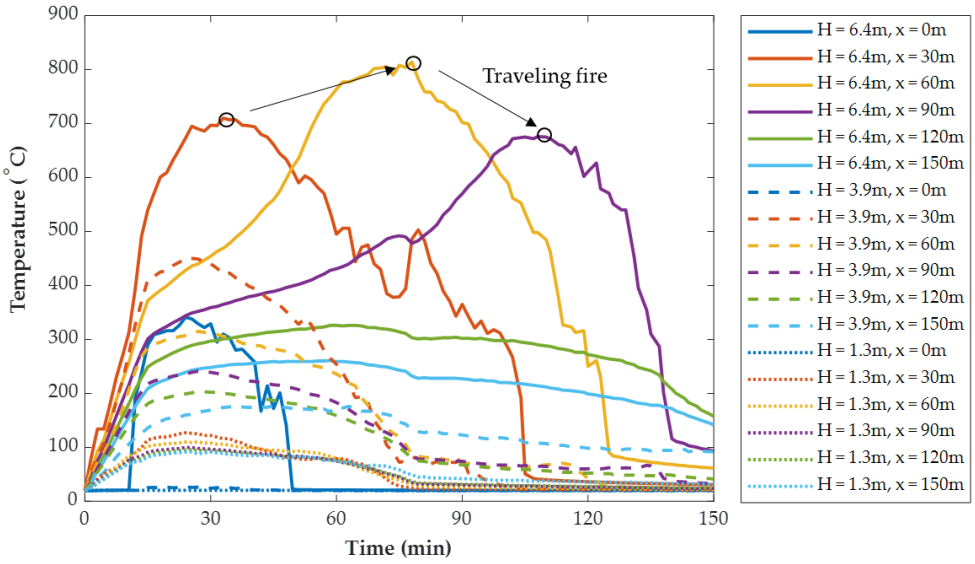

Figure 2.24 Fire temperatures measured at different locations of the prototype tunnel from a sample scenario

The following observations can be made from the data presented in Figure 2.24:

(1) Comparing the measured temperatures at different heights, the ceiling section experiences the highest demand as expected, and temperatures close to the ground remain moderate (below 100 °C) during the fire.

(2) Following the temperature profiles close to the ceiling (i.e., 6.4 m height) confirms the "traveling fire" pattern because of the fire spread between railcars. For example, the cross-section at 30 m downstream of the ignition point reaches its peak temperature at approximately 30 minutes, while the ceiling temperature at 90 m downstream of the ignition point reaches the peak after 90 minutes.

The above two observations are not unique to the sample scenario shown here. They can be tracked in almost all the 540 simulations that considered variations in HRR, ventilation

velocity, slope, ignition point, and temperature as listed in Table 2.7. The result in Figure 2.24 also demonstrate the large variance in the fire demand at different locations along the tunnel and at a given cross section during a single fire event.

2.4.2 Statistics on T_{cri} and t_{cri}

This section provides the statistics of: (1) T_{cri}, defined as the maximum temperature at different tunnel locations along the tunnel length and height, and (2) t_{cri}, defined as the time to reach T_{cri} at the ceiling (H = 6.4 m) to identify the overall trend from all the scenarios. Although the two observations mentioned in Section 2.4.1 are applicable to most of the simulated tunnel fire scenarios, the absolute values of T_{cri} and t_{cri} varies from case to case, because of the different input parameters. The results from 540 simulations are also grouped into three categories based on their HRR_{max} value to stay consistent with the defined categories in Section 2.3: low-intensity fires ($HRR_{max} \leq 30$ MW, 216 out of 540 scenarios), intermediate-intensity fires (30 MW $\leq HRR_{max} \leq$ 40 MW, 162 out of 540 scenarios) and high-intensity fires ($HRR_{max} \geq 40$ MW, 162 out of 540 scenarios). Figure 2.25 and Figure 2.26 show the statistics of T_{cri} and t_{cri} using boxplots. The horizontal red line in each boxplot indicates the median of data. The bottom and top edges of the box indicate the 25th and 75th percentiles, respectively. The maximum whisker length is set to be 1.5. The whiskers extend to the most extreme data points that are not considered outliers, while the outliers are plotted individually using the red '+' symbols. The results are compiled at every 30 m of the tunnel to demonstrate the trend along the tunnel length. In addition, the maximum, minimum, mean, and standard deviation values of T_{cri} and t_{cri} at different tunnel locations are tabulated in Table 2.12, Table 2.13, Table 2.14 and Table 2.15.

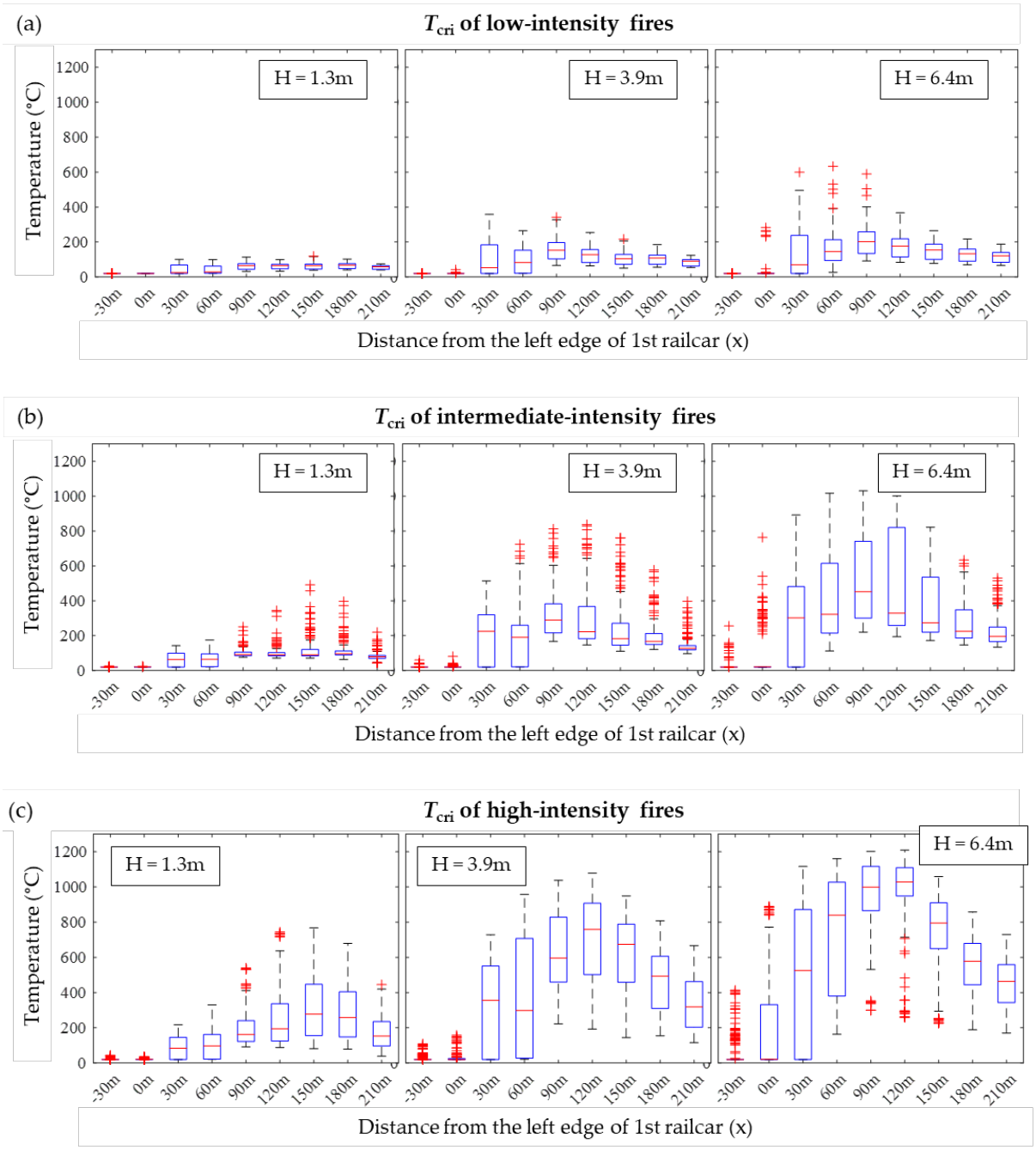

Figure 2.25 Boxplots of T_{cri}

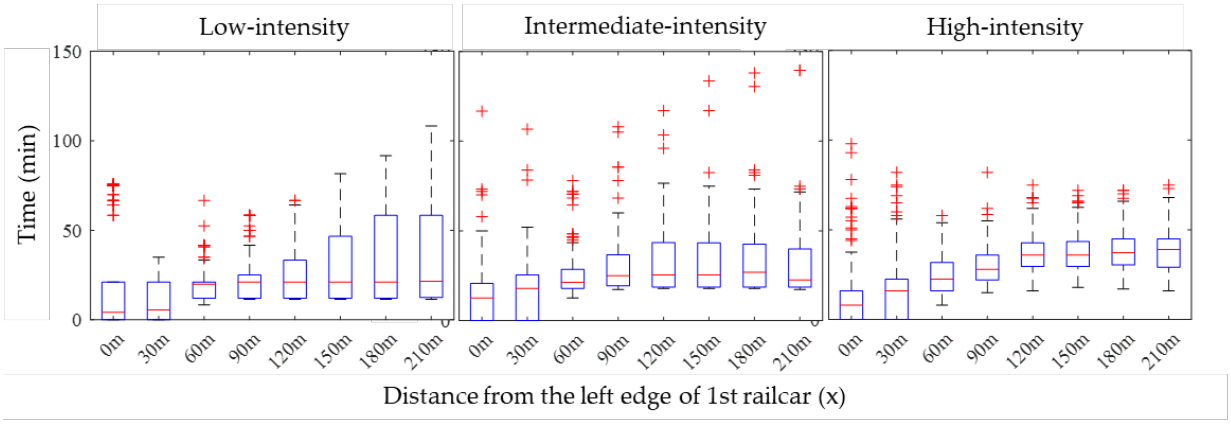

Figure 2.26 Boxplots of t_{cri}

Table 2.12 Statistics of T_{cri} for low-intensity fires

x		-30 m	0 m	30 m	60 m	90 m	120 m	150 m	180 m	210 m
A	Min (°C)	20	20	20	21	32	32	39	40	40
	Max (°C)	20	20	101	99	113	99	119	102	75
	Mean (°C)	20	20	41	41	63	61	64	65	55
	Stan. dev (°C)	0	0	26	24	19	17	17	16	11
B	Min (°C)	20	20	20	20	65	63	51	56	54
	Max (°C)	20	42	358	264	342	255	217	185	124
	Mean (°C)	20	20	102	89	159	129	107	105	85
	Stan. dev (°C)	0	2	98	73	65	46	38	31	20
C	Min (°C)	20	20	20	26	91	83	77	70	65
	Max (°C)	20	282	599	633	589	367	265	217	188
	Mean (°C)	20	29	132	163	207	174	150	128	116
	Stan. dev (°C)	0	44	133	103	87	63	48	38	32

Table 2.13 Statistics of T_{cri} for intermediate-intensity fires

x		-30 m	0 m	30 m	60 m	90 m	120 m	150 m	180 m	210 m
A	Min (°C)	20	20	20	21	76	71	71	63	44
	Max (°C)	26	24	142	175	251	344	492	396	220
	Mean (°C)	20	20	62	60	100	102	119	114	82
	Stan. dev (°C)	0	1	44	41	25	40	70	51	25
B	Min (°C)	20	20	20	21	167	146	110	121	96
	Max (°C)	60	81	514	724	813	838	761	577	397
	Mean (°C)	21	22	186	188	324	304	252	205	144
	Stan. dev (°C)	5	6	167	163	138	178	155	95	50
C	Min (°C)	20	20	20	112	220	194	172	147	134
	Max (°C)	255	764	892	1017	1031	1001	822	634	531
	Mean (°C)	28	83	299	418	522	494	365	274	228
	Stan. dev (°C)	32	137	272	256	245	286	186	120	89

Table 2.14 Statistics of T_{cri} for high-intensity fires

x		-30 m	0 m	30 m	60 m	90 m	120 m	150 m	180 m	210 m
A	Min (°C)	20	20	20	21	92	88	81	78	38
	Max (°C)	44	35	217	330	540	744	768	679	445
	Mean (°C)	21	21	86	102	197	251	311	294	175
	Stan. dev (°C)	4	2	67	86	103	162	178	163	98
B	Min (°C)	20	20	20	21	222	193	144	155	115
	Max (°C)	108	158	729	958	1037	1078	950	807	667
	Mean (°C)	26	28	306	385	626	696	615	471	343
	Stan. dev (°C)	17	24	261	329	226	261	228	184	158
C	Min (°C)	20	20	20	163	299	259	225	188	170
	Max (°C)	413	890	1117	1160	1201	1210	1059	858	729
	Mean (°C)	60	167	483	743	950	982	755	556	456
	Stan. dev (°C)	88	254	405	329	203	207	204	169	146

Table 2.15 Statistics of t_{cri} at the ceiling

x		0 m	30 m	60 m	90 m	120 m	150 m	180 m	210 m
Low-intensity	Min (min)	0	0	8	12	12	12	12	12
	Max (min)	76	208	67	58	67	82	92	108
	Mean (min)	17	19	19	22	26	29	33	35
	Stan. dev (min)	25	42	9	12	15	19	25	27
Intermediate - intensity	Min (min)	0	0	13	17	18	18	18	17
	Max (min)	117	107	78	108	117	134	138	140
	Mean (min)	12	16	26	31	33	33	34	32
	Stan. dev (min)	16	17	12	16	18	19	20	19
High-intensity	Min (min)	0	0	8	15	16	18	17	16
	Max (min)	98	82	58	82	75	72	72	75
	Mean (min)	12	16	24	30	37	37	38	38
	Stan. dev (min)	17	16	10	11	11	11	11	12

The results plotted in Figure 2.25, Figure 2.26, and listed in Table 2.12, Table 2.13, Table 2.14, Table 2.15 demonstrate that:

(1) Fire temperatures in low-intensity fires remain mostly below 300 °C, while temperatures in high-intensity fires can reach as high as 1200 °C. High-intensity fires are expected to cause major damage to the tunnel lining, as will be discussed in the next chapter of this report.

(2) When studying temperatures at different heights, the maximum temperature at the height of 1.3 m mostly remains below 500 °C, hence only mild damage would be expected for the lining sections close to the ground. The tunnel ceiling is expected to have the most fire damage.

(3) Upstream of the fire ($x \leq 0$) remains at ambient temperature in almost all the fire scenarios. This confirms that the calculated critical velocity in the analysis is capable to prevent a backdraft, as required for a passenger railway tunnel, to allow safe evacuation of people. Overall, the critical section with highest temperatures, considering the potential for fire spread, is 120 m downstream of the fire ignition point ($x = 120$ m).

(4) The temperatures in most cases reach peak values within the first 100 minutes. The traveling fire patterns are more prominently observed in high-intensity fires, where the medians of t_{cri} continue increasing along the tunnel length.

2.5 Conclusion

This chapter studied the uncertainties in the influencing parameters of a passenger railway tunnel fire event. The considered parameters included ventilation velocity, amount of fuel in terms of heat release rate (HRR), tunnel slope, ignition point, and ignition criteria for fire spread between passenger train cars. The uncertainties were characterized using available data in the literature or the potential range of the considered parameter. The research investigated 540 fire scenarios (based on a combination of 10 heat release rate values, three ventilation velocities, three slope values, two ignition points, and three fire spread ignition criteria) in a railway tunnel case study to evaluate temporal and spatial evolutions of temperature inside the tunnel. The fire simulations were conducted in Fire Dynamic Simulator (FDS), a computational fluid dynamics software package. The modeling approach in FDS was verified using a scaled tunnel fire experiment and one of the full-scale Memorial Tunnel fire tests. The main contributions of this chapter are summarized as follows:

1. HRR demand for passenger railcars is established from full-scale experimental data.
2. A traveling fire concept, to capture fire spread between railcars in a tunnel, is included when investigating temperature-time evolution of fire inside the tunnel.
3. A range of temperature demands are established from 540 fire scenarios that capture temperature evolution over time across the tunnel length.
4. A tri-linear model was adopted to transform and standardize the simulated temperature-time curves by defining the growth fire rate α_g, decay fire rate α_d, maximum fire temperature T_{max} and the duration of maximum fire temperature t_D. Weibull distributions were used to characterize the four parameters that define the temperature-time curves.
5. Fires with HRRs larger than 40 MW were categorized as high-intensity with the mean maximum temperature of 1007 °C. Fires with HRRs smaller than 30 MW were categorized as low-intensity with the mean maximum temperature of 245 °C.
6. Quantiles of T_{max} for low and high intensity fires were provided. For example, the 90th quantile of the maximum temperature for low- and high-intensity fires were 384 °C and 1170 °C, respectively.
7. Spatial and temporal distributions of fire temperatures were studied and statistically presented using boxplots. Based on the data from 540 simulations, the tunnel section located at 120 m downstream underwent the highest fire demand.

The outcomes of this chapter can be used to make design recommendations for temperature-time curves during passenger railway tunnel fires. The temperature demands are needed for the design of concrete tunnel linings and the associated fire protection requirements based on defined performance levels (e.g., level of damage, downtime) for a railway tunnel fire event.

CHAPTER 3 DAMAGE ASSESSMENT

This chapter describes the introduction of a performance-based approach to characterize potential fire damage to a tunnel structure considering uncertainties in the fire scenario.

In this chapter, the results obtained from 540 simulations (described in Chapter 2) provide the probabilistic-based time-dependent temperature boundary for the tunnel lining sections and serve as the input for analyzing heat propagation within the lining, and the consequent damage assessment of the structure under fire. Damage is defined as the volume of concrete that requires repair following the fire event, as this is a quantity that can be related to downtime. A simplified spalling model is incorporated within thermal and coupled thermo-mechanical analysis to capture damage to the tunnel lining. Statistics of potential damage are reported considering the variations in the fire scenario. Structural analysis of the tunnel section, incorporating soil-tunnel liner interaction, has been performed to demonstrate stability of the tunnel under an extreme fire scenario. The proposed methodology is established for passenger railway tunnels, as related to demand fire scenarios and geometry of the prototype tunnel, but can be extended for application to other tunnel types (e.g., freight).

The proposed methodology in this chapter can be expanded in the future to assess downtime and select proper mitigation measures, such as the design of passive fire protection of tunnel linings to minimize life-cycle costs and improve resilience of the tunnel structure subjected to fire.

3.1 Characterizing damage

The application of a performance-based method leads to designs that would meet pre-defined performance objectives for a structure. The performance objectives can range from collapse prevention for a given design fire scenario, to additional resilience requirements, such

as limited loss of functionality after the fire event. This work is a first step towards defining damage for concrete tunnel linings subjected to fire, where the application can be expanded to further incorporate resilience-based performance objectives.

In this chapter, damage is defined as the volume of concrete that requires repair and replacement. While there is no consensus on a methodology to quantify fire damage to a tunnel lining, similar statements can be found in a number of standards where 300°C is recommended as a threshold for discoloring and reduced residual strength of concrete [30, 31, 85, 86]. Hence, the damaged volume of concrete (DVC) is calculated as the volume of concrete that experiences temperatures above 300 °C. This temperature threshold is also consistent with existing experiments and observations, which show that concrete in excess of 300 °C undergoes permanent material degradation [87-89].

Heat-induced spalling of concrete is broadly observed after real tunnel fire events and can lead to significant concrete losses. Spalling also accelerates the heat transfer process within the lining section, causing a larger fraction of concrete to reach the defined threshold temperature. Hence, the volume of concrete losses for the 540 fire scenarios will be obtained from a series of spalling-incorporated heat-transfer analyses (as described in Sections 3.2, 3.3 and 3.4). To verify structural safety of the tunnel lining during a passenger train fire, the structural stability will be checked against an extreme fire scenario (as described in Section 3.5).

3.2 Modeling of concrete spalling

One challenge in assessing the tunnel fire damage relates to the characterization of the potential heat-induced concrete spalling and numerical modeling of the structure with spalled elements. Existing generic or specialized finite element tools for the analysis of structures at elevated temperatures, such as ABAQUS, ANSYS, and SAFIR, have been verified using fire test data of structural elements [22], but do not capture concrete spalling. This section describes the approach taken in this chapter to incorporate spalling within SAFIR, a finite element code for analysis of structures under fire, to provide a more realistic assessment of fire damage.

3.2.1 Heat-induced spalling of concrete

Heat-induced spalling is a major and common issue for fire performance of concrete structures, and is defined as the violent ejection of pieces from the surface of concrete elements when exposed to rising temperatures [32]. This phenomenon is still not well-understood because of the complex mechanisms involved. The research focusing on the subject is mostly experimental and has shown that while fire spalling of concrete is highly dependent on the concrete material properties, it can also be influenced by other factors, such as the geometry of concrete elements, fire duration and temperature, boundary and restraint conditions, and the externally applied loads [90-95]. Although it has been experimentally proven that adding a small amount of polypropylene (PP) fibers in the concrete mix could effectively reduce or prevent heat-induced spalling [9, 10, 12, 13], the mechanisms behind the process are not well understood.

Some researchers have developed spalling mechanism models to assist computational studies by looking into the macro- and micro- levels of concrete behavior when exposed to elevated temperatures [26, 96-98]. Two major theories are considered in these models: thermal stress induced spalling and pore-pressure induced spalling [1, 99, 100]. Although these advanced coupled thermo-hydro-chemo-mechanical codes can account for a variety of parameters, they are unable to accurately predict spalling for a given concrete mix under certain mechanical demands and heating regimes.

Given the complex nature of this thermal-mechanical-physical-chemical phenomenon, and the numerous influencing factors on the process, full- or large-scale experiments would provide the best support to help the research community understand heat-induced concrete spalling. There is an increasing trend in the last two decades to experimentally study fire spalling of concrete tunnel segments around the world, as listed in Table 1.1. These tests are conducted on full-scale tunnel segments or slabs, mostly serving as fire resistance tests in tunneling projects.

3.2.2 Simplified spalling model

Based on the above discussion, this study assumes that, for a given location of tunnel lining exposed to a certain temperature demand, the heat-induced concrete spalling is a gradual and uniform process with a constant spalling rate (i.e., spalling depth changes linearly with time, specified with a unit of mm/min). Thus, the spalling process is characterized using three factors: spalling start time (t_{start}), spalling rate (R_s), and the spalling end time (t_{end}), as shown in Figure 3.1:

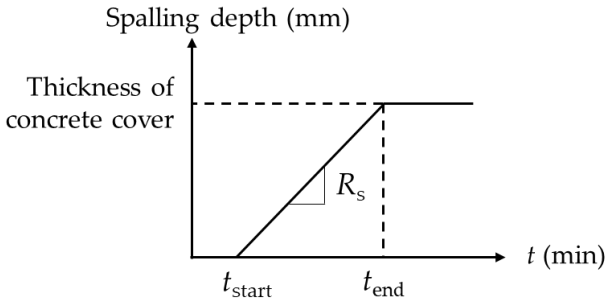

Figure 3.1 A simplified concrete spalling model

3.2.3 Data from existing experiments

While large-scale experiments provide the most reliable data on potential spalling of tunnel segments, the number of investigated specimens is quite limited. This is primarily due to the high costs and safety requirements involved in large-scale fire testing. Further, most of the tests mentioned above use extreme fire curves (RWS, Hydrocarbon, Modified Hydrocarbon or RABT), the majority of which represent fuel, oil, or petrol tanker fires in worst-case scenarios and could reach 1000 °C within the first five minutes [4]. Although these standard curves are used in practice to design for tunnel fires, they might be too conservative for passenger train or metro fires given the nature of fuel and results of previous CFD analyses. The heating rates for extreme cases from the CFD analyses, with temperatures reaching 1000 °C, are mostly between 20 °C/min to 50 °C/min.

Hence, the collected data to quantify t_{start}, R_s, and t_{end} has been expanded to include small- and intermediate- scale tests as well as those tests under less-intense fire curves (e.g., ISO 834). Table 3.1 provides the detailed experimental data obtained from published literature. Most data sets are from a compilation reported by the International Workshops on Concrete Spalling due to Fire Exposure, which is a workshop held bi-annually, and publishes recent results in

experimental research to advance the understanding of spalling under various conditions [21, 101].

Table 3.1 Experimental spalling test data from published literature

Reference	Specimen No.	Specimen type	Fire scenario	Spalling start time (min)	Spalling start temp. (°C)	Spalling duration (min)	Max. spalling depth (mm)	Spalling rate (mm/ min)
[13]	1	Slab	RWS	3	890	80	250	3.125
	2	Slab	RWS	2	580	70	270	3.857
	3	Slab	RWS	2	580	60	200	3.333
	4	Slab	ISO 834	5	576	50	150	3.000
	5	Slab	ISO 834	6	603	50	150	3.000
	6	Slab	RWS	1.5	435	112	220	1.964
	7	Slab	RWS	1.5	435	95	220	2.315
[16]	8	Tunnel segment	ISO 834	6-20	718	N/A	42	N/A
	9	Tunnel segment	ISO 834	6-20	718	N/A	51	N/A
	10	Tunnel segment	ISO 834	6-20	718	N/A	26	N/A
	11	Tunnel segment	ISO 834	6-20	718	N/A	38	N/A
[102]	12	Slab	ISO 834	14	728	N/A	N/A	N/A
[103]	13	Slab	HC	0.75	678	2	9	4.500
	14	Slab	HC	0.5	568	2	10	5.000
	15	Slab	HC	0.8	694	2	5	2.500
	16	Slab	HC	1	743	2	8	4.000
	17	Slab	HC	1	743	2	10	5.000
	18	Slab	HC	2	843	2	5	2.500
	19	Slab	HC	2	843	2	8	4.000
	20	Slab	HC	0.75	678	2	10	5.000
	21	Slab	HC	1	743	2	8	4.000
	22	Slab	HC	1	743	2	5	2.500
[104]	23	Slab	ISO 834	5-7	550	35	45	1.286
	24	Slab	ISO 834	5-7	550	35	35	1.000
	25	Slab	ISO 834	5-7	550	35	65	1.857
	26	Slab	ISO 834	5-7	550	35	55	1.571
	27	Slab	ISO 834	5-7	550	35	40	1.143
	28	Slab	ISO 834	5-7	550	35	50	1.429
[105]	29	Column	ISO 834	20	781	N/A	N/A	N/A
	30	Column	ISO 834	12	705	N/A	N/A	N/A
	31	Column	ISO 834	10	678	N/A	N/A	N/A
	32	Column	ISO 834	20	781	N/A	N/A	N/A

	33	Column	ISO 834	12	705	N/A	N/A	N/A
	34	Column	ISO 834	20	781	N/A	N/A	N/A
[106]	35	Slab	ISO 834	10-15	728	10-20	20-60	1.667*
	36	Slab	ISO 834	10-15	728	10-20	20-60	1.667*
	37	Slab	ISO 834	10-15	728	10-20	20-60	1.667*
	38	Slab	ISO 834	10-15	728	10-20	20-60	1.667*
	39	Slab	ISO 834	10-15	728	10-20	20-60	1.667*
	40	Slab	ISO 834	10-15	728	10-20	20-60	1.667*
	41	Slab	ISO 834	10-15	728	10-20	20-60	1.667*
	42	Slab	ISO 834	10-15	728	10-20	20-60	1.667*
	43	Slab	ISO 834	10-15	728	10-20	20-60	1.667*
	44	Slab	ISO 834	10-15	728	10-20	20-60	1.667*
	45	Slab	ISO 834	10-15	728	10-20	20-60	1.667*
	46	Slab	ISO 834	10-15	728	10-20	20-60	1.667*
[107]	47	Slab	ISO 834	17	757	N/A	N/A	N/A
	48	Slab	ISO 834	15	738	N/A	N/A	N/A
	49	Slab	RWS	3	890	N/A	N/A	N/A
[108]	50	Slab	HC	2	793	N/A	N/A	N/A
	51	Slab	HC	3	865	N/A	N/A	N/A
	52	Slab	ISO 834	11	692	13	38	2.923
	53	Slab	ISO 834	10	678	16	50	3.125
	54	Slab	ISO 834	11	692	15	50	3.333
	55	Slab	ISO 834	11	692	16	42	2.625
	56	Slab	ISO 834	12	705	11	38	3.455
	57	Slab	ISO 834	14	728	13	35	2.692
	58	Slab	ISO 834	12	705	19	65	3.421
	59	Slab	ISO 834	11	692	18	53	2.944
	60	Slab	ISO 834	12	705	18	58	3.222
	61	Slab	ISO 834	14	728	13	46	3.538
	62	Slab	ISO 834	16	748	15	69	4.600
	63	Slab	ISO 834	10	678	21	60	2.857
	64	Ring-shape	ISO 834	18	766	14	40	2.857
	65	Ring-shape	ISO 834	14	728	8	27	3.375
	66	Slab	ISO 834	6	603	N/A	N/A	N/A
	67	Slab	ISO 834	9	662	N/A	N/A	N/A
	68	Slab	ISO 834	7	625	N/A	N/A	N/A
	69	Slab	ISO 834	12	705	15	31	2.067
	70	Slab	ISO 834	12	705	11	18	1.636
[109]	71	Column	ISO 834	6	603	24	40	1.667
	72	Column	ISO 834	13	717	24	55	2.292
	73	Column	ISO 834	13	717	23	54	2.348
	74	Column	ISO 834	7	625	6	25	4.167
	75	Column	HCM	7	1170	N/A	N/A	N/A
	76	Column	HCM	8	1190	N/A	N/A	N/A

	77	Column	HCM	8	1190	N/A	N/A	N/A
	78	Column	HCM	5	1119	N/A	N/A	N/A
	79	Column	HCM	4	1086	N/A	N/A	N/A
	80	Column	HCM	4	1086	N/A	N/A	N/A
	81	Column	HCM	5	1119	N/A	N/A	N/A
[19]	82	Slab	HCM	4	1087	N/A	400	5-7*
	83	Slab	HCM	4	1087	N/A	400	5-7*
	84	Slab	HCM	2	996	N/A	315	5-7*
[110]	85	Slab	ISO 834	10	678	40	51	1.275
	86	Slab	ISO 834	10	678	40	99	2.475
	87	Slab	ISO 834	10	678	40	42	1.050
	88	Slab	ISO 834	10	678	40	56	1.400
[11]	89	Prismatic samples	ISO 834	15	739	10	38	3.800
	90	Prismatic samples	ISO 834	12	705	10	22	2.200
	91	Prismatic samples	ISO 834	15	734	10	19	1.900
	92	Prismatic samples	ISO 834	10	668	12	28	2.333
	93	Prismatic samples	ISO 834	8	645	12	12	1.000
	94	Prismatic samples	ISO 834	9	663	12	17	1.417
	95	Prismatic samples	ISO 834	13	717	12	8	0.667
	96	Prismatic samples	ISO 834	9	663	12	8	0.667
	97	Prismatic samples	ISO 834	6	596	10	14	1.400
	98	Prismatic samples	ISO 834	6	603	10	6	0.600
	99	Prismatic samples	ISO 834	5	576	10	5	0.500
	100	Prismatic samples	ISO 834	6	603	10	8	0.800
	101	Prismatic samples	ISO 834	7	610	10	12	1.200
				Mean:	735		Mean:	2.69

Note: the spalling rate is calculated by the authors, except for those marked with *.

Table 3.1 shows that specimens tested under Hydrocarbon (HC), Hydrocarbon Modified (HCM), or RWS fire curves typically experience spalling within the first five minutes of fire because of the high heating rate. These specimens also have a higher spalling rate (> 2.5 mm/min).

Specimens under less-intense fire conditions (e.g., ISO 834) mostly start to spall after 10-15 minutes and have a relatively mild spalling rate (1 to 3 mm/min).

This research characterizes the spalling starting time as a function of gas temperature. That is, when the gas temperature in proximity of the tunnel lining reaches the spalling starting temperature, the concrete lining will begin to spall. Table 3.1 lists the spalling starting temperatures for all the tests, which are calculated by the reported spalling starting time and the corresponding fire curve in the test. Compiling the data, the spalling starting temperature is set at 740 °C and the spalling rate is set at 2.6 mm/min, with both values taken as the mean of the experimental values listed in Table 3.1.

Data that could be used to determine the endpoint of the spalling process is quite limited, as many experiments were terminated shortly after the first indication of spalling. For modeling purposes, this work assumes that spalling ceases when the first reinforcement layer is exposed, with the assumption that the reinforcement will provide some level of confinement to reduce the rate of spalling. This assumption is consistent with the experimental findings, where reinforcement mesh slows down or prevents spalling from progressing further within the cross-section [13]. The approach and assumptions presented in this research can be adjusted to integrate additional future experimental results to improve the spalling model.

3.3 MATLAB/SAFIR interactive code

In order to incorporate the described fire spalling model within the thermo-mechanical finite element analysis, a fine mesh has been created in SAFIR, for which the concrete cover of the reinforced concrete section is composed of relatively fine layers of concrete fibers to enable proper removal of concrete when spalling occurs. Figure 3.2 shows the concrete lining with overall depth of 0.3 meters. Before spalling starts ($0 \leq t \leq t_{start}$), the concrete cover is composed of 10 layers. During the spalling phase ($t_{start} \leq t \leq t_{end}$), the mesh nodes and fiber elements of the cover can be deleted layer by layer, where this process is controlled by the spalling rate. The fire exposed surface (i.e., the temperature boundary) of the section is also updated at every time step given the

spalled layers. The concrete removal process ceases after spalling stops ($t \geq t_{end}$), and the section remains constant until the fire ends.

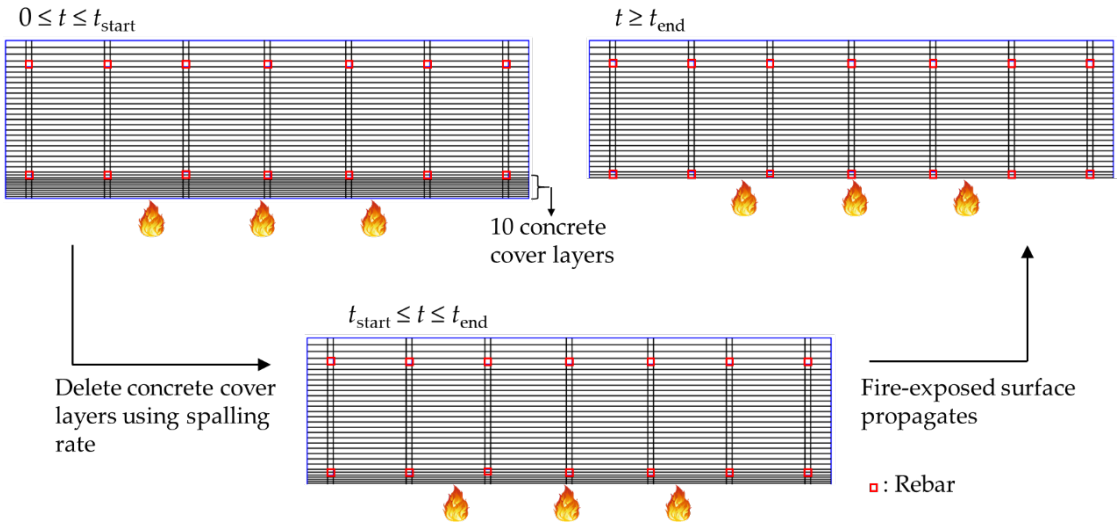

Figure 3.2 Finite element mesh in SAFIR for modeling concrete spalling

An interactive MATLAB/SAFIR script has been coded to control and repeat the heat transfer process when applied to different fire scenarios. The MATLAB code writes and updates the input file for SAFIR over the duration of fire as spalling occurs. The code automatically generates input files for the SAFIR thermal analysis, indicates whether spalling occurs, removes concrete layers based on the spalling rate, updates the input file and the thermal boundary given the removed concrete layers, restarts SAFIR to continue the thermal analysis, and finally reads output files from SAFIR for damage quantification. A flowchart describing the process is shown in Figure 3.3.

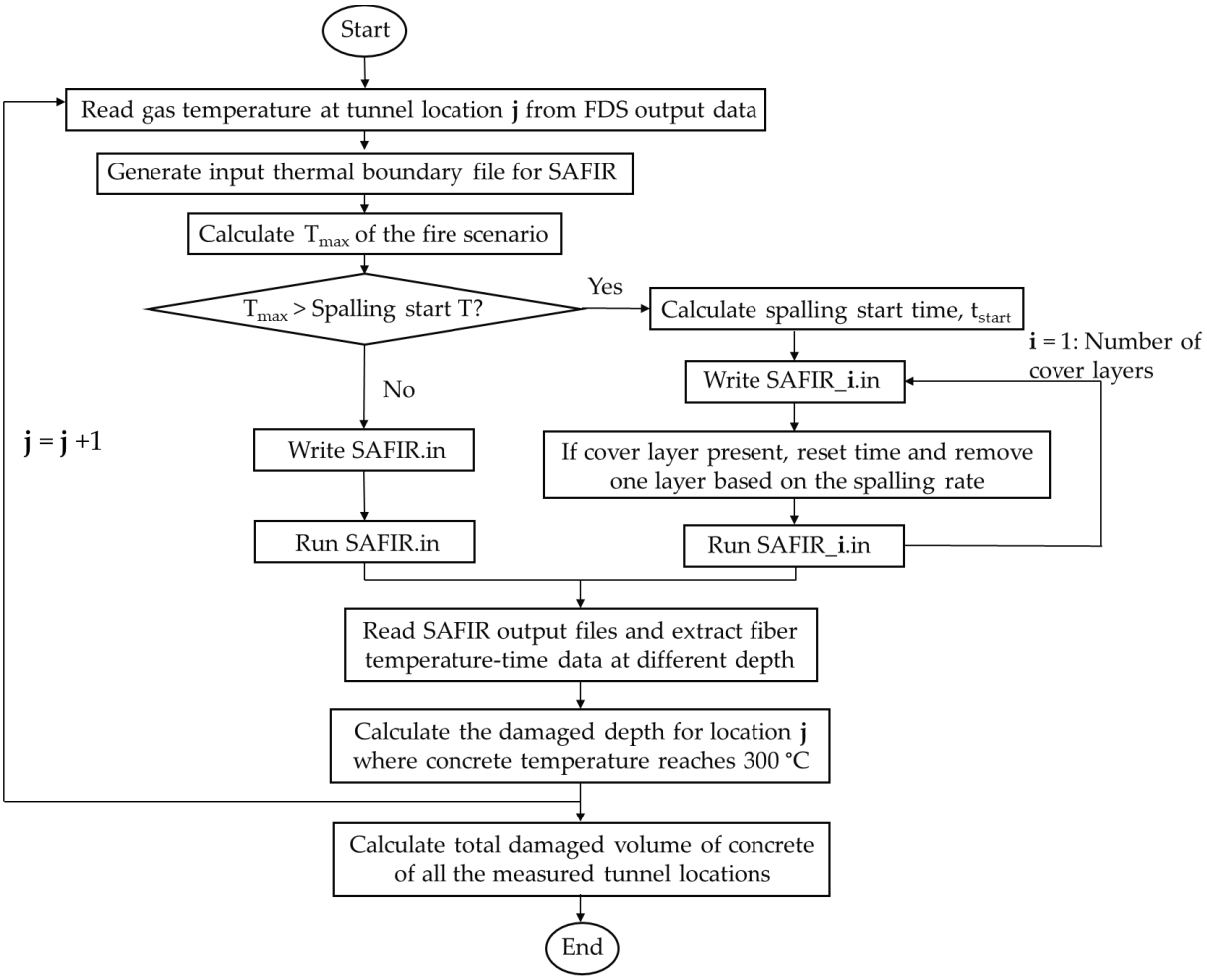

Figure 3.3 MATLAB/SAFIR interactive code to incorporate spalling

3.4 Damaged volume of concrete (DVC)

This section studies the volume of concrete loss for the 540 fire scenarios based on the results of heat-transfer analyses using SAFIR and incorporating spalling. The section losses can originate from two criteria: spalling induced concrete losses and heat-induced losses where concrete temperature exceeds 300 °C, as discussed in Section 3.1. Figure 3.4 shows the total damaged volume of concrete (DVC) for the tunnel, calculated as the summation of damaged concrete volumes at all investigated sections at different heights and along the tunnel length. The results are shown for the three considered fire categories. The statistics of calculated DVC are presented in Table 3.2.

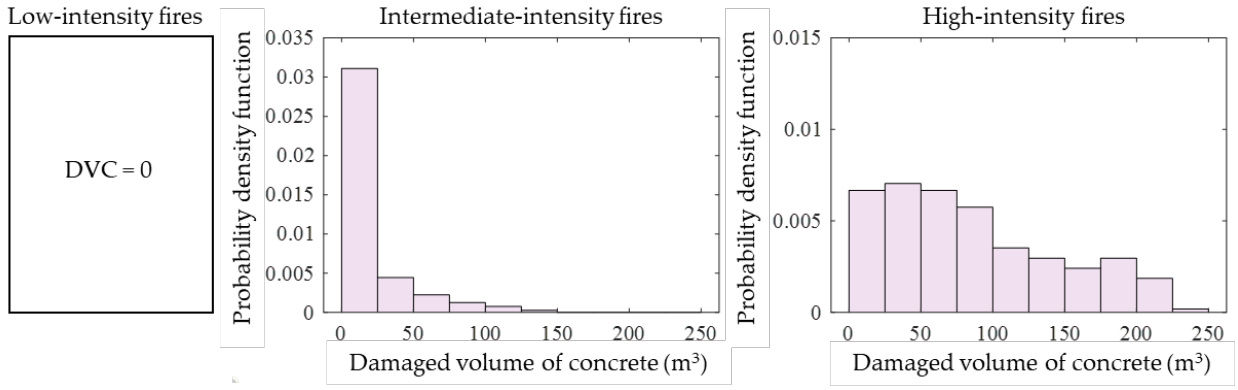

Figure 3.4 Probability density functions for DVC including spalling

Table 3.2 Statistics of DVC including spalling

Category	Intermediate-intensity	High-intensity
Min. (m^3)	0 (65/162 cases)	0 (6/216 cases)
Max. (m^3)	130	226
Mean (m^3)	16	86
Stan. dev (m^3)	27	61

The results, as discussed earlier, show that low-intensity fires do not cause any damage to the tunnel lining given their mild fire temperatures. Approximately 60% of intermediate fires cause some level of damage to the tunnel lining, while the remainder cause zero damage. More than 97% of high-intensity fires result in concrete damage.

Extensive repair work would be needed after high intensity fires. The capacity of a common concrete mixer truck is generally about 6.1 m^3. The maximum calculated DVC for high-intensity fires is 226 m^3, which is equivalent to 37 concrete trucks needed to repair the damaged sections of the tunnel. The mean DVC of 86 m^3 translates to 14 concrete trucks. The normalized value of DVC for the worst-case scenario, with respect to the total volume of concrete within the affected 260 m of the tunnel section is 16%. The value of DVC provides an understanding of how much material would need to be replaced after a fire, as well as a reference for predicting the potential labor cost, downtime, and economic losses from service interruptions.

The influence of concrete spalling is investigated by again calculating DVC, this time assuming no concrete spalling in the analysis. Figure 3.5 and Table 3.3 summarize values of DVC

without spalling. When comparing the DVCs with and without spalling, it is clear that the occurrence of spalling significantly increases damage. For example, the mean DVC for high-intensity fires increases by 69% due to concrete spalling. This observation emphasizes the necessity of incorporating spalling into fire damage analyses for more realistic assessment. The results can also be interpreted as lower and upper bounds of damage given the level of uncertainty in predicting spalling.

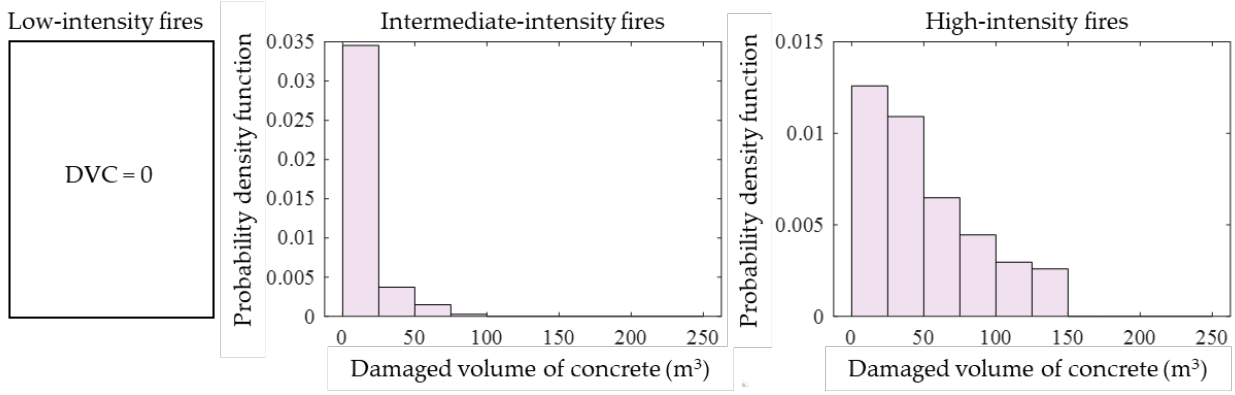

Figure 3.5 Probability density functions for DVC with no spalling

Table 3.3 Statistics of DVC with no spalling

Category	Intermediate-intensity	High-intensity
Min. (m^3)	0 (75/162 cases)	0 (6/216 cases)
Max. (m^3)	76	142
Mean (m^3)	10	51
Stan. dev (m^3)	17	38

Using the same methodology, DVC has also been calculated for the same tunnel assuming the crown is exposed to the RWS (lasts for three hours without cooling) and RABT-ZTV (a train fire that lasts for three hours including cooling) fire curves. With spalling considered, the depths of damaged concrete sections are 0.14 m and 0.12 m under RWS and RABT fires, respectively (note that the concrete lining is 0.3 m thick). Assuming that the same fires affect 130 m of the tunnel ceiling (approximate length of five railcars), the calculated DVCs for the RWS and RABT fires are 252 m^3 and 216 m^3, respectively. This analysis illustrates that using the standard fire curves for damage assessment could lead to unrealistic and uneconomic decisions.

3.5 Structural stability

3.5.1 SAFIR thermo-mechanical analysis

This section investigates the structural performance of the tunnel under extreme fire scenarios using SAFIR's thermo-mechanical analysis. Figure 3.6 shows the two-dimensional beam-spring model of the Howard Street tunnel cross section (as discussed in Section 3.1) for structural analysis. The model consists of 26 two-dimensional beams and 25 spring elements. The tunnel base is approximately 11 m below grade and is modeled as fixed-fixed. The tunnel deformation in the longitudinal direction is assumed to be zero, and the two-dimensional model will provide a conservative assessment of tunnel performance under fire.

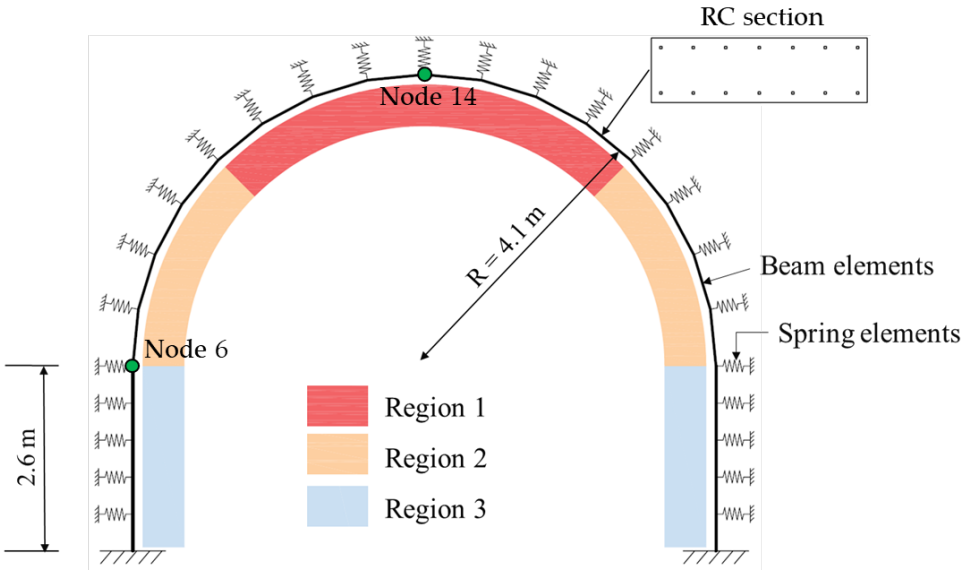

Figure 3.6 Beam-spring model of the tunnel for structural analysis

One of the most intense temperature profiles from the 540 FDS simulations is selected to study stability of the structure (HRR_{max}: 55MW, ventilation velocity: 2.45 m/s, tunnel slope: 0.0, ignition temperature criteria for fire spread: 300 °C, fire starts in the first car from the North portal, temperature measured at 120 m downstream). If structural stability of the tunnel is verified for an extreme fire scenario, it can be assumed that the tunnel structure will not collapse under less severe cases. As shown in Figure 3.6, the tunnel section is divided into three regions to account for the variance in gas temperature across the height. Region 1 (the crown) is identified as the

hottest region during a fire, and the "high heat" section from the heat transfer analysis (using the temperature boundary that is measured at point A in Figure 2.16) is assigned to this region. Accordingly, Regions 2 and 3 are assigned the sections that corresponds to points B and C in Figure 2.16, respectively. Figure 3.7 shows the temperature curves used in this section, with the fire taking about six hours to completely cool down to ambient temperature. For comparison purposes, the structural analysis has also been completed assuming that Regions 1 and 2 are subjected to the standard RWS fire (Figure 3.7) for three hours while Region 3 remains at ambient temperature.

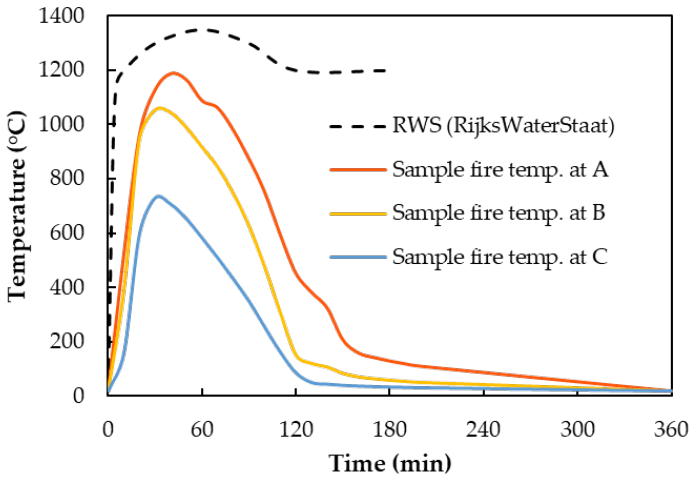

Figure 3.7 Fire curves assigned to the tunnel section for structural analysis

As for the material properties, at ambient temperature, the compressive strength of concrete is 45 MPa and the tensile strength is assumed to be zero. The tensile yield strength of the reinforcement is 414 MPa. The stress-strain material relationships for every fiber in a section is generated taking into account material type (steel or concrete), temperature, and the corresponding mechanical properties. Material degradation factors are taken into account for the structural analysis. The temperature-dependent material properties from EN 1992-1-2 [111] are applied to both concrete and steel. The constitutive material model for concrete is based on the modified Eurocode 2 concrete model with an explicit transient creep term [112].

The applied loads on the tunnel include self-weight, vertical earth pressure, horizontal earth pressure, and live load from the street above the tunnel. In this study, the density of

reinforced concrete is 2500 kg/m^3, unit weight of soil is 15 kN/m^3, lateral earth pressure coefficient is 0.6, and the applied live load is 23.9 kN/m^2 [113].

The compression-only springs (Figure 3.6) are used to model soil-tunnel liner interaction. The spring stiffness (K_s) is calculated based on Equation 3.1, as a function of tunnel radius R, modulus of elasticity E, and Poisson's ratio ν of the surrounding soil [25]. Assuming a clay soil, E and ν are taken as 30 MPa and 0.4, respectively. The soil properties can be varied in future studies to investigate effects of soil type and temperature-dependent soil properties on the fire performance of a tunnel. The springs are only activated when the tunnel expands outward, placing the springs in compression.

$$K_s = \frac{E}{(1+\nu)R} \tag{3.1}$$

For each fire scenario, the structural analysis is performed considering both "with spalling" and "no spalling" cases, to obtain lower and upper bound responses. It should be noted that spalled layers cannot be removed from the finite element mesh during the structural analysis in SAFIR. Therefore, the spalling-induced section losses within the structural model are represented by assigning a fiber temperature of 1200 °C to spalled layers – the temperature at which concrete loses all material strength and stiffness [111] – effectively removing the material from the analysis. Overall, four simulations have been conducted: "RWS - no spalling", "RWS - spalling", "FDS - no spalling", and "FDS - spalling".

3.5.2 Results

Generally, the structural response for tunnels under fire is governed by the combination of several mechanisms. Initially, the load-induced stresses in the intact structure are due to the soil overburden and applied external loads. When the fire starts and heat propagates through the lining sections, thermally-induced axial forces and moments (due to the thermal gradient) are generated. Simultaneously, the non-uniform material degradation close to the fire-exposed surface makes the section weaker and changes the center of stiffness of the section. The axial restraint within a section also changes with time as the temperature increases, and the

surrounding structure heats up. The following will present results from the analysis of two fire scenarios, and investigate the structural response for fires with and without a cooling phase. The tunnel response will be studied at the crown, as well as for the full tunnel section.

First, the temperature, strain, and stress distributions at the tunnel ceiling – which experiences the largest fire demand – are investigated. Figure 3.8 and Figure 3.9 show the results for RWS and FDS fires, respectively. Data extracted from different time steps are provided to illustrate the effect of heat propagation within the section, where "t" represents the time after which the fire starts. Figure 3.8 a, b and Figure 3.9 a, b show the temperature distributions across the section; Figure 3.8 c, d and Figure 3.9 c, d provide the strain profiles; and Figure 3.8 e, f, and Figure 3.9 e, f provide the stress profiles. The left columns in the figures present results from the "no spalling" analysis, whereas the right columns present results from the "spalling" analysis. Note that the strain shown here is the mechanical strain, calculated as the difference between the total and thermal strains.

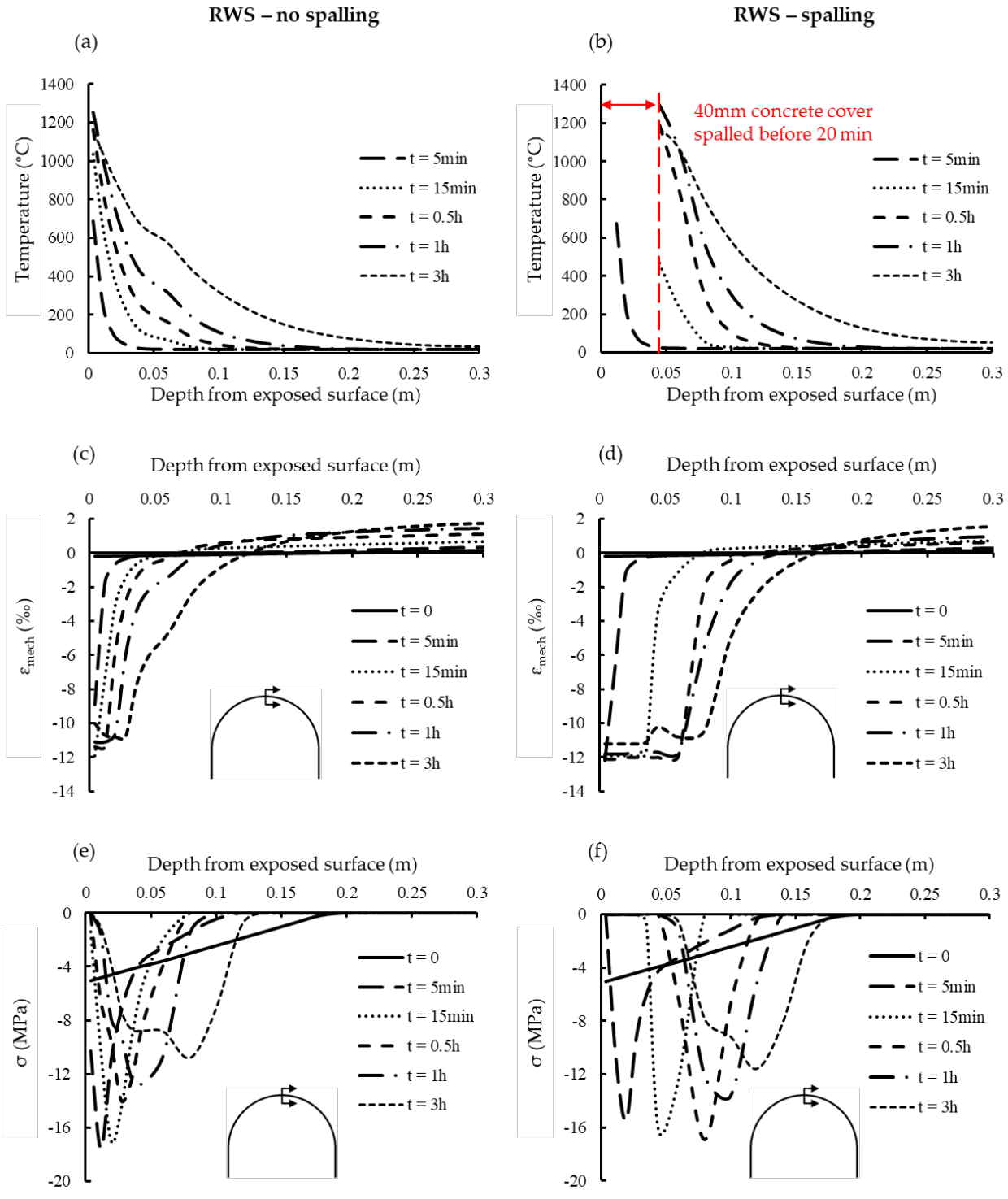

Figure 3.8 Temperature, strain, and stress evolution in the tunnel crown section subjected to the RWS fire scenario

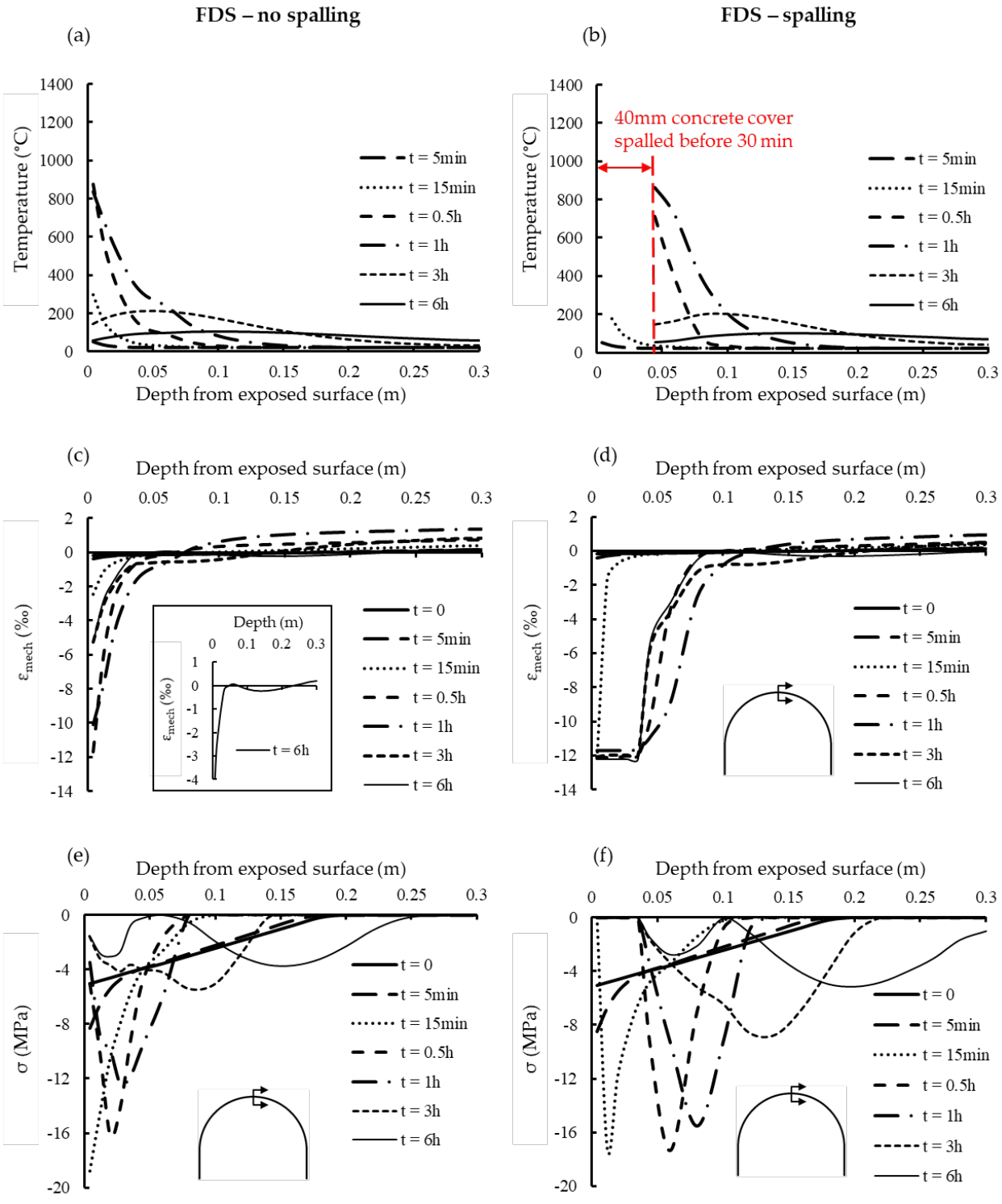

Figure 3.9 Temperature, strain, and stress evolution in the tunnel crown section subjected to the sample FDS fire scenario

Before the fire starts (t = 0), the demand load on the tunnel structure includes the overburden and externally applied loads, with the majority of the crown section in compression, as expected. The "RWS – no spalling" scenario (Figure 3.8 a, c and e) shows that the temperature of the exposed surface heats up rapidly during the early stages of the RWS fire, while the rest of the section remains at ambient temperature. The large temperature difference along section depth generates a thermally-induced moment and significantly increases the compressive strain near the hot surface. The compressive stress in concrete starts to follow a bell-shape as the hotter side of concrete is softened due to temperature, which is consistent with other studies [114]. As more heat propagates within the concrete, the temperature gradient within the section is less prominent, yet the thermally-induced axial compressive force increases due to a higher average temperature within the section. Therefore, the bell-shaped stress profile becomes wider across the section. At the end of the fire (t = 3h), the peak of bell-shaped stress profile moves to 0.08 m from the fire-exposed surface, implying that at least 0.08 m of the concrete section undergoes material softening, which is not recoverable [114]. Figure 3.8 b, d, and f, show the effect of concrete spalling on the process, and how spalling would accelerate the temperature increase within the section, shifting the bell-shaped stress profile. Figure 3.8 b indicates that all of the 0.04 m concrete cover spalls before 20 minutes, causing deeper concrete fibers to undergo compression. The peak of bell-shaped stress profile moves to 0.12 m within the section at 3 hours, implying that an additional 0.04 m of concrete thickness is damaged because of spalling.

The stress distribution within the tunnel ceiling element subjected to the sample FDS fire (Figure 3.9) follows a trend similar to the RWS fire during the heating phase. When the fire temperature starts to decay, the exposed boundary surface cools down slowly, while deeper concrete fibers within the section maintain heat due to the low thermal conductivity of concrete, as shown in temperature plots at "t = 3h" and "t = 6h" in Figure 3.9 a and b. The level of thermal shrinkage due to cooling is governed by the temperature profile within the section. The mechanical strain is influenced by the residual strains as well as the constraint imposed by the rest of the structure. This explains the changes in direction of mechanical strain within the concrete section at t = 6h (Figure 3.9 c). The strain profile at t = 6h follows the temperature distribution at the depths of 0.05 m to 0.3 m from the fire-exposed surface; however, the surface

concrete within 0.05 m of the exposed boundary cannot reverse back to the tensile region due to irrecoverable residual strains. The stress distribution during the cooling phase of fire follows a double-bell shape. Concrete close to the fire-exposed surfaced is severely damaged during heating, and exhibits an extreme softening behavior. The rest of the section follows the strain distribution and undergoes less softening. It is harder to determine the depth of section which undergoes material softening during the cooling phase, given that the strain profile switches directions. Hence, the damaged depth is calculated at t = 1h, about 20 minutes after the end of heating. The damaged depths are calculated as 0.03 m and 0.08 m for the "FDS – no spalling" and "FDS – spalling" scenarios.

Table 3.4 summarizes the calculated damaged depth of concrete within the crown section of the tunnel using the two methods: (a) the temperature threshold of 300 ˚C (Section 3.1), and (b) the stress analysis discussed above. The comparison of results from the four cases shows that the temperature threshold of 300 ˚C provides a more conservative estimation of damage. However, it is challenging to implement damage assessment using stress analysis during the cooling phase; thus, the results most probably underestimate damage. Finally, the damaged volume of concrete calculated using the 300 ˚C threshold (i.e., temperature correlation) can be further supported considering that concrete damage is mostly due to the dehydration process at elevated temperatures [115, 116].

Table 3.4 Damage assessment using temperature and stress calculations

Methodology	RWS – no spalling	RWS – spalling	FDS – no spalling	FDS – spalling
Temperature based	0.10 m	0.14 m	0.05 m	0.09 m
Stress based	0.08 m	0.12 m	0.03 m	0.08 m

Figure 3.10 presents the evolution of moments in the tunnel structure for the four considered scenarios. Figure 3.10a shows the moment demand at ambient temperature as a reference point (moment is plotted on the tension side). At the initial stage, when the tunnel is at ambient temperature, the crown tends to bend outward while the spring-line element tends to bend inward. Once the fire starts, the exposed side of the section wants to expand but the cooler

part restrains the section, resulting in compressive stresses in the hot side of the section and tensile stresses in the cooler part, shifting the moment to the outward direction. At later stages of the fire, the moment decreases as the temperature gradient within the section decreases. Finally, the moment reverses direction during the decay phase of fire as shown in Figure 3.10 d and e. Cases with spalling generally experience smaller moments, since heat propagates through the sections faster, and the temperature tends to be more uniform within the sections.

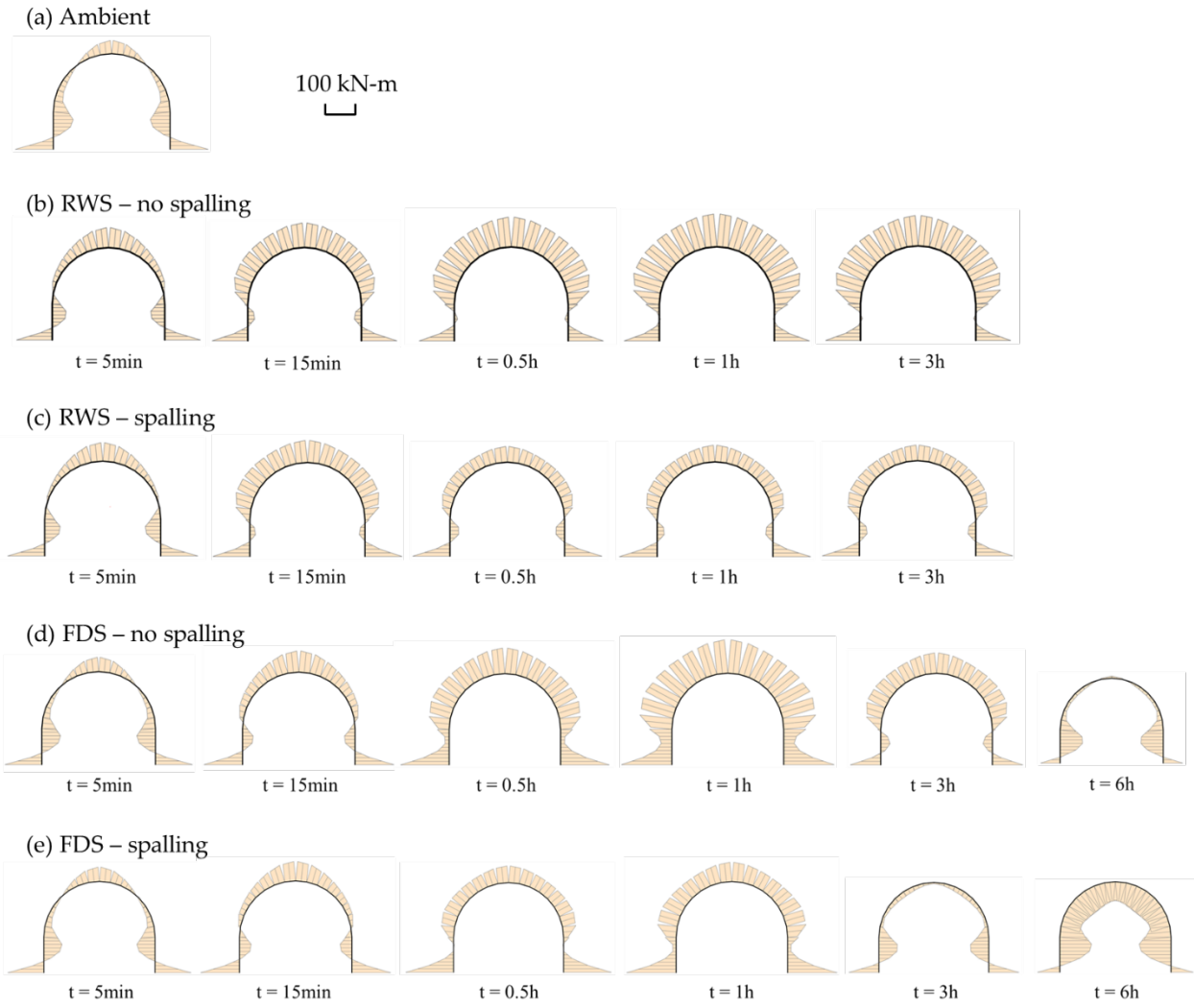

Figure 3.10 Evolution of moment diagrams for the tunnel structure during fire

Displacements over time for two locations have been recorded to understand the deformation of the tunnel structure under fire: one is the vertical displacement of the crown (node 14 marked in Figure 3.6), and the other is the horizontal displacement of the spring-line (node 6

marked in Figure 3.6). Figure 3.11 presents displacements for the two fire scenarios, with or without spalling conditions, and showing the location and direction of recorded displacements. The results show that the structure moves upwards at the crown and bends inward at the spring-line during the heating phase, as expected based on the moment diagrams in Figure 3.10.

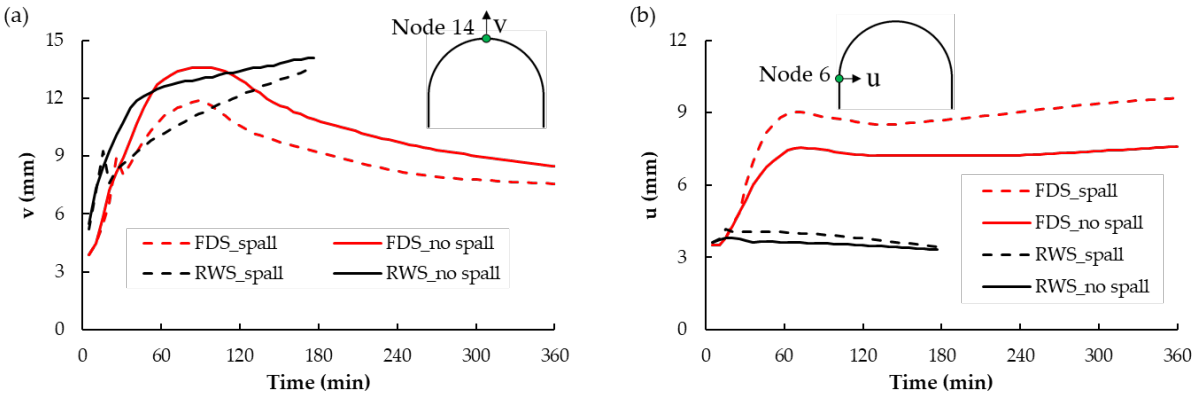

Figure 3.11 Displacements of (a) crown and (b) spring-line under fire

Overall, none of the considered fire scenarios resulted in structural instability of the tunnel, as the load is redistributed within the cross section to the cooler side of the concrete lining. The arch shape of the tunnel also helps, transferring loads in compression and preventing a tensile failure of the structure. However, the delayed response and propagation of heat within the section due to low thermal conductivity of concrete should be noted. The FDS fire scenario in Figure 3.7 reaches peak temperatures at approximately 40 minutes, while the maximum deflection occurs after 1 hour. Similar observations were also found when discussing the stress distribution within the crown element. These findings are consistent with studies on concrete building structures exposed to fire [117]. Understanding the delayed temperature distribution within the concrete structure is significant when considering life safety of emergency responders.

3.6 Conclusion

This chapter provided a framework to quantify damage during a passenger train tunnel fire event, considering the uncertainties within the fire scenario, as well as incorporating a spalling model for damage assessment. The spatial and temporal distributions of fire temperature

within the tunnel obtained from Chapter 2 are transferred as input data to the SAFIR heat transfer analysis. The damage was captured by calculating the volume of concrete that exceeded 300 °C. The spalling-incorporated heat transfer analysis used an interactive MATLAB/SAFIR code that included data-driven criteria for the initiation of spalling, spalling rate, and ending point. Finally, the stability of the tunnel was evaluated based on structural analysis of the tunnel section under an extreme fire scenario.

The low-intensity fires did not reach high temperatures and consequently did not cause any damage. Intermediate- and high-intensity fires caused damage, with the maximum calculated damaged volume of concrete (DVC) for high-intensity fires being 226 m^3. This value is equivalent to 37 concrete trucks that are needed to repair the damaged sections of the tunnel. The results also showed that spalling has a significant effect on damage assessment. Although the incorporated spalling model is simplified, the comparison of results with and without spalling can provide upper and lower bound assessments of damage. Structural analysis of the tunnel section confirmed stability of the tunnel structure under an extreme fire scenario, as was also observed in historical events, where collapse has rarely occurred. However, it was noted that the maximum demand within the tunnel section was not observed until the fire was in the cooling phase, which is due to low thermal conductivity of concrete.

The proposed framework in this chapter can be integrated within probabilistic risk-assessment methods to guide the design of fire protection for concrete linings. The first step in such procedure is to quantify the probability of having a high intensity fire based on the type of railcars passing through the tunnel. Given the probability of hazard (i.e., frequency of the fire scenario and its intensity), concrete damage (as discussed in this chapter) and consequently the corresponding downtime of the tunnel can be evaluated. Combining the probability of hazard with the associated consequences (i.e., losses) provides an assessment of risk. The decision to incorporate fire protection (if any) and the corresponding design should be based on the comparison of the calculated risk versus the acceptable risk that is agreed with the stakeholders.

CHAPTER 4 EXPERIMENTAL INVESTIGATION OF HEAT-INDUCED SPALLING OF CONCRETE

4.1 Introduction

As mentioned in the previous chapters, one of the main disadvantages of concrete is that when it is subjected to fire, concrete spalling may occur, which is defined as the separation of concrete fragments due to the thermal instability of the material [118]. Protecting concrete tunnel liners against spalling in practice should be carefully studied; thus, many researchers have been experimentally and numerically investigating the process [119].

One of the main solutions proposed to address this spalling issue is the use of additives in the concrete mixture, which improves the fire resistance of concrete against severe fire scenarios. The two most common additives used for this purpose are polypropylene and steel fibers, which rely on different mechanisms to mitigate the thermal spalling of concrete. It is well understood that, in the absence of polypropylene fibers, the concrete surface cracks and pressure due to water vapor builds up within concrete when it is exposed to a high level of heat [120, 121]. If the water vapor pressure exceeds the tensile strength of concrete, then spalling occurs. Polypropylene fibers dissipate some of the built-up pressure as they melt at about 170°C, creating more space within the micro-structure of concrete [122].

Studies on the influence of steel fibers provide contradictory conclusions. The goal of adding steel fibers is to create entrapped air bubbles that would contain the excess vapor when pressure builds up [123]. Also, steel fibers increase the tensile strength of concrete and therefore decreases the chance of spalling. Although there are studies in favor of adding steel fiber to address concrete spalling [124] other researchers concluded that steel fibers do not prevent thermal spalling [125].

In this chapter, an experimental investigation of the effect of adding polypropylene and steel fibers on concrete spalling is presented. For this purpose, four different concrete mixtures were utilized. Concrete specimens with dimension of 350 mm x 350 mm x 200 mm were cast and placed against an electrical furnace to heat up the concrete up to 1000 °C. Concrete spalling was

visually assessed, and the spalling depth and percentage of weight loss were measured. During the experiments, the temperature inside the concrete specimens was measured at different depths in order to obtain the temperature gradient inside the section. It was observed that the temperature inside the concrete for the specimens with concrete spalling was substantially higher than those without spalling. Although the effect of the steel fibers on thermal spalling was minimal, the polypropylene fibers at higher densities were capable of effectively preventing spalling.

4.2 Material and test scheme

In this section, the materials used for making the concrete specimens, the concrete properties and the characteristics of the testing equipment are comprehensively described.

The concrete mixture composition was designed based on the ACI design criteria to achieve a 28-day compressive strength of 35 MPa. 0 shows the designed concrete mixture by weight for 1 cubic meter of concrete. Adding fibers would slightly change the values in 0. The cement to water to coarse aggregate to sand mixture ratio was 1:0.46:1.3:1.57, and the average unit weight of the concrete was 2,580 kg/m^3.

Table 4.1 Concrete mixture composition by weight in 1 m^3

Water (kg/m^3)	Cement (kg/m^3)	Fine Aggregate (kg/m^3)	Coarse Aggregate (kg/m^3)
240	520	680	820

All the specimens were made of ordinary Portland cement (OPC). Crushed river stones with a maximum size of 20 mm were used to make the concrete. Properties and morphologies of the polypropylene and steel fibers heavily depend on the production methods and can change drastically depending on the producer. Both fibers used in this study were acquired from Nycon. The polypropylene fiber was a macro-fibrillated type with the commercial name of Procon-F. This fiber meets the standards required by the ASTM C-1116. Table 4.2 contains the properties of the polypropylene fiber used in this study.

Table 4.2 Properties of the polypropylene fiber

Tensile strength (MPa)	Flexural Strength (GPa)	Filament diameter (mm)	Length (mm)	Aspect ratio	Melting point (°C)	Elongation (%)
410	5.6	1.52	19	12.5	160	25

A continuously deformed stainless-steel fiber commercially denominated as SSF-Type V was used. This fiber, with relevant properties shown in Table 4.3, meets the requirement of the ASTM A820 standard.

Table 4.3 Properties of the steel fiber

Tensile strength (MPa)	Flexural Strength (GPa)	Filament diameter (mm)	Length (mm)	Aspect ratio	Melting point (°C)	Elongation (%)
1030	203	1.18	3.8	32.2	1516	3~4

Five different mixtures were designed for this study. Three mixtures include 1, 2, and 3 kg/m^3 of polypropylene fiber, one mixture contains 20 kg/m^3 of steel fiber and the control mixture included no fiber. Two specimens were tested for each mixture in order to evaluate the repeatability of the test results. Table 4.4 presents the detailed information of each tested concrete specimen. Figure 4.1 shows the polypropylene and steel fibers used in this study.

Table 4.4 Mixture of the concrete specimens containing fiber

Specimen Name	Fiber	Density (kg/m^3)	Compressive strength (MPa)	Slump (cm)
C	None	-	35.3	12.5
PP1	Polypropylene	1	34.6	9.6
PP2	Polypropylene	2	34.0	9.2
PP3	Polypropylene	3	33.5	8.3
S10	Steel	10	35.8	5.1

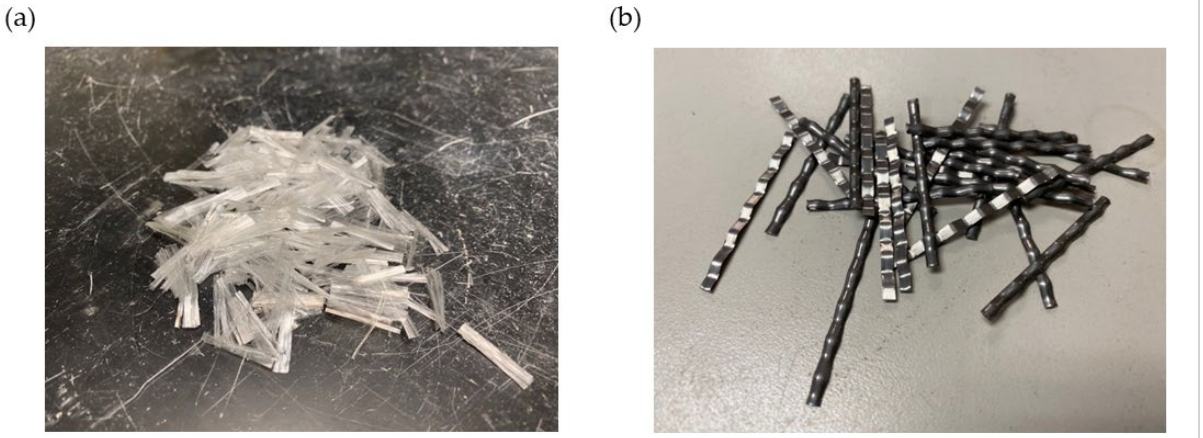

Figure 4.1 Photo of (a) polypropylene and (b) steel fibers used in the experiments

The cross-section of each concrete specimen was 350 mm x 350 mm, with a setback close to the perimeter to match the furnace opening, as shown in Figure 4.2. Each specimen had a thickness of 200 mm. The cross-section was dictated by the size of the furnace opening, while the thickness was dictated by the weight capacity of the equipment used to move the concrete specimens. Also, 200 mm is a common thickness used in other spalling tests [126], which will facilitate subsequent comparisons. Each specimen was cured in a 20°C humid chamber for 21 days. Five holes were drilled in each specimen at different depths in order to measure the temperature inside of the specimens. Figure 4.3 illustrates the pattern and location of each hole in the specimen. In order to measure the temperatures inside of the concrete, K-type thermocouples with a maximum measurable temperature of 1100 °C and accuracy of ±5 °C were used (Figure 4.4a). In order to protect the furnace from concrete spalling, a stainless-steel shield was built and installed inside the furnace (Figure 4.4b). Also, two clamps were employed to minimize the heat loss in the system, particularly where the concrete is in contact with the furnace (Figure 4.4c).

Figure 4.2 Side view of the specimen showing a setback on the front (heated) side of a specimen

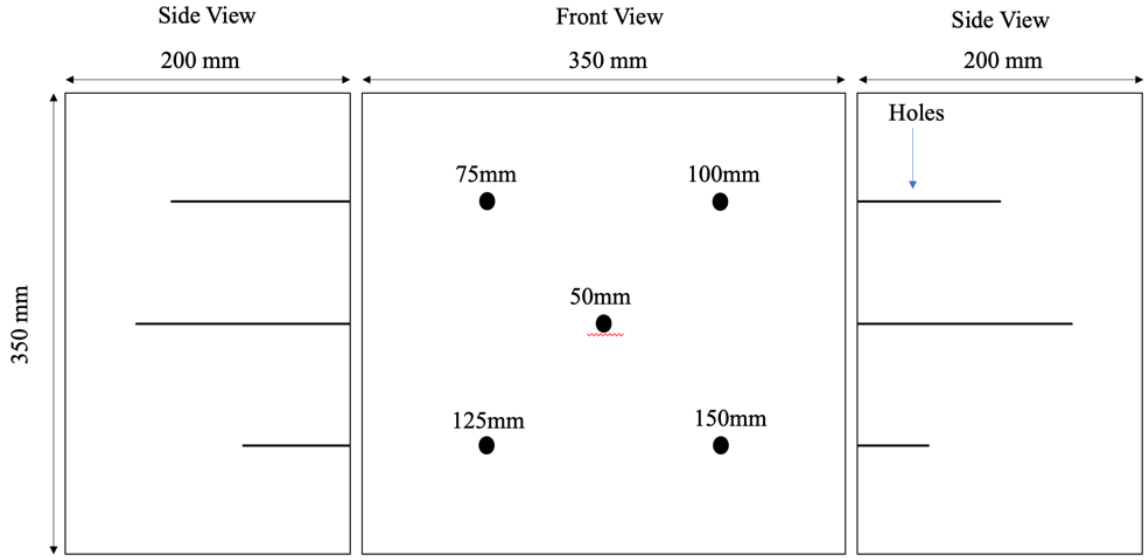

Figure 4.3 Hole pattern to insert the thermocouples for temperature measurements

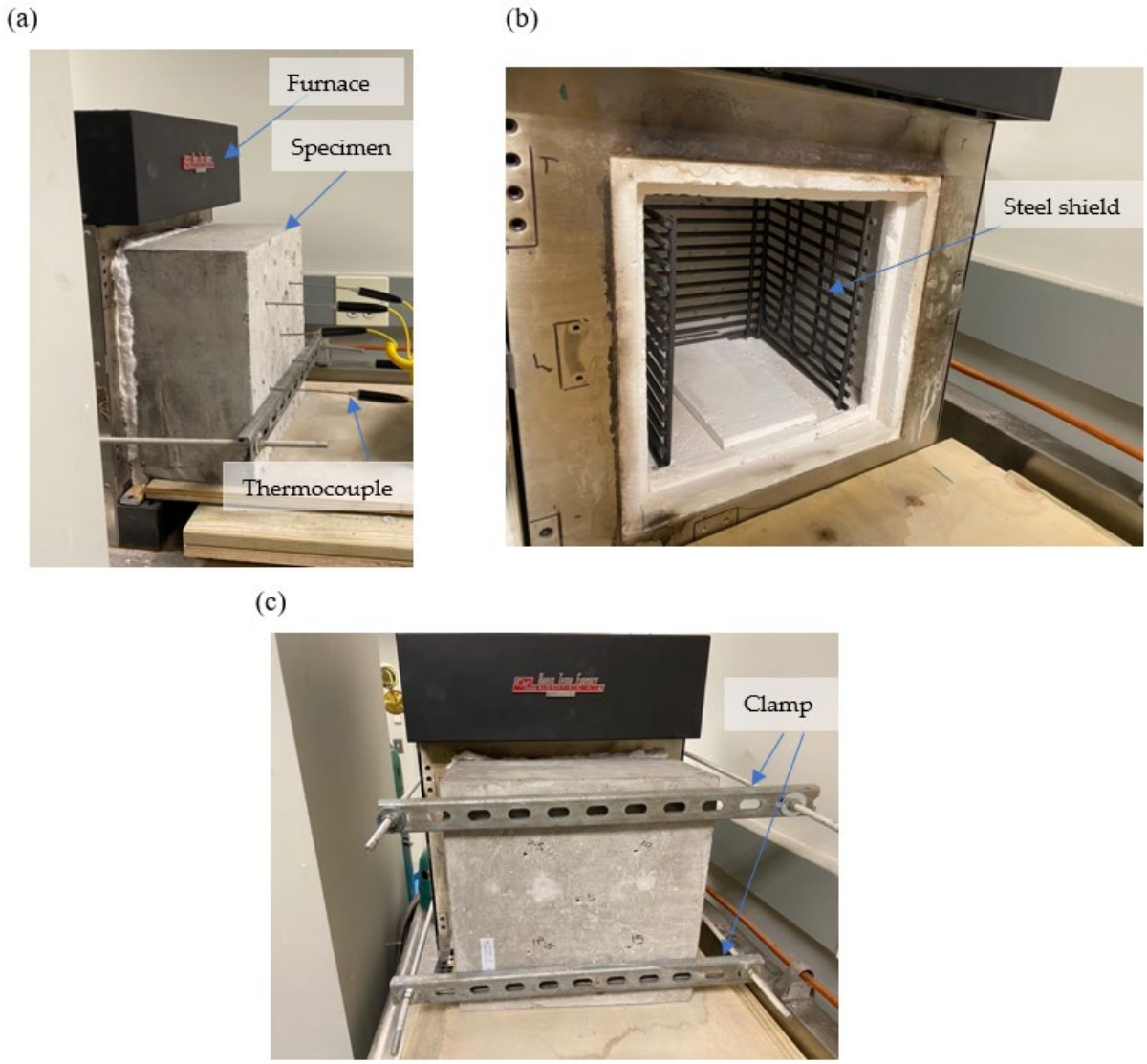

Figure 4.4 Test setup showing (a) side view of the furnace, ceramic isolator, concrete specimen, clamp, and thermocouples (b) steel shield inside the furnace to protect furnace from violent concrete spalling (c) clamps connecting the specimens to the furnace

An electric furnace with an opening of 200 mm x 200 mm was used for the experiments. The furnace has six coils capable of raising the temperature to 1600 °C. The average heating rate used in the tests is shown in Figure 4.5, where it is compared to the ISO 834 fire curve. The rate of heating used in the tests is lower than the ISO 834, primarily due to equipment limitations. The weights of each specimen were measured and recorded before and 24 hours after the experiment.

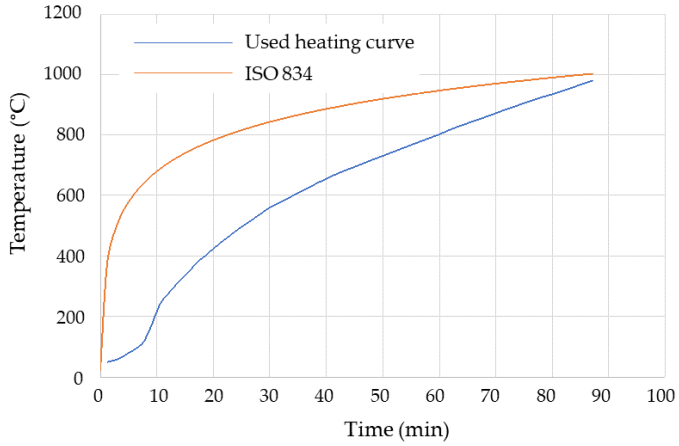

Figure 4.5 Temperature vs time curve used in the experiments versus the ISO 834 fire curve

4.3 Results and discussion

This section presents the results of the study. First, the overall experimental observations are discussed, followed by the cases in which spalling occurred. Subsequently, the temperature gradient inside the concrete is analyzed.

4.3.1 Experimental observations

During the experiments, no significant observation was made for temperatures up to 480 °C with respect to spalling. From this point on, the sound of occasional spalling events could be heard in the specimens in which spalling occurred. Also, cracks gradually developed on the sides of all specimens. The major cracks were located in the middle of the side edges of the specimens, as shown in Figure 4.6. The development of these fractures was followed by water coming out of the cracks. All the explosive spalling events happened at temperatures between 550 °C and 600 °C. From about 600 °C to 700 °C, the amount of water appearing on the surface of the specimen grew significantly as the fractures further propagated. Also, moisture started to come out of some of the temperature measuring holes. From 700 °C to 850 °C, the accumulated moisture on the surface of the specimen evaporated and steam started to come out of the fractures and, in some

cases, also from the temperature measuring holes. No significant spalling events occurred during the increase of temperature from 850 °C to 1000 °C and no water was observed during this period.

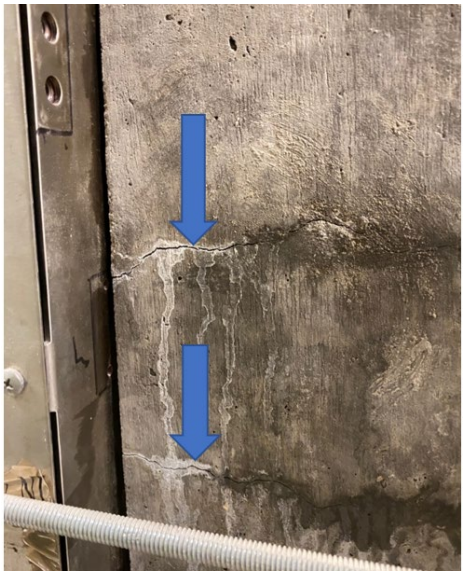

Figure 4.6 Fractures and traces of water on the side of a specimen

4.3.2 Severity of spalling and weight loss

The extent of concrete spalling on different specimens is shown in Figure 4.7. Spalling occurred in three out of five specimens, namely in the control specimen, PP1, and S10. It is clear that by increasing the density of polypropylene fibers, the tendency of thermal spalling decreases. This corresponds well to what has been observed in the literature [120]. The steel fibers had a minimal effect on the spalling severity. Table 4.5 presents the average mass loss and the maximum depth of spalling for each mixture. The control specimen experienced the most severe spalling, as expected, with a mass loss of 5.6% and a maximum spalling depth of 29 mm. The S10 specimen showed the most severe spalling after the control specimen, with a mass loss of 4.31% and a maximum spalling depth of 25 mm. The specimens with a higher density of polypropylene fibers (2 kg/m^3 and 3 kg/m^3) did not experience any spalling. The mass loss in these specimens was 2.8% and 2.5%, respectively. However, the mass loss in the specimen with 1 kg/m^3 of polypropylene fiber was 3.7% with a maximum depth of spalling of 17 mm.

C

S10

PP1

PP2

PP3

Figure 4.7 Extent of concrete spalling for the tested specimens

Table 4.5 Mass loss and maximum depth of spalling for each mixture

Specimen	Weight loss (%)	Weight loss reduction (%)	Maximum depth of spalling (mm)	Reduction in spalling depth (%)
C	5.60	-	29	-
PP1	3.70	33.7	17	41.3
PP2	2.77	50.5	<2mm	~100
PP3	2.48	55.7	0	100
S10	4.31	23.0	25	13.7

4.3.3 Temperature change inside the concrete

In general, we can subdivide the temperature transfer inside of the specimens into two categories, namely "without spalling" and "with spalling". Figure 4.8 shows the temperature change at different depths of the concrete section over time for S10 and PP3 specimens, as representative examples of the categories "with spalling" and "without spalling", respectively. It can be observed that, towards the end of the tests, the temperatures in the specimens with spalling is considerably higher than the specimens without spalling at all measured depths. Spalling removes pieces of the concrete, which would act as barrier to the heat; thus, heat can penetrate faster within the concrete section. As it can be seen from Figure 4.8a, a considerable jump in temperature can be observed after initial spalling in the S10 specimen. Finally, the time that heat takes to reach different points inside the specimen provides an understanding of the heat transfer rate inside the concrete section.

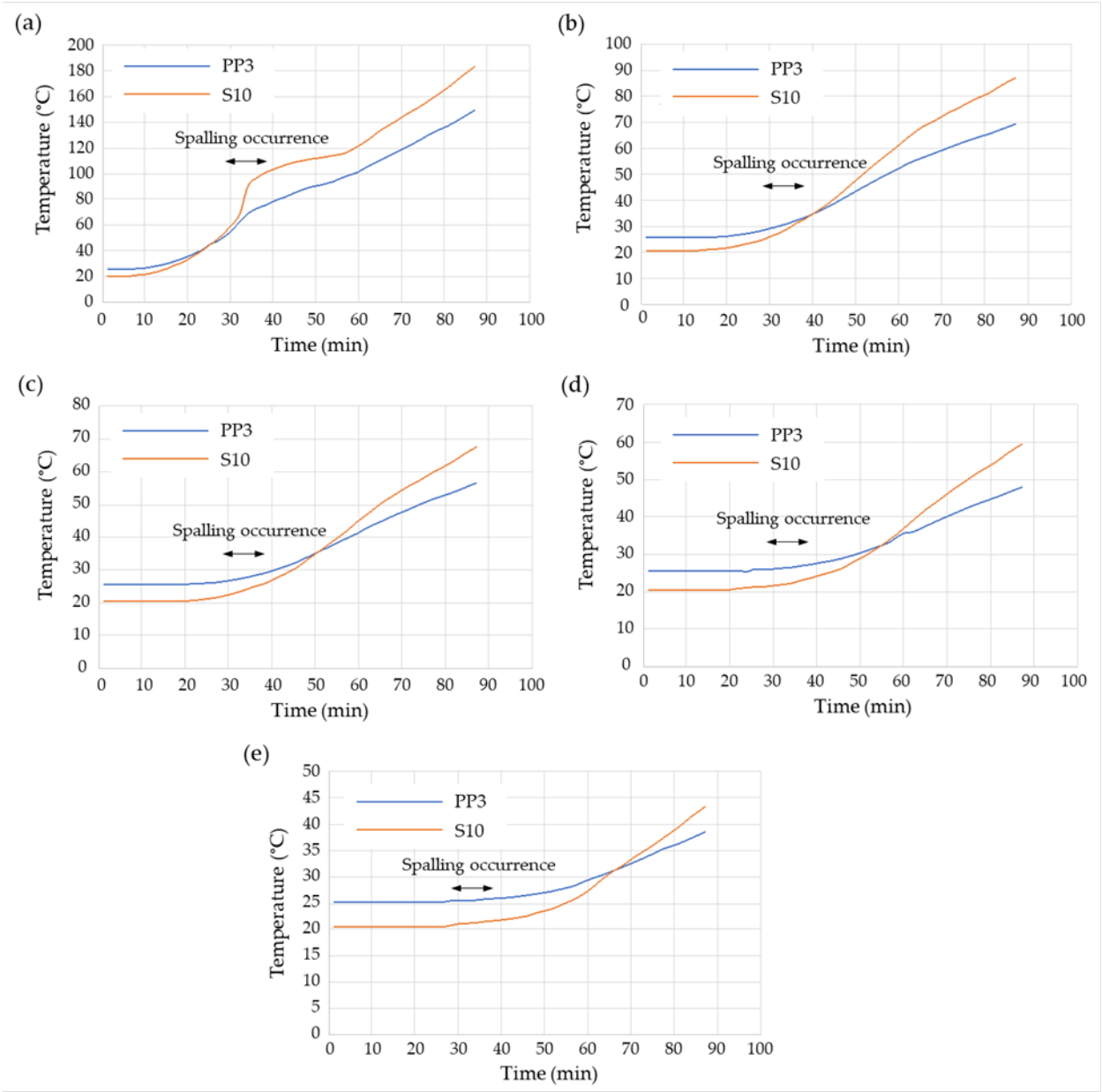

Figure 4.8 Temperature vs time plots for S10 and PP3 specimens at depths a) 50mm, b) 75mm, c) 100mm, d) 125mm, e) 150mm

Figure 4.9 shows the temperature change inside the PP3 specimen versus time. It can be seen that, at 50 mm from the heated concrete face, a noticeable temperature change starts to occur at 8 minutes of the test. Also, at 75 mm, 100 mm, 125 mm and 150 mm from the heated face of the concrete, changes in temperature started at 15, 19, 22, and 26 minutes, respectively.

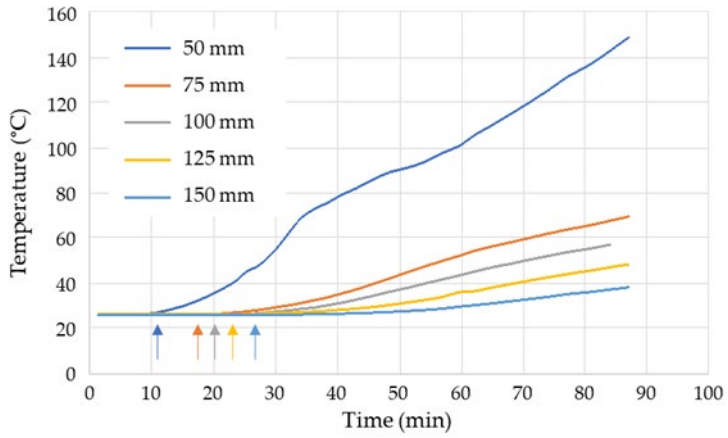

Figure 4.9 Temperature vs time curve at different depths of specimen PP3, arrows represent the time when the temperature starts to increase at each depth

4.4 Summary and conclusions

The effect of different densities of polypropylene fibers and steel fibers on the thermal spalling of concrete was investigated. The following conclusions were reached:

1) Using steel fibers for decreasing spalling is not an effective solution since the steel fibers decreased the spalling minimally when compared to the control specimen. It only decreased the weight losses by 23% and the maximum depth of spalling by 13.7%. Moreover, adding steel fibers leads to lower workability of the concrete (low slump), which is not desirable.

2) It was observed that adding more than 2 kg/m^3 of polypropylene fiber prevented the concrete spalling completely. However, at the lower density of 1 kg/m^3, minor concrete spalling was still observed.

3) This study illustrated that in the cases with spalling, the temperature inside the specimen was substantially higher than specimens without spalling. This could increase the risk of damage for tunnels by further reduction in the strength of concrete and exposure of steel reinforcement.

CHAPTER 5 EXPERIMENTAL INVESTIGATION OF FIRE DAMAGE TO REINFORCED CONCRETE SLABS

5.1 Introduction

This chapter presents the experimental investigation of four restrained and loaded large-scale reinforced concrete tunnel slabs. As summarized in Chapter 1, there is an increasing trend in studying fire performance of tunnel segments/slabs in the past two decades. Among the published studies, large-scale tests have provided the most realistic findings and contributed valuable knowledge to the community. Most of the existing large-scale tests focused on the influence of concrete mixes (e.g., adding fibers, optimizing aggregate sizes) on spalling behavior. Combined with other material-level and intermediate-scale tests, one can conclude from these studies that polypropylene (PP) fiber reduces heat-induced spalling more effectively when comparing to other types of fibers (e.g., polyvinyl alcohol (PVA) fibers and steel fibers) [17, 127].

In practice, the extreme standard fire curves without a decaying phase, such as the RWS and modified hydrocarbon curves, are mostly being adopted as the test fire scenarios. Although the residual deformation and capacity of a tunnel structure after fire plays an important role in deciding the tunnel's serviceability and resilience, there is very limited research available on specimen behavior during or after the cooling phase. Moreover, except for material properties of concrete, fire damage to tunnel lining segments can be influenced by many other factors, as introduced in Chapter 1. To mimic the realistic condition of an in-situ tunnel segment as much as possible, the restraint level (as provided by the rest of the structure) and loading condition (i.e., earth pressure) should be carefully incorporated in tests, whereas only a few fire tests have considered such factors.

The experimental investigation in this chapter aims to study the effects of three parameters on fire damage to the ceiling (typically the mostly damaged area) of a tunnel lining through furnace tests on four large-scale RC slabs: (1) addition of polypropylene (PP) fiber type that is commonly available in the US market (SIKA PPM-150 fiber), (2) level of restraint (induced using post-tensioned prestressed strands), and (3) duration of the maximum temperature. The

three investigated parameters are designed to reflect realistic scenarios and provide insightful results for evaluating tunnel damage. The design process of the specimens and test programs are introduced in Section 5.2.1 and Section 5.3, in accordance with available fire test guidance documents [128, 129].

5.2 Experimental set-up

5.2.1 Test specimens

(i) Overview

The test specimens include: (1) four 2440 mm x 1830 mm x 300 mm (8′ x 6′ x 1′) flat reinforced concrete slabs for furnace testing, and (2) 12 small-scale 200 mm x 100 mm x 100 mm (8″ x 4″ x 4″) concrete cylinder samples for determining concrete compressive strength and moisture content. The schematics of the four slabs (TS 1-4) are presented in Figure 5.1 through Figure 5.3. Specimens TS 1-3 are cast with a concrete mix including 0.22% (by volume) PP fibers to study its effect on spalling and test specimen TS 4 is designed with conventional concrete. Two levels of axial restraint are considered in this test by using three (TS 2) and six (TS 1, 3, and 4) centric post-tensioned strands, respectively. All of the slab specimens have the same reinforcement layout.

The concrete used in this test has a nominal compressive strength of 55 MPa (8 ksi). The PP fibers are SikaFiber PPM-150, monofilament polypropylene fibers with two lengths of 12.7 mm and 19.1 mm. Table 5.1 presents the mix proportions of concrete. The mild steel is Gr.60 - ASTM A615/A615M [130] with a nominal yield strength of 414 MPa (60 ksi) and Young's modulus of 200 GPa (29,000 ksi). The post-tensioning strands are cold-drawn, low-relaxation 7-wire strands in accordance with Gr.270 - ASTM A416/A416M [131], with an ultimate stress of 1861 MPa (270 ksi).

Table 5.1 Concrete mix proportions

Specimen No.	Cement (kg/m³)	Mineral addition (kg/m³)	Friction sand (kg/m³)	Coarse aggregate (kg/m³)	w/c	PP fiber (kg/m³)
TS 1-3	314	104	661	1056	0.34	2
TS 4	314	104	661	1056	0.34	0

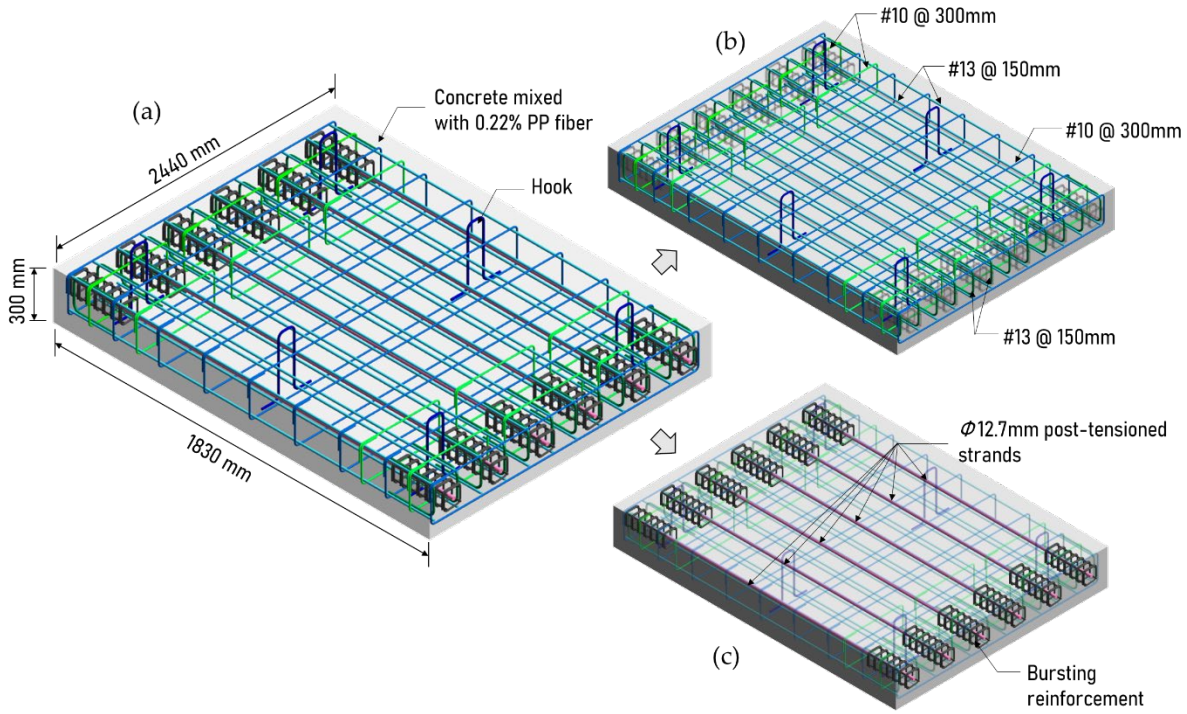

Figure 5.1 (a) Dimension, (b) reinforcement, and (c) unbonded prestressing details of TS 1 and TS 3

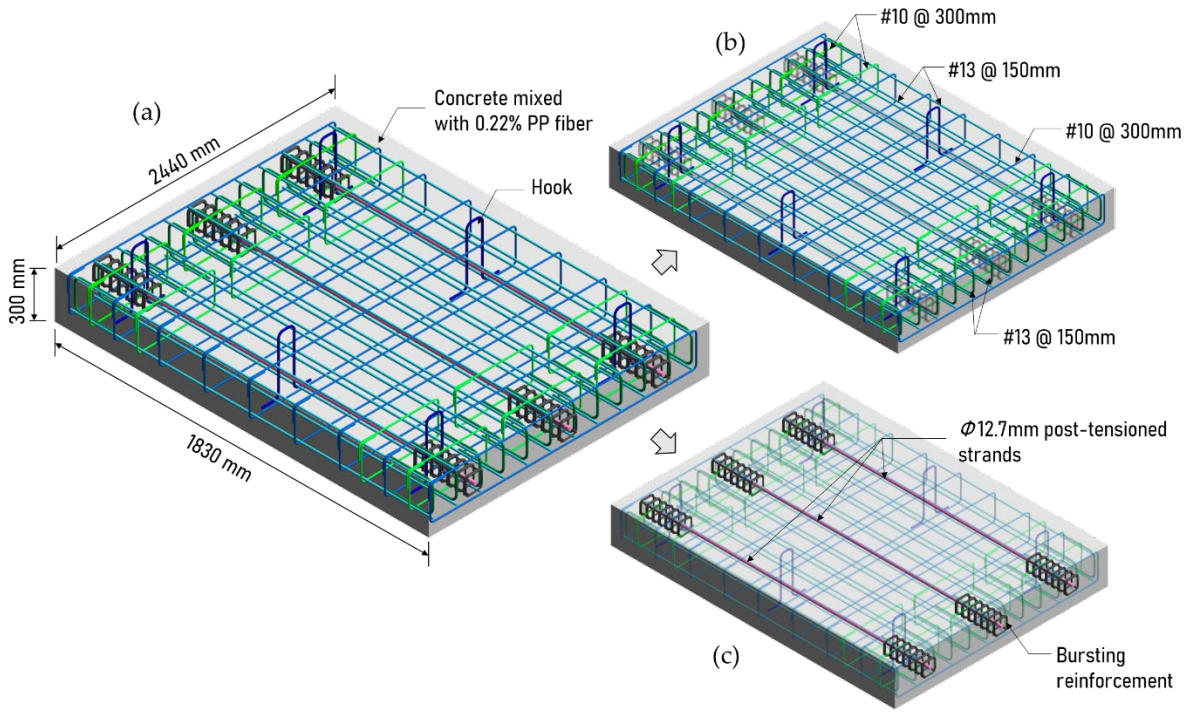

Figure 5.2 (a) Dimension, (b) reinforcement, and (c) unbonded prestressing details of TS 2

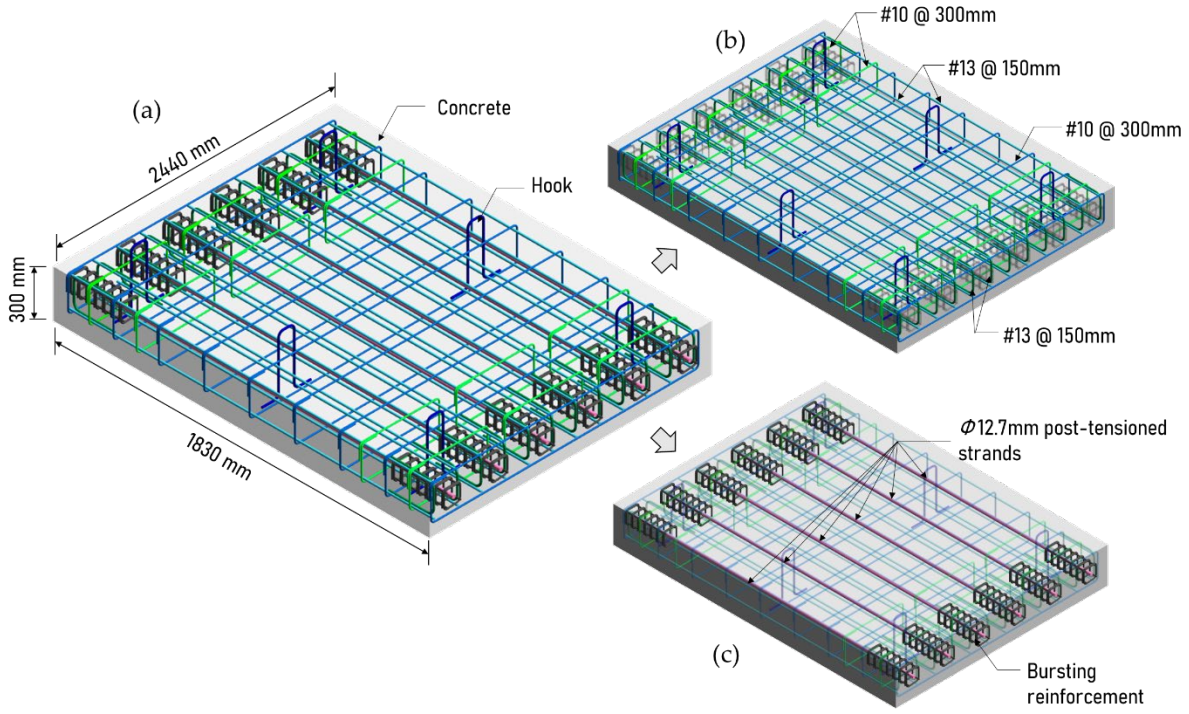

Figure 5.3 (a) Dimension, (b) reinforcement, and (c) unbonded prestressing details of TS 4

(ii) Specimen design

- Dimension and reinforcement

The thickness of the slab specimens was determined based on a survey of 20 tunnels (including both real tunnels and published case studies) collected from the literature in the recent decade [132-150]. Figure 5.4 shows this data and that a typical range for reinforced concrete tunnel lining thickness is 200 mm to 400 mm. The longitudinal reinforcement ratio of the specimens was 0.6%, consistent with the design example of a mid-size TBM tunnel lining with an inner diameter of 5.74 m (18.83 ft), as described in [151]. The rebar layouts of TS 1-4 are shown in Figure 5.5 and Figure 5.6. All dimensions in Figure 5.5 and Figure 5.6 are in mm.

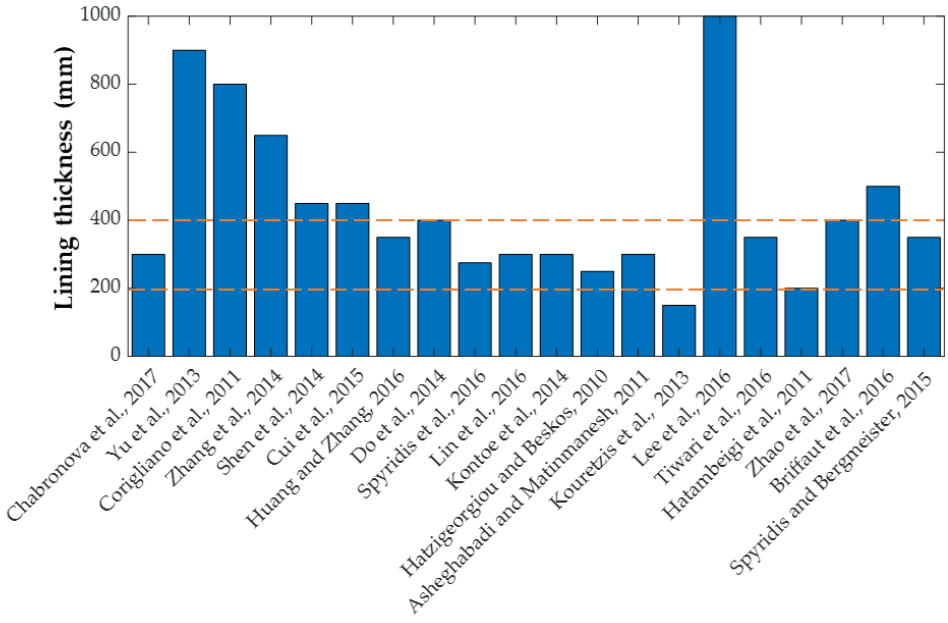

Figure 5.4 Collected data on tunnel lining thickness [132-150]

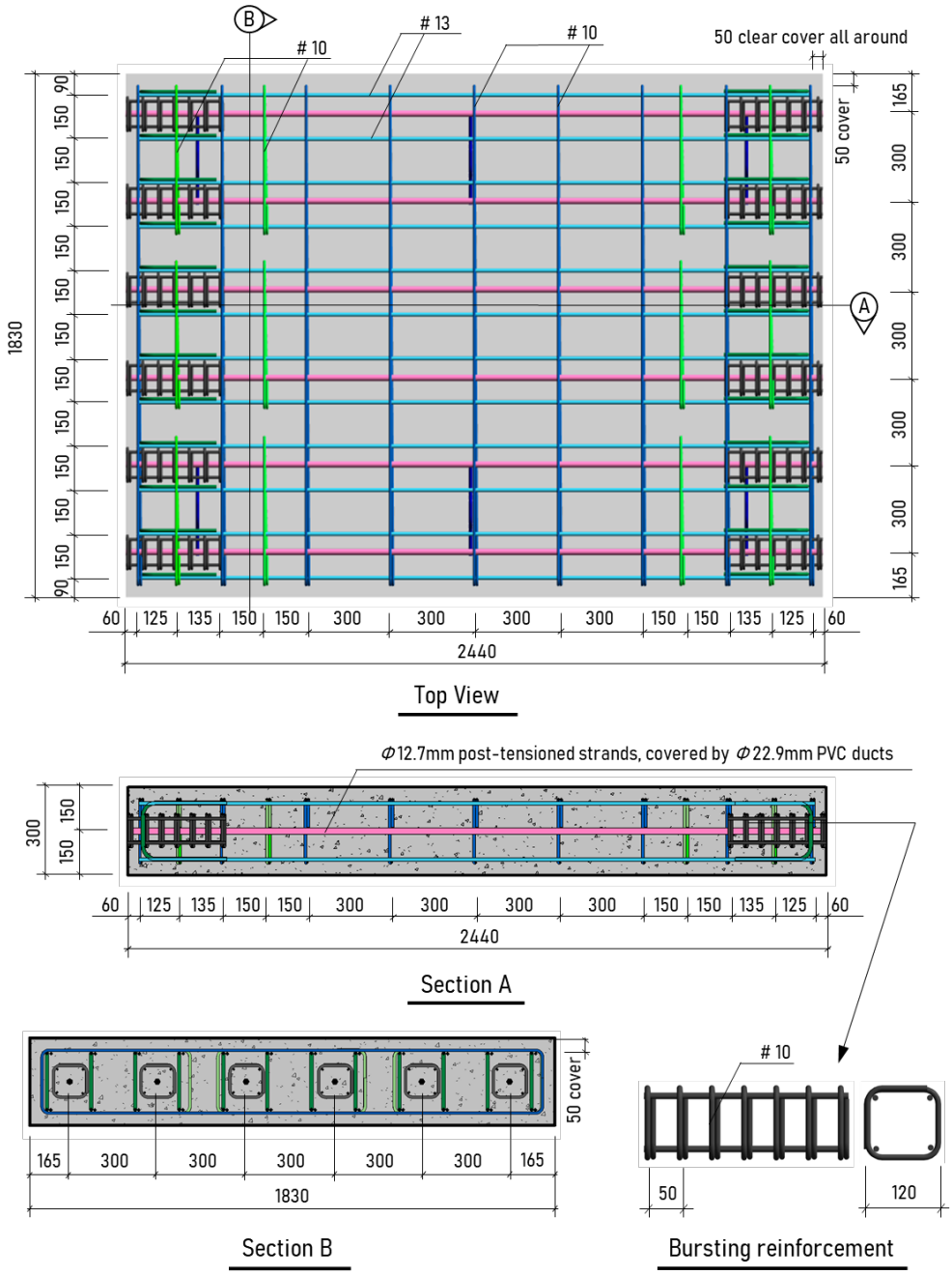

Figure 5.5 Reinforcement layout for TS 1,3 and 4

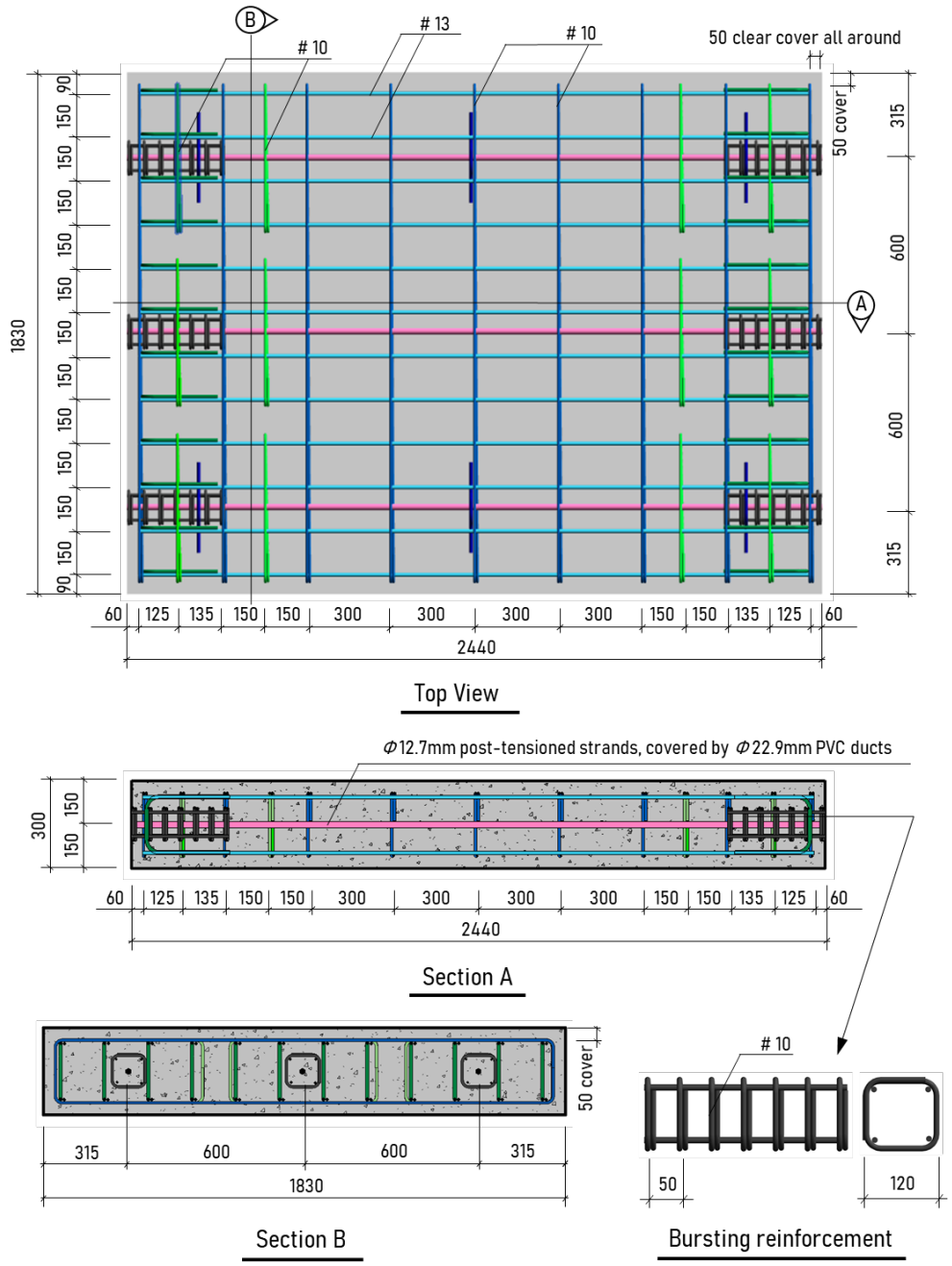

Figure 5.6 Reinforcement layout of TS 2

- PP fibers

The form, size, and dosage of PP fibers used in this test to reduce concrete spalling was determined based on a literature review. As was discussed in Chapter 3, it is widely agreed that

two major mechanisms govern the spalling process: (1) thermal stress-induced spalling, which is associated with the thermal dilation/shrinkage gradients that occur within the element when heated, and 2) pore-pressure induced spalling, which is generated by the build-up of pore pressure due to migration of water vapor toward the concrete interior at elevated temperatures. Since the permeability of concrete is one of the most important characteristics controlling moisture transport and pore pressure build-up inside concrete [122, 124, 152], the second type of spalling can be mitigated by improving the permeability of concrete at high temperatures. When heated, PP fibers melt at around 170 °C, leaving behind empty channels and creating pathways for gas [153]. In this way, the addition of PP fibers increases the permeability of concrete, which allows the outward migration of gas and results in the dissipation of pore pressure.

The PP fibers used in concrete applications are commercially available in a range of forms and sizes. The most common forms are monofilament, multifilament, and fibrillated (see Figure 5.7) [154]. It has been experimentally proven that monofilament and multifilament fibers act more effectively to reduce the propensity of heat-induced concrete spalling, due to their larger specific surface areas. Khoury [155] suggested fiber lengths of 6-12 mm as an acceptable middle region to improve the effectiveness. Bangi et al. [121] found that longer fibers of 12 mm length with diameters of 18 μm generally perform better than shorter ones of 6 mm length with diameters of 28 μm. Maluk et al. [154] further experimentally proved that longer PP fibers appeared to be more effective at reducing the propensity for spalling, as relatively short fibers could fail to generate continuous channels for enhancing gas migration during heating.

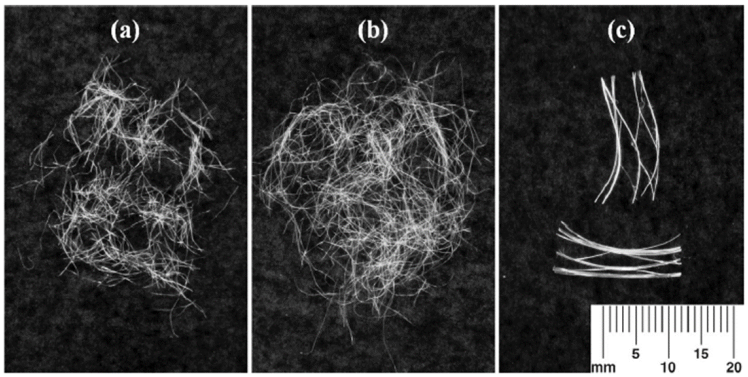

Figure 5.7 Photographs of (a) 6 mm monofilament, (b) 12 mm multifilament, and (c) 20 mm fibrillated PP fibers [154]

European guidance for the design of concrete structures under fire [156] recommends including at least 2 kg of monofilament PP fibers per cubic meter of concrete for concrete grades $80/95 < C \leq 90/105$. Australian design guidance for concrete in fire [157] states that the addition of 1.2 kg of 6 mm long monofilament PP fibers per cubic meter of concrete has a "dramatic effect in reducing the level of spalling". However, there is no established procedure for determining an optimum PP fiber dosage, i.e., the most effective PP fiber dosage for a given combination of concrete strength, permeability, aggregate sizes, heating conditions, etc. To obtain a typical PP fiber dosage, the authors searched over the proceedings of the 6th (the most-recent) International Workshop on Concrete Spalling due to Fire Exposure [21] and summarized the adopted dosages in the published experiments, as listed in Table 5.2. The experiments in Table 5.2 include normal-strength, high-strength, and ultra-high strength concrete. A PP fiber dosage of 2 kg/m^3 or 0.22% by volume appears to be an average value among these tests. Based on the above observations, the concrete mix for TS 1-3 includes 12.7 mm- and 19.1 mm-long monofilament polypropylene fibers (SikaFiber PPM-150), with a dosage of 2 kg/m^3 (0.22% by volume).

Table 5.2 Published experimental designs in the proceedings of the 6th International Workshop on Concrete Spalling due to Fire Exposure

Ref No.	Type	Concrete grade (measured compressive strength)	Fiber			
			Type	Dosage (kg/m^3)	Dosage (by vol)	Length
[17]	column	C45, C65, C85, C105	PP	3, 6	0.33%, 0.67%	12 mm
	tunnel panel	Unknown	polyvinyl alcohol/ PP	3	0.33%	Unknown
[18]	full-scale tunnel segment	C30/37, C80/95, C45/55	PP	2	0.22%	Unknown
[158]	ring-restrained specimen	(90-100 MPa)	PP / jute	0.9	0.10%	12 mm
[159]	prisms	(80-200 MPa)	PP	3	0.33%	15 mm
[20]	tunnel segment	(80-100 MPa)	PP	1.5, 1.75	0.17%	Unknown
[160]	prisms, cylinder	(120 MPa)	PP	0.9-1.35	0.1-0.15%	16 mm
[161]	slab	(40-50 MPa)	PP	2	0.22%	Unknown
[162]	cylinder	Unknown	PP	2	0.22%	Unknown

[163]	prismatic sample	(90 MPa)	PP	0.2-1.0	0.02%-0.11%	12 mm
[11]	prismatic sample	(40, 80, and 90 MPa)	PP	0.5-1.0	0.06%-0.11%	6, 12 mm

- Restraint level

Practically, tunnel linings are subjected to combined vertical and horizontal ground pressures. As a result, the ceiling slab of a tunnel lining is usually under a compressive load (see Figure 5.8 adapted from [128]). The magnitude of this compressive load could vary with tunnel shape, dimension, ground condition, etc. When exposed to fire, the compressive load would increase because the ceiling element would tend to expand but is restrained by the rest of the structure. This study used uniformly distributed, centric and straight unbonded post-tensioned strands to provide the compressive load on the slabs during the fire tests. To investigate a realistic measure of the axial constraint and to determine the number of prestressing strands for the slab tests, ambient structural analysis of a horseshoe and a rectangular tunnel have been completed using SAFIR. Note that in reality, the tunnel ceiling could also be subjected to rotational restraint, however the scope of this experimental study is limited to the effect of axial compression.

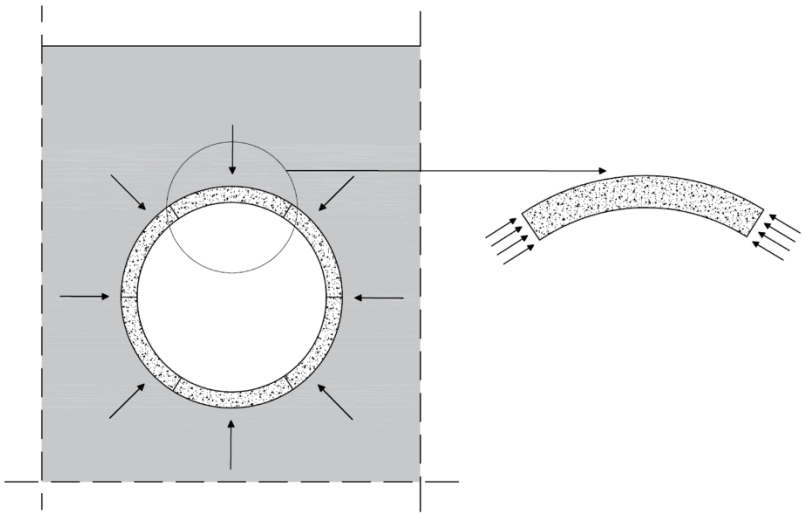

Figure 5.8 Principle of representing compressive ring forces by prestressing (adapted from [128])

Ceiling segments of tunnels with horseshoe or circular cross-sections are subjected to relatively higher levels of axial forces due to their arch shapes when compared to rectangular

tunnel sections. The first considered case study is a 2D model of the Howard Street Tunnel in Baltimore, MD, as introduced in Chapter 2. The schematic of the tunnel cross-section and its surrounding soil data are presented in Figure 5.9 (a), and the structural model is presented in Figure 5.9 (b). The tunnel lining was modeled using 26 beam elements with reinforced concrete sections. The width of the modeled lining strip was 1.83 m, thus keeping it consistent with the test specimens. The compressive strength of concrete was set to be 45 MPa and the tensile yield strength of the reinforcement was 414 MPa. Self-weight, earth pressures (vertical and horizontal) and surcharge loads were considered in the model. Soil-liner interactions were captured using 25 compression-only springs. The spring stiffness was calculated based on Eq. 4.1 [25].

$$k_s = \frac{E}{1+\nu} \cdot \frac{1}{R} \tag{4.1}$$

The axial force on the ceiling element (see Figure 5.9 (b)) under the aforementioned service loads was calculated as 656 kN.

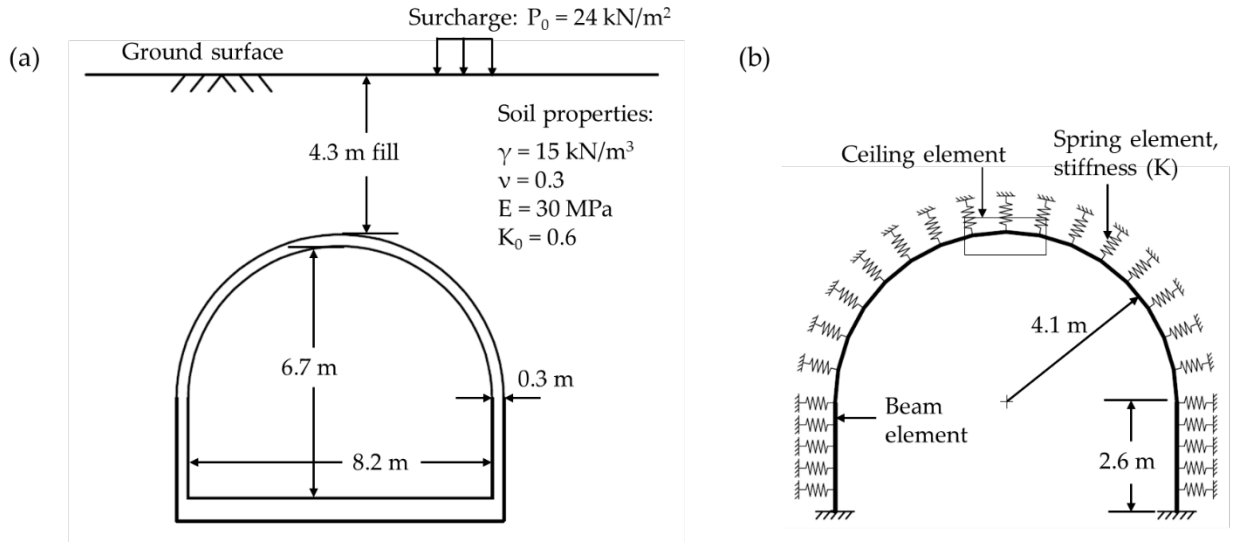

Figure 5.9 (a) Schematic and (b) structural model of a horseshoe tunnel

A parallel study on a 2D rectangular tunnel model is also conducted using SAFIR, following the same methodology as above. The tunnel model is shown in Figure 5.10, located at 4.3m below ground surface (same as the horseshoe tunnel). The geometry of the considered rectangular tunnel cross-section was obtained from the Harbor Tunnel in Baltimore, MD [164]. The axial force on the ceiling element (Figure 5.10) under service loads was calculated as 375 kN.

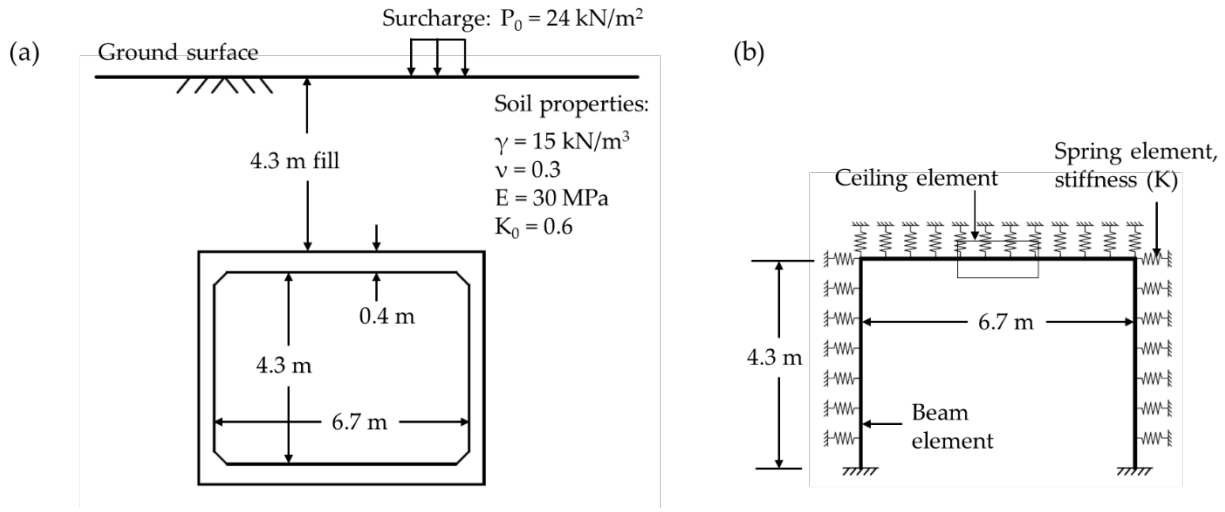

Figure 5.10 (a) Schematic and (b) structural model of a rectangular tunnel

Based on the results, two levels of prestress are considered for the purpose of experiments: (1) six ϕ12.7mm prestressed strands with initial prestress of 1172 MPa (170 ksi), translating into a total force of 694 kN (156 kips), and (2) three ϕ12.7mm strands with initial prestress of 1172 MPa, translating into a total force of 347 kN (78 kips). As Figure 5.5 and Figure 5.6 show, the straight prestressing strands are uniformly distributed along the center line of the specimens to provide axial restraints. When being heated, the concrete would want to expand while the strands provide restraint and increase compressive forces within the concrete slab.

(iii) Specimen construction

Figure 5.11 shows the construction process including steel cage assembling and concrete pouring. The concrete slabs were cured with water sprays and canvas covers for one month at room temperature. Figure 5.12 shows the cylinder samples of concrete mixed with PP fiber and plain concrete, which were cured in water for one month.

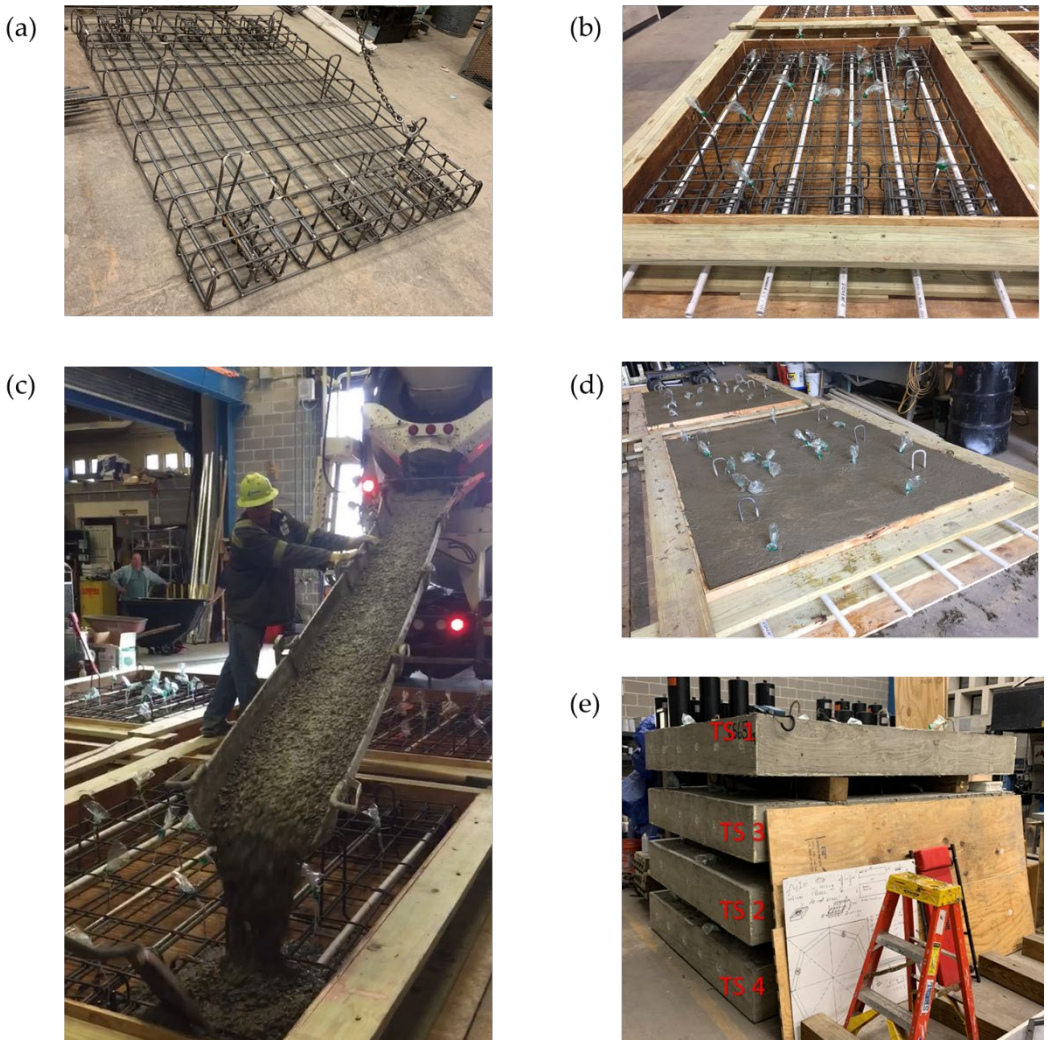

Figure 5.11 (a) Steel cage, (b) before concrete pouring, (c) during the concrete pour, (d) finished surface after the concrete pour, and (e) piled specimens at ambient temperature following the curing process

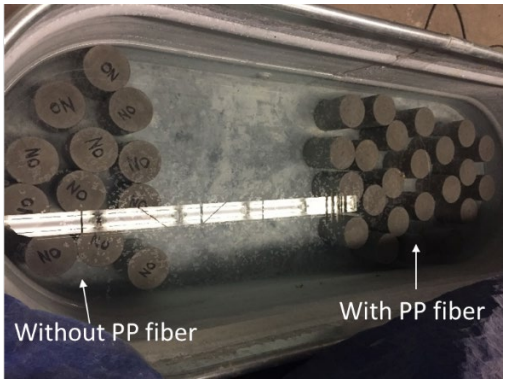

Figure 5.12 Concrete cylinder samples during the curing process

5.2.2 Test set-up

Static loading is applied on the concrete slab using a 500 kN-capacity hydraulic actuator with 250mm stroke. The actuator is mounted to a steel loading frame positioned around the furnace. A spreader beam is used to distribute the load on the slab through two rollers. The test specimens are supported by two steel frames. The supports are specially designed for the purpose of these tests to take the load from the specimens and protect the furnace body from mechanical loading. High-temperature fiber blankets are used to seal gaps between the specimen and the furnace, insulate the steel supports, and to prevent heat escaping from the fire chamber. A steel wire mesh is attached to the specimen to protect the furnace electric coils from potential concrete spalling. The test set-up is shown in Figure 5.13 and Figure 5.14.

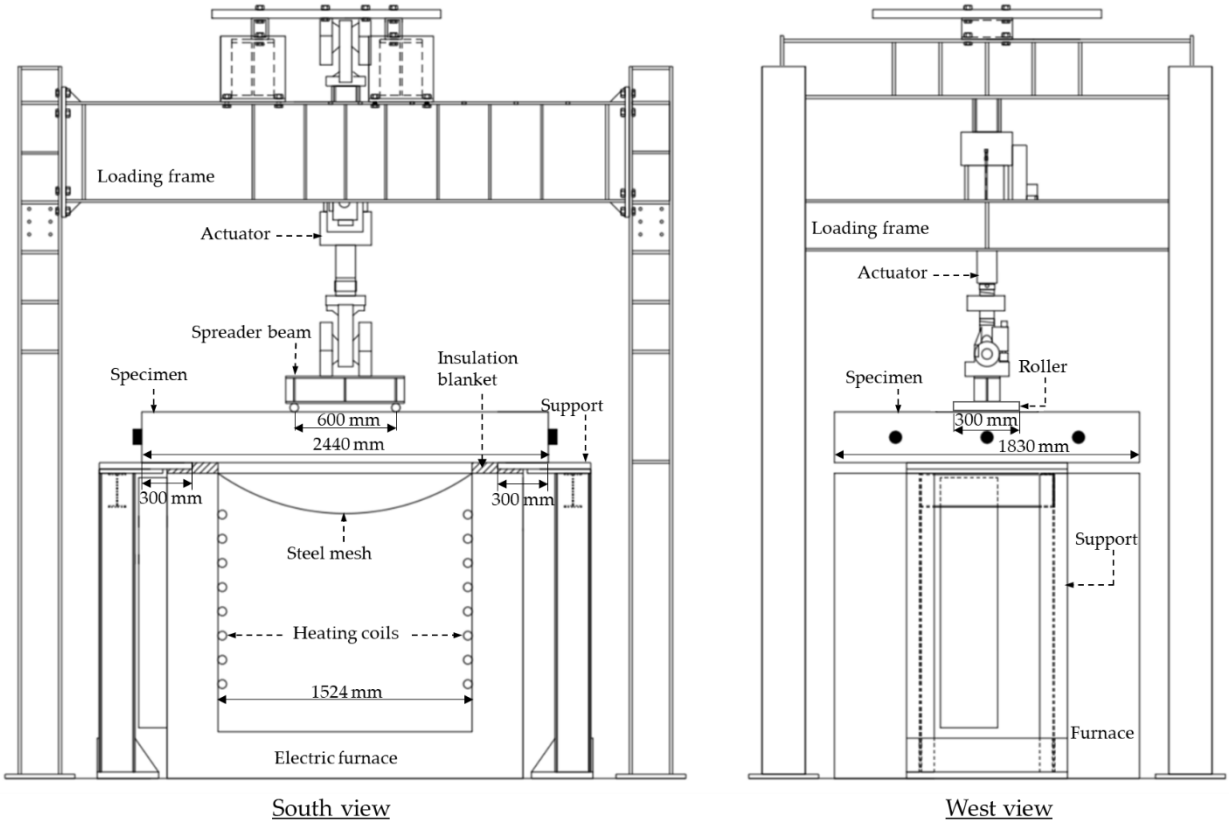

Figure 5.13 Test set-up

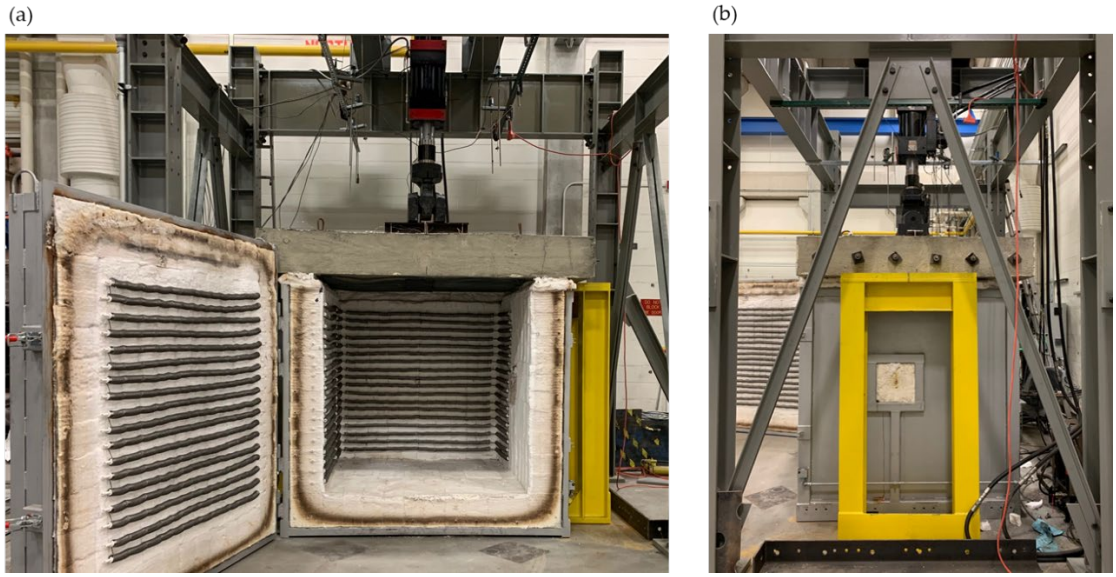

Figure 5.14 (a) South view and (b) East view of the test set-up (with furnace door opened)

The slab specimens are heated using an electric furnace with a fast ramp (Figure 5.15). The furnace is capable of reaching temperatures up to 1000 °C, with input ramp and soak protocols specified through a control panel. The furnace is made of a steel shell lined with high temperature fiber insulation, and heated by heating elements (metal coils). The lid is removed in this experiment to accommodate the test specimens during tests. The fire chamber is 1530 mm x 1530 mm x 1530 mm (5′ x 5′ x 5′).

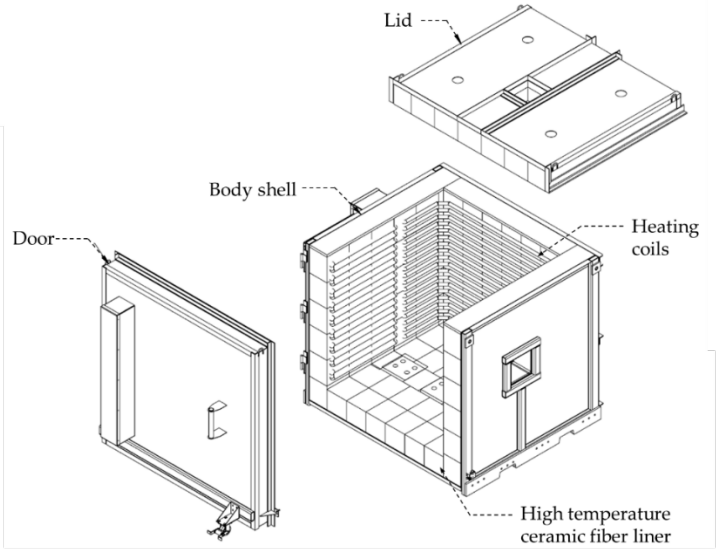

Figure 5.15 Schematic of the furnace

5.2.3 Instrumentation and data acquisition

The following types of sensors are used to measure furnace temperature, concrete and rebar temperatures, displacements, and external forces during the test.

(i) Furnace thermocouples

Type 'K' thermocouples (Figure 5.16) are mounted through the side wall of the furnace to measure and control the gas temperature inside the furnace. As Figure 5.17 shows, multiple thermocouples were used for redundancy.

Figure 5.16 Photograph of a type 'K' furnace thermocouple

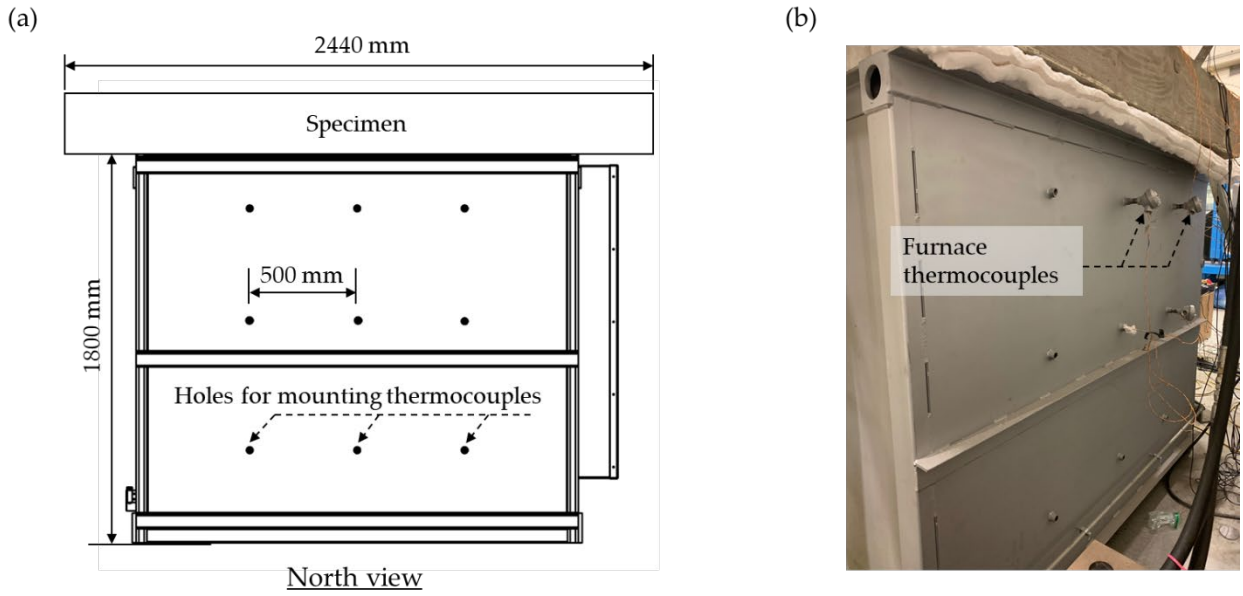

Figure 5.17 Location of furnace thermocouples: (a) schematic drawing and (b) photograph

(ii) Concrete and rebar thermocouples

Concrete and rebar temperatures are measured using Omega type 'K' bare wire thermocouples (maximum temperature measurement: 870 °C). While the tails are covered with heat shrink tubes for insulation, only the small "V" shape tips of the thermocouples are kept bare to ensure accurate measurements, as Figure 5.18 shows.

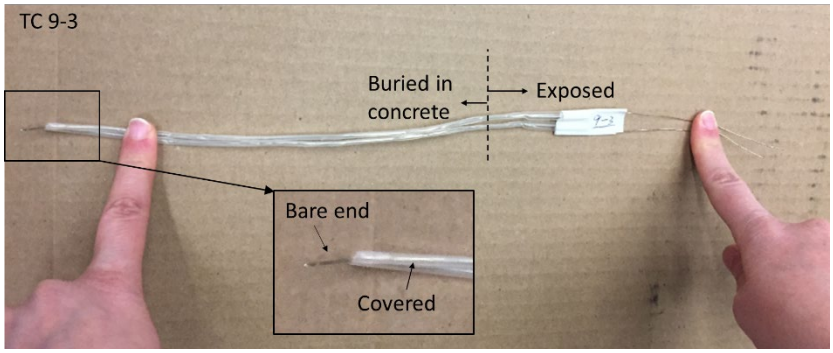

Figure 5.18 Concrete and rebar thermocouples

To measure the temperature within the specimen, 28 thermocouples are buried in each slab to obtain concrete temperature at different locations and depths. As Figure 5.19 shows, there are 15 locations across the slab, each location accommodates one or two thermocouples installed at different depths. Locations No. 1 through 9 are within the heating boundary, while the other locations are not directly heated. The information for all the thermocouples for a sample slab is summarized in Table 5.3. More thermocouples have been placed close to the heated surface of concrete (25 mm, 50 mm and 75 mm depth) to capture the large temperature gradient in that area. The implemented plan for the thermocouple locations is aligned with the requirement in the ENFARC guideline [129].

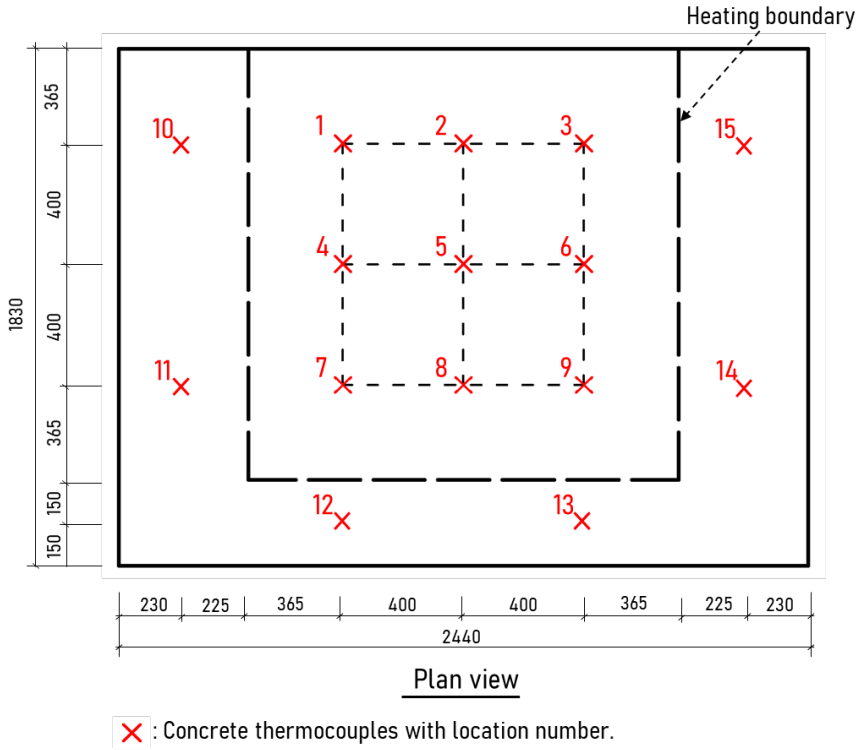

Figure 5.19 Locations of concrete thermocouples

Table 5.3 Summary of concrete thermocouples per slab

No. of thermocouple	No. of location	Depth (mm)	No. of thermocouple	No. of location	Depth (mm)
TC 1-1	1	25	TC 8-6	8	150
TC 1-3	1	75	TC 9-1	9	25
TC 2-2	2	50	TC 9-3	9	75
TC 2-6	2	150	TC 10-1	10	25
TC 3-1	3	25	TC 10-3	10	75
TC 3-4	3	100	TC 11-2	11	50
TC 4-2	4	50	TC 12-1	12	25
TC 5-1	5	25	TC 12-3	12	75
TC 5-3	5	75	TC 13-2	13	50
TC 6-2	6	50	TC 13-4	13	100
TC 7-1	7	25	TC 14-1	14	25
TC 7-4	7	100	TC 14-3	14	75
TC 8-2	8	50	TC 15-2	15	50

Note: Depth (mm) is calculated from the heated surface of the specimen.

Six thermocouples are used to measure temperature of the reinforcement during the test. As Figure 5.20 shows, four thermocouples are mounted on the bottom reinforcement and two thermocouples are mounted on the top reinforcement.

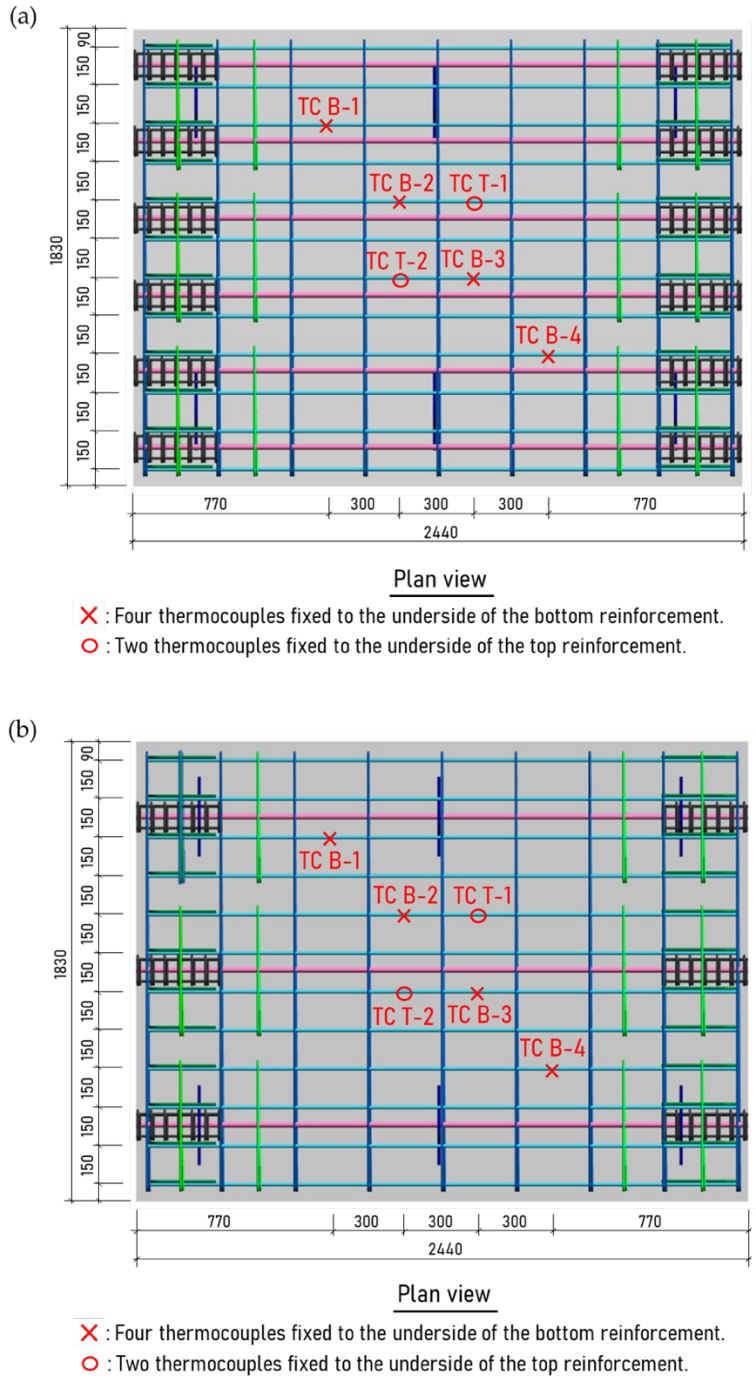

Figure 5.20 Reinforcement thermocouples for (a) TS 1, 3, 4, and (b) TS 2

(iii) Displacement transducers

The LVDT (Linear Variable Differential Transformer) transducer mounted within the actuator is used for measuring slab center displacements. Two additional string potentiometers are used to monitor the movement of the two steel supports during tests. They are illustrated in Figure 5.21.

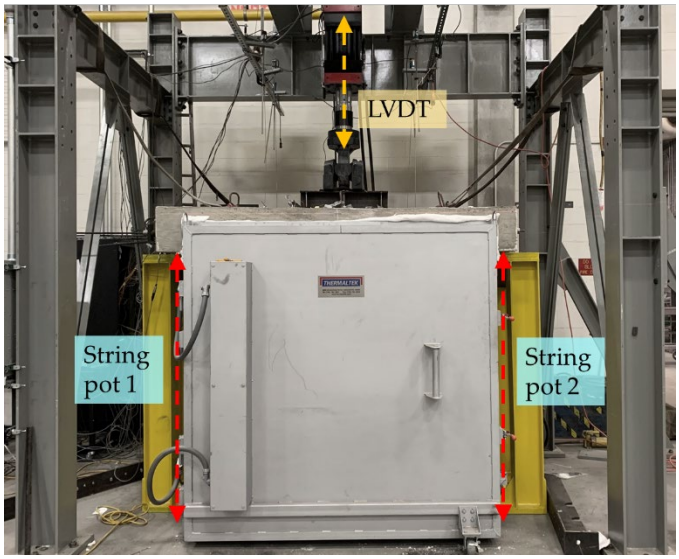

Figure 5.21 Displacement transducers

Experimental data are collected using the Pacific Instruments 6000 Mainframe Data Acquisition System. The sampling rate was 10 samples per second.

5.3 Test program

The test program includes two main stages: static loading, and fire test. In addition, a series of rebound hammer tests are conducted before and after each furnace test to obtain the strength profile of the undamaged and damaged bottom surface of each specimen. The locations of hammer tests on the specimens are shown in Figure 5.22. According to [36], 10 tests are conducted on each 200 mm-diameter circular area to obtain an average strength.

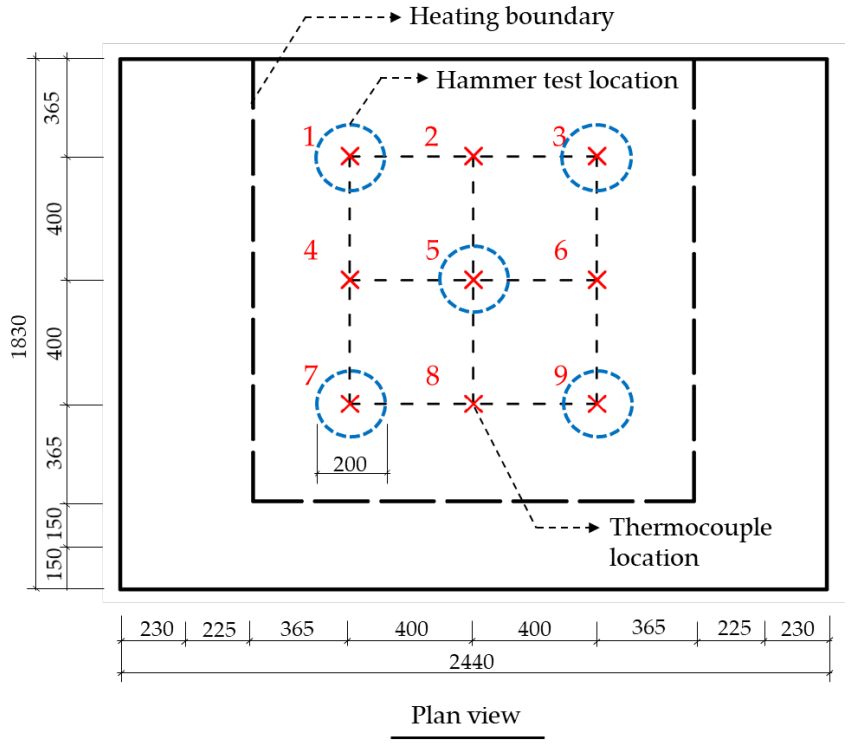

Figure 5.22 Plan view of areas where the hammer test is conducted

5.3.2 Static loading

As a first step, the force-controlled static loading is applied to the specimen with an average velocity of 3 kN per second. The load is distributed to two line loads through a spreader beam supported by two steel rollers, as shown in Figure 5.23. The applied load is 310 kN (70 kips) for all four specimens, which is equivalent to the weight of 3-meter soil overburden plus a surcharge load of 14 kPa. After reaching 310 kN, the applied load is kept constant for 4-6 hours after the fire test.

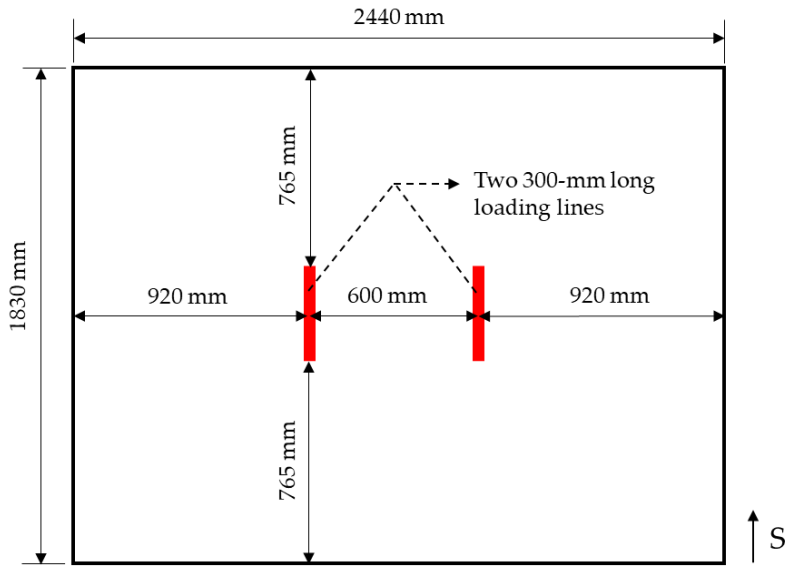

Figure 5.23 Plan view of the top surface of a slab specimen and the loading lines

5.3.3 Fire test

For each test, the heating phase starts following the application of the static load. A square area of 1530 mm x 1530 mm (5 ft x 5 ft) of the bottom surface of the specimen is exposed to heat (see Figure 5.24). The designed temperature-time curves for the heating phase are presented in Figure 5.25 (solid lines). Only TS 3 is tested under "scenario 2", the rest of the specimens are tested under "scenario 1". Based on the results from FDS analysis introduced in Chapter 2, the temperature heating rate, the maximum temperature and its duration for "scenario 1" can be taken as a representative scenario of a high-intensity passenger train fire, while "scenario 2" (without a temperature plateau) represents the effect of fixed firefighting safety system getting activated and suppressing the fire.

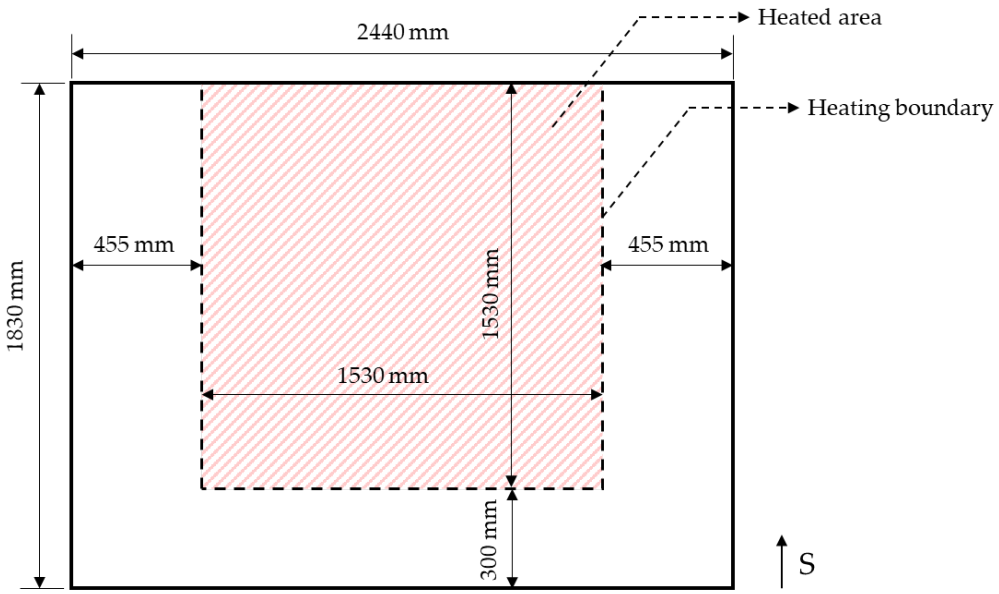

Figure 5.24 Plan view of the bottom surface of a slab specimen with specified heated area

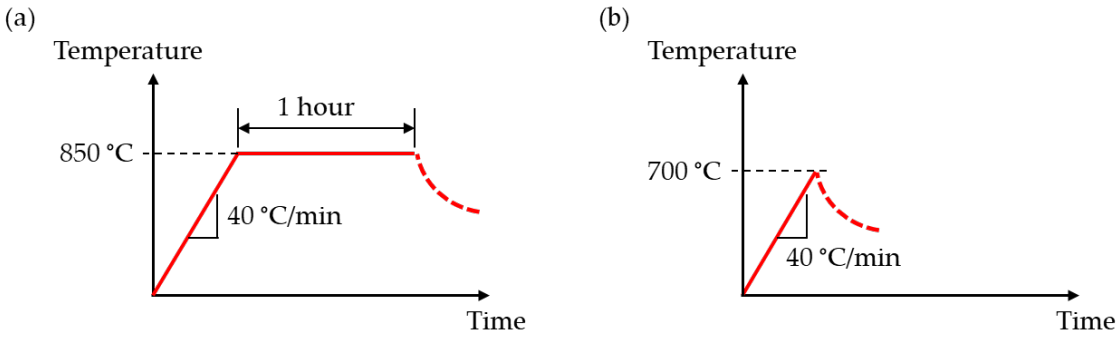

Figure 5.25 Temperature-time protocols: (a) scenario 1 and (b) scenario 2

The furnace would then be turned off after the designed heating curve is achieved. The furnace and the specimens would be naturally cooled down to ambient temperatures. All the instruments would stay connected until the concrete specimen is completely cooled down, for capturing responses during the cooling phase and residual deflections.

5.4 Test matrix

Table 5.4 provides a summary of the test matrix for the large-scale slab tests, where the concrete strengths and moisture contents are measured using the cylinder samples (average of three samples).

Table 5.4 Test matrix for large-scale specimens

Test No.	Specimen No.	Mixed with PP fiber or not	No. of post-tensioned strands	Measured concrete strength (f'_c)	Measured moisture content	Heating curve
Test 1	TS 1	YES	6	9.6 ksi	2.5%	Scenario 1
Test 2	TS 2	YES	3	9.6 ksi	2.5%	Scenario 1
Test 3	TS 3	YES	6	9.6 ksi	2.5%	Scenario 2
Test 4	TS 4	NO	6	10.6 ksi	2.5%	Scenario 1

5.5 Results

5.5.1 Measured furnace temperature

The measured furnace temperature-time curves during the four tests are shown in Figure 5.26. The fire curves represent the average temperatures from multiple thermocouples at various locations within the furnace chamber. Overall, the recorded furnace temperatures follow the designed curves with slight differences at peak temperatures. Test 4 experienced a heating delay at around 15 minutes due to short circuiting in the electric system (most likely caused by spalling of concrete within the furnace at the time). Following each fire test, the furnace door was opened when the chamber temperature was cooled down to approximately 300 °C to shorten the cooling period; a quick temperature drop can be observed, as shown in the figure, accordingly. The furnace temperatures cooled down to ambient within 12 hours for all the tests, while this process took longer for Tests 1 and 4 compared to Tests 2 and 3.

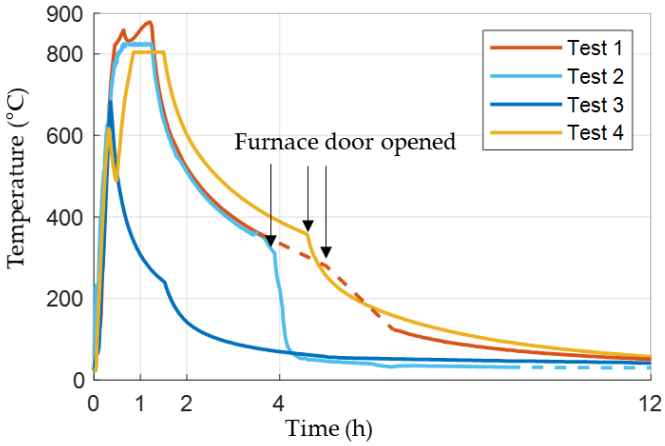

Figure 5.26 Furnace temperature-time curves for all four tests

5.5.2 Concrete temperatures

Temperatures within the heated area of each slab, measured at 25 mm, 50 mm, 75 mm, and 150 mm from the heated surfaces, are recorded for 24 hours and presented in Figure 5.27. Each curve represents the average of all the thermocouple readings at a given depth (locations 1 to 9 in Figure 5.19). The differences between the temperatures measured at the same depth are within 20%, where the slab center typically experienced slightly higher temperatures compared with the concrete close to heating boundaries. As for the unheated areas (locations 10-15 in Figure 5.19), concrete temperatures stayed below 150 °C during all the four tests.

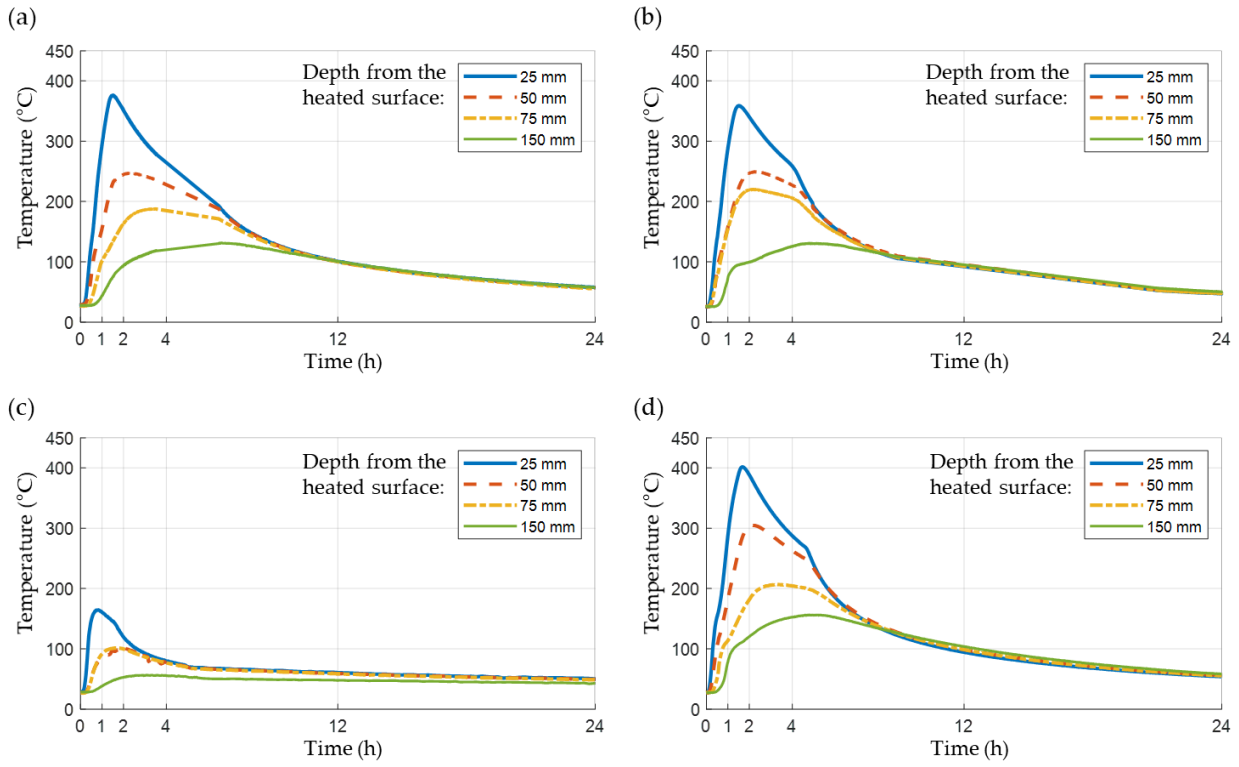

Figure 5.27 Concrete temperature measurements for (a) TS 1, (b) TS 2, (c) TS 3, and (d) TS 4

As shown in Figure 5.27, although the furnace temperatures were similar for Test 1, 3 and 4, specimen TS 4 experienced the highest sectional temperatures (e.g. concrete at 25 mm reached 400 °C) due to concrete spalling. When spalling occurred, the heating boundary propagated and caused higher temperatures within the inner concrete section. The spalling process was gradual, based on the relatively continuous "popping sounds" heard during Test 4, and also no abrupt increase in concrete temperature was recorded. TS 1 experienced slightly higher sectional temperatures than TS 2 and took the longest time to cool down. TS 3 had the lowest concrete temperatures (remained below 200 °C) as the slab was subjected to a fast heating curve. The sections of all the slabs cooled down to around 50 °C after 24 hours. Based on the damage assessment methodology introduced in Chapter 3, where 300°C was used as a threshold for concrete damage, Table 5.5 summarizes the damaged depths of the four specimens.

Table 5.5 Damaged depths of the slabs

Specimen No.	TS 1	TS 2	TS 3	TS 4
Damaged depth	25 mm	25 mm	<5 mm	50 mm

5.5.3 Rebar temperatures

Figure 5.28 shows the temperature evolutions of the top and bottom reinforcements for the four tests. Similar to concrete temperature readings, the reinforcement in TS 4 underwent the highest temperatures because of spalling, whereas TS 4 had the lowest rebar temperatures. It is worth mentioning that the bottom rebar temperatures are consistent with the concrete temperatures at 50 mm depth from the heated surfaces, where the bottom rebars were located. The temperatures of rebars remained below 300 °C for all the tests.

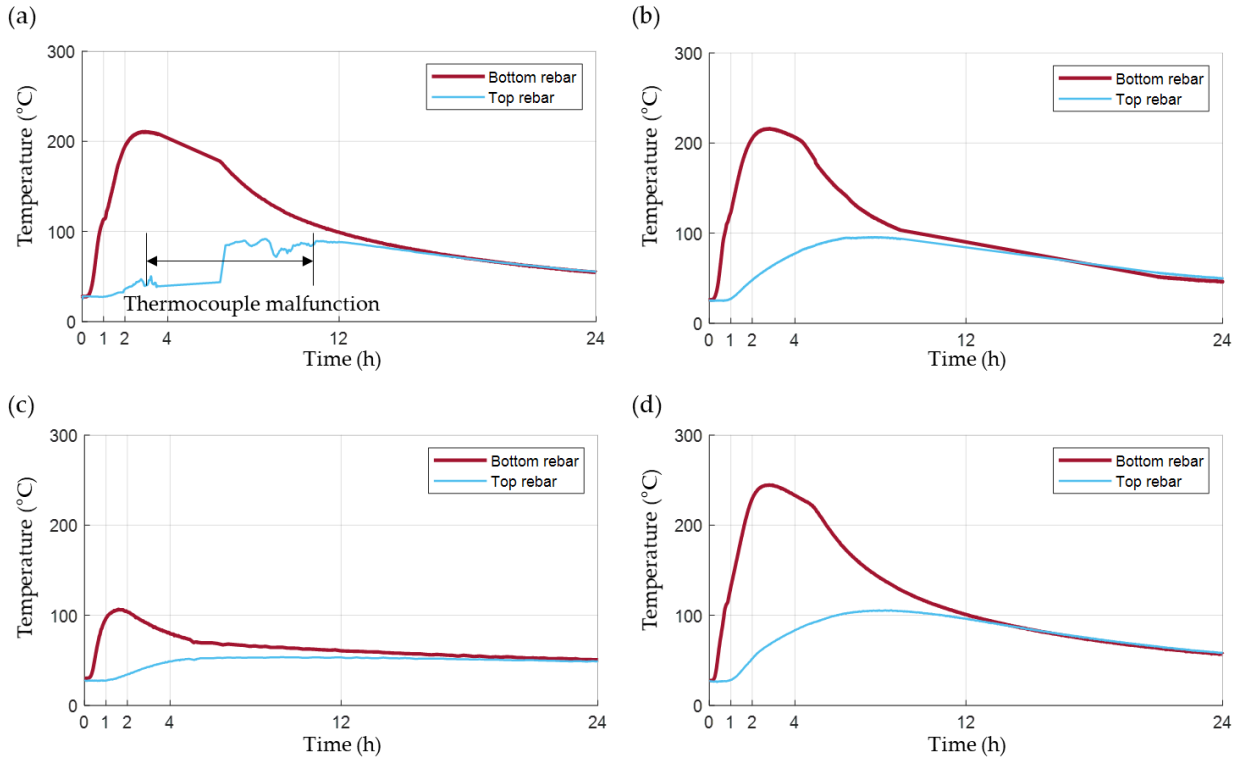

Figure 5.28 Rebar temperatures for (a) TS 1, (b) TS 2, (c) TS 3, and (d) TS 4

5.5.4 Center displacement of slabs

Figure 5.29 compares the vertical displacements of the center of the slabs during and after the fire tests. The graph shows that, at time zero, all the slabs had similar initial central displacements (2-3 mm) under a 310-kN vertical static load. The slabs show a similar and distinct

three-stage deflection trend, with a rapid deflection rate during the initial heating, followed by a steady state phase where the deflections did not change significantly, and finally a slow recovery during cooling. The static load applied by the actuator was removed at about 4 to 6 hours after the fire tests had started (the actuator and laboratory hydraulics had to be turned off after laboratory working hours). The four slabs had similar deflection rates at the early stage of the fire because of the similar heating ramps. After 24 hours, when the sections cooled down to almost ambient temperature, the central displacements were steady and did not show any change. The Residual displacements of several millimeters were recorded (a minimum of 3 mm in Test 3 and a maximum of 7 mm for Test 1). Note that the application of the static load did not cause any nonlinear behavior; hence, the residual displacements were mainly from the fire effect.

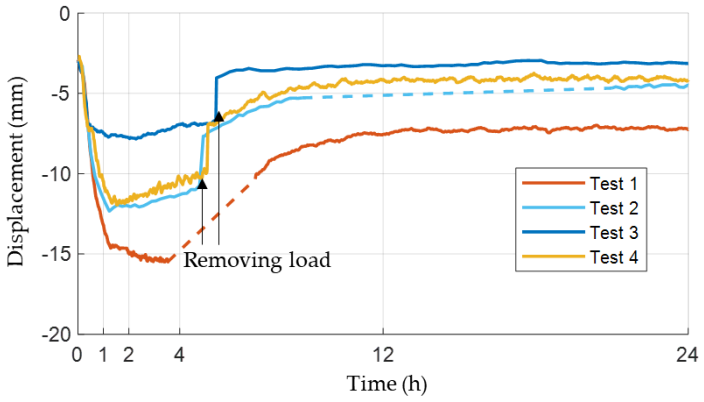

Figure 5.29 Displacements at the center of slabs for all tests

The maximum and residual deflections of the four slabs are summarized in Table 5.6. TS 1-3 included PP fibers in the concrete mix, among which TS 1 reached the largest maximum and residual center displacement, which can be explained by the slightly higher temperatures and a longer cooling process during Test 1. TS 4 had the highest concrete strength (the mix without PP fibers) and was subjected to the maximum fire temperature of 800 °C (compared to 850 °C in other tests). However, given the damage due to spalling and penetration of heat within the concrete section, TS 4 experienced similar displacements as TS2. The restraint condition did not make distinct influence on the displacement results.

Table 5.6 Maximum and residual deflections for the four tested slabs

Specimen No.	TS 1	TS 2	TS 3	TS 4
Maximum deflection	15 mm	12 mm	8 mm	12 mm
Residual deflection	7 mm	5 mm	3 mm	4 mm

5.5.5 Post-fire damage

(i) Concrete spalling and cracking on the heated surface

Figure 5.30 shows the heated surfaces of the four slabs after the fire tests. Only TS 4 experienced heat-induced concrete spalling, while a large number of distributed cracks were observed on the heat-exposed surfaces of TS 1-3. The major cracks (> 0.2 mm) were traced with thick black lines and the minor cracks (≤ 0.2 mm) were traced with thin red lines in Figure 5.30. The threshold of 0.2 mm was selected according to the maximum allowable crack thickness of reinforced concrete structural members prescribed by a series of international guidelines [165]. The maximum measured crack widths were 0.50 mm, 0.55 mm, and 0.30 mm for TS 1,2 and 3, respectively. TS 3 (Figure 5.30c) had a minimal number of major cracks as a result of the short heating protocol. The major cracks can cause future serviceability concerns such as corrosion, and it is recommended to be repaired after fire.

TS 4 (without polypropylene fibers) experienced spalling, most of which occurred towards the perimeter of the heated area, with the north-west corner (the top left corner in Figure 5.30d) experiencing the most severe spalling, where the bottom reinforcement was exposed. The maximum and average spalling depths were 83 mm and 25 mm, respectively. The weight of spalled concrete sections was 23.4 kg. In summary, the combining effects of adding PP fibers and the activation of a fixed fire-fighting system (replicated by a quick fire in the test) would minimize fire damage to the concrete liner surface.

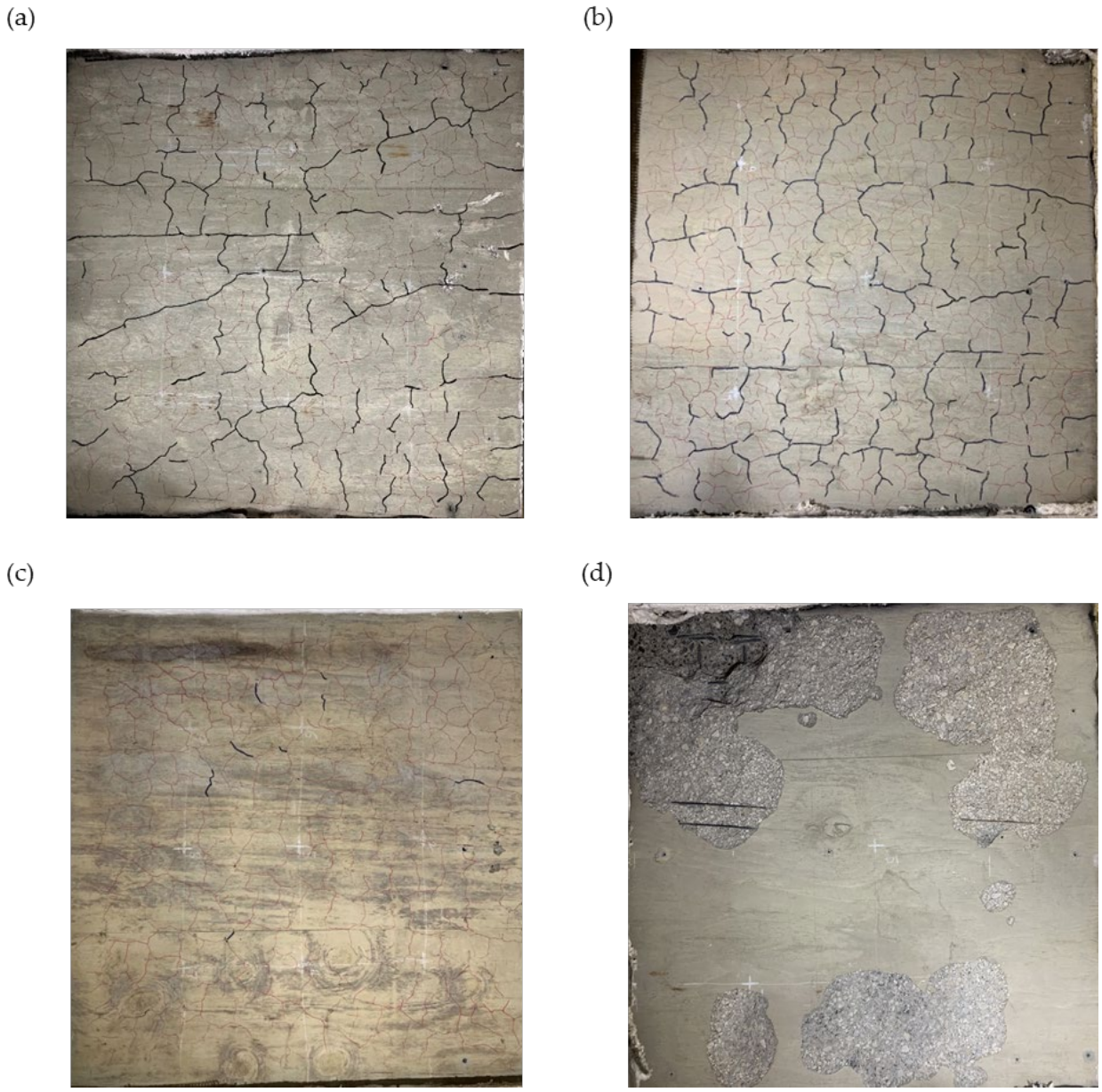

Figure 5.30 Heated surfaces of (a) TS1, (b) TS 2, (c) TS 3, and (d) TS 4 after fire tests, showing cracked and spalled concrete

(ii) Strength deterioration

The Schmidt Hammer test, a non-destructive testing technique, was conducted to measure the strength profile across the bottom slab surfaces of the slabs before and after fire and to assess the average strength deterioration after the fire. Figure 5.31 shows the changes (in percentage) between the measured concrete strength before and after the fire tests. The presented

result for each test location (as marked in Figure 5.22) is the mean value of 10 hammer test readings at that location. Table 5.7 summarizes the average change in concrete strength across the slab surface considering all the test locations from Figure 5.31. The results from the Schmidt Hammer test shows that the heated surfaces of TS 1, 2, and 4 experienced around 20% strength loss after an 80-min fire, whereas TS 3 gained 4% in concrete strength. The gain in concrete strength is consistent with other material-level tests, where heating of concrete up to 200 °C could lead to an increase in strength due to cement hydration [166].

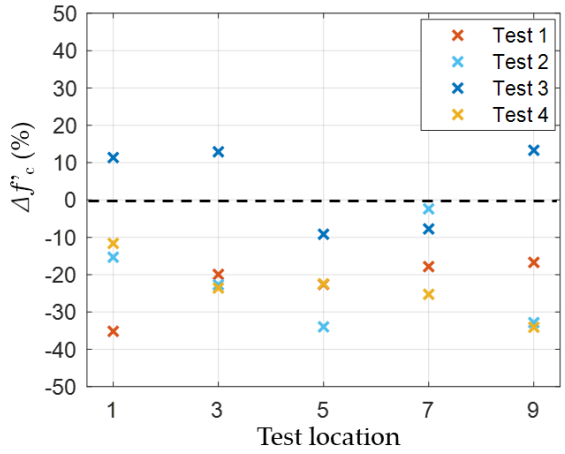

Figure 5.31 Change in f'_c measured by the Schmidt Hammer tests

Table 5.7 Average change in the concrete strength of slab surfaces after the fire tests

Specimen No.	TS 1	TS 2	TS 3	TS 4
Average $\Delta f'_c$ (%)	-22%	-21%	+4%	-23%

5.6 Conclusions

This chapter summarized the design, preparation, execution, and results of fire experiments of four loaded and restrained reinforced concrete slabs. Each slab was 2440 mm x 1830 mm x 300 mm (8′ x 6′ x 1′). The thickness and reinforcement ratio of the slabs were selected following the design of modern tunnel concrete linings. The slabs were heated at the soffit (one sided heating) using a furnace with a fire chamber of 1530 mm x 1530 mm x 1530 mm (5′ x 5′ x 5′). Three of the slabs included polypropylene fibers (SikaFiber PPM-150), and one slab used a

conventional concrete mix. The cylinder tests showed a concrete strength of 9.6 ksi for the mix with polypropylene fibers and 10.6 ksi for the conventional concrete mix. The slabs were post-tensioned to replicate the effect of restraint from the rest of the tunnel sections. Two levels of restraint associated with a crown section in a horseshoe tunnel and a rectangular tunnel were considered. A load of 310 kN (70 kips) were applied to the slabs, equivalent to the weight of a 3-meter soil overburden plus a surcharge load of 14 kPa. Two different fire scenarios were considered: (1) the first fire scenario reached the maximum temperature of 850 °C at a rate of 40 °C/min with the soaking time of 60 min, and (2) the second fire scenario was a quick fire reaching the maximum temperature of 700 °C without any soak time to represent the activation of a fixed firefighting system in a tunnel. The concrete and rebar temperatures and slab displacements were measured during the heating and cooling phases of the tests. Damage, in terms of cracking, spalling, and loss of concrete strength, were documented.

The overall outcomes of the four experiments demonstrated that the lack of any active or passive fire protection could lead to damage even under a moderate fire scenario (e.g., 23 kg of concrete spalling from the heated surface was recorded for an 80 min railway tunnel fire). Addition of the polypropylene fibers prevented spalling of concrete; however, the slab could experience cracking and a residual displacement that would require assessment for the long-term performance of the structure. The test with a quick fire (representing activation of fixed firefighting system in a tunnel) showed the least amount of damage, although a minimal residual displacement was still observed after the slab completely cooled down. The Schmidt hammer test showed an average strength gain of 4% in the test specimen with the quick fire, which is consistent with material-level tests in the literature when concrete heats up to 200 °C (due to additional hydration of the cement paste). The 80-min moderate fires caused an average of 20% reduction in concrete strength according to the Schmidt hammer tests of the concrete surfaces. The documented experimental results in this chapter can be used for model verification during both heating and cooling phases of the fire. The residual performance of a structure is crucial to determine the post-fire capacity and serviceability of a tunnel structure.

CHAPTER 6 CONCLUSIONS AND RECOMMENDATIONS

This report studied fire damage to tunnel lining using numerical modeling and experimental testing. Chapters 2 and 3 established a framework to quantify fire damage through modeling considering the uncertainties in the fire scenario and fire spread within the tunnel. Application of the established framework was demonstrated for a passenger railway tunnel fire. Variations in the heat release rate of railway cars, ventilation velocity, tunnel slope, and fire spread criteria within the tunnel were captured and 540 scenarios were simulated to characterize the spatial and temporal distributions of fire temperature within the affected section of the tunnel. The obtained distribution for the maximum obtained temperatures was used to make recommendations for design applications. The spatial variation in temperature across the tunnel section was taken into account when evaluating damage to the concrete liner. The volume of damaged concrete was determined based on the results of heat transfer analysis and structural analysis, both of which provided similar assessments. The structural behavior of the tunnel section under fire was modeling and the soil-concrete liner interaction was incorporated using compression-only springs in the model. The tunnel structure showed stability for extreme fire scenarios, consistent with observations in historic cases. It was shown that the main drive for the application of passive or active fire protection within a tunnel, from a structural point of view, is to minimize damage and tunnel downtime following a fire event.

Chapters 4 and 5 provided results of experimental tests of fire damage to concrete. Chapter 4 summarized results of small-scale (i.e., material level) tests conducted at the New Jersey Institute of Technology (project collaborator). The results confirmed that adding polypropylene fibers within the concrete mix prevented spalling at high temperatures. Chapter 5 summarized the experimental results of 4 loaded and restrained reinforced concrete tunnel slabs conducted at the University at Buffalo. The effects of the following parameters on the level of damage were studied: (1) fire scenario (a railway tunnel fire versus a fast fire that is suppressed by activation of a fixed firefighting system in a tunnel), (2) addition of 0.22% (by volume) polypropylene fibers to the concrete mix, and (3) level of restraint (representing a crown tunnel

slab in a horseshoe tunnel versus a rectangular tunnel). The documented data included fire temperature, concrete temperatures at different depths within the slab, rebar temperatures, and displacement of the slab. The data were recorded for 24 hours until the specimens were completely cooled down. Crack patterns and sizes, and the change in concrete strength using the Schmidt Hammer test were also reported. The results showed that the combination of both active (fixed firefighting system) and passive (polypropylene fibers) fire protection minimizes the damage within the tunnel for the considered fire scenarios, and operation can be resumed quickly. However, the lack of any mitigation strategies, such as the addition of polypropylene fibers, could lead to spalling and damage even under moderate railway tunnel fire. The amount of added polypropylene fibers were sufficient to prevent concrete spalling for the considered levels of restraint in the slabs.

The presented results in this report pave the way for moving forward the performance-based design and assessment of tunnel structures for fire. The framework for the design process or evaluation of performance is available; however, limited guidance exists on the required performance criteria (i.e., thresholds for different levels of damage) to characterize losses. The next research step should investigate damage thresholds and the corresponding repair strategies for structural fire analysis of tunnels and downtime assessment of critical infrastructure.

REFERENCES

[1] F. Lu, "On the prediction of concrete spalling under fire," Ph.D. Doctoral Thesis, Dept. of Civil, Environmental and Geomatic Engineering, ETH-Zürich, Zurich, Switzerland, 23092, 2015.

[2] D. Schütz, "Fire protection in tunnels: Focus on road & train tunnels," *Tech. Newsl. SCOR Glob. P&C,* 2014.

[3] K. Fridolf, D. Nilsson, and H. Frantzich, "Fire Evacuation in Underground Transportation Systems: A Review of Accidents and Empirical Research," *Fire Technology,* vol. 49, no. 2, pp. 451-475, 2013/04/01 2013.

[4] EFNARC, "Guidelines for testing of passive fire protection for concrete tunnels linings," 2006.

[5] *NFPA 502 - standard for road tunnels, bridges, and other limited access highways*, 2017.

[6] I. Maevski, "Design fires in road tunnels - a synthesis of highway practice," in "NCHRP Synthesis 415," 2011.

[7] Y. Z. Li and H. Ingason, "The maximum ceiling gas temperature in a large tunnel fire," *Fire Safety Journal,* vol. 48, pp. 38-48, 2012.

[8] Y. Z. Li, B. Lei, and H. Ingason, "The maximum temperature of buoyancy-driven smoke flow beneath the ceiling in tunnel fires," *Fire Safety Journal,* vol. 46, no. 4, pp. 204-210, 2011.

[9] C.-G. Han, Y.-S. Hwang, S.-H. Yang, and N. Gowripalan, "Performance of spalling resistance of high performance concrete with polypropylene fiber contents and lateral confinement," *Cement and concrete research,* vol. 35, no. 9, pp. 1747-1753, 2005.

[10] G.-F. Peng, W.-W. Yang, J. Zhao, Y.-F. Liu, S.-H. Bian, and L.-H. Zhao, "Explosive spalling and residual mechanical properties of fiber-toughened high-performance concrete subjected to high temperatures," *Cement and Concrete Research,* vol. 36, no. 4, pp. 723-727, 2006.

[11] F. Sultangaliyeva, B. Fernandes, H. Carré, P. Pimienta, C. La Borderie, and N. Roussel, "Experimental contribution to the optimization of the choice of polypropylene fibers in concrete for its thermal stability," presented at the 6th International Workshop on Concrete Spalling due to Fire Exposure, Sheffield, United Kingdom, 19–20 September 2019, 2019.

[12] M. Zeiml, D. Leithner, R. Lackner, and H. A. Mang, "How do polypropylene fibers improve the spalling behavior of in-situ concrete?," *Cement and concrete research,* vol. 36, no. 5, pp. 929-942, 2006.

[13] W. Kusterle *et al.*, "Fire resistance of fibre-reinforced, reinforced and prestressed concrete," *Bundesministerium für verkher, innovation und technologie,* no. 544, 2004.

[14] A. Caner and A. Böncü, "Structural fire safety of circular concrete railroad tunnel linings," *Journal of structural engineering,* vol. 135, no. 9, pp. 1081-1092, 2009.

[15] Z. Yan, Y. Shen, H. Zhu, X. Li, and Y. Lu, "Experimental investigation of reinforced concrete and hybrid fibre reinforced concrete shield tunnel segments subjected to elevated temperature," *Fire Safety Journal,* vol. 71, pp. 86-99, 2015.

[16] Z. Yan, H. Zhu, J. W. Ju, and W. Ding, "Full-scale fire tests of RC metro shield TBM tunnel linings," *Construction and Building Materials,* vol. 36, pp. 484-494, 2012.

[17] O. Lalu and T. Lennon, "Experimental investigations into the spalling of high strength concrete and the fire performance of tunnel linings," presented at the 6th International Workshop on Concrete Spalling due to Fire Exposure, Sheffield, United Kingdom, 19–20 September 2019, 2019.

[18] A. Klimek, S. Hothan, and A. Rogge, "Investigation of size effects in concrete spalling," in *6th International Workshop on Concrete Spalling due to Fire Exposure*, Sheffield, United Kingdom, 2019.

[19] D. Pardon *et al.*, "In situ concrete spalling risk assessment in tunnel by means of a mobile oil-fired furnace," presented at the 6th International Workshop on Concrete Spalling due to Fire Exposure, Sheffield, United Kingdom, 19–20 September 2019, 2019.

[20] M. Guerrieri, S. Fragomeni, C. Sanabria, W. Lee , and E. Pazmino "Australian large scale structural fire test facility for concrete tunnel linings," presented at the 6th International Workshop on Concrete Spalling due to Fire Exposure, Sheffield, United Kingdom, 19–20 September 2019, 2019.

[21] I. Burgess and S.-S. Huang, "Proceedings of the 6th International Workshop on Concrete Spalling due to Fire Exposure," Sheffield, United Kingdom, 2019: The University of Sheffield.

[22] J.-M. Franssen and T. Gernay, "Modeling structures in fire with SAFIR®: theoretical background and capabilities," *Journal of Structural Fire Engineering,* vol. 8, no. 3, pp. 300-323, 2017.

[23] F.-J. Ulm, P. Acker, and M. Lévy, "The ''Chunnel'' fire. II: analysis of concrete damage," vol. 125, no. 3, pp. 283-289, 1999.

[24] B. Schrefler, P. Brunello, D. Gawin, C. Majorana, and F. Pesavento, "Concrete at high temperature with application to tunnel fire," *Computational mechanics,* vol. 29, no. 1, pp. 43-51, 2002.

[25] K. Savov, R. Lackner, and H. A. Mang, "Stability assessment of shallow tunnels subjected to fire load," *Fire safety journal,* vol. 40, no. 8, pp. 745-763, 2005.

[26] M. Zeiml, R. Lackner, F. Pesavento, and B. A. Schrefler, "Thermo-hydro-chemical couplings considered in safety assessment of shallow tunnels subjected to fire load," *Fire safety journal,* vol. 43, no. 2, pp. 83-95, 2008.

[27] C. Feist, M. Aschaber, and G. Hofstetter, "Numerical simulation of the load-carrying behavior of RC tunnel structures exposed to fire," *Finite elements in analysis design,* vol. 45, no. 12, pp. 958-965, 2009.

[28] G. Lilliu and A. Meda, "Nonlinear phased analysis of reinforced concrete tunnels under fire exposure," *Journal of Structural Fire Engineering,* 2013.

[29] Z. Sun, Y. Zhang, Y. Yuan, and H. A. Mang, "Stability analysis of a fire-loaded shallow tunnel by means of a thermo-hydro-chemo-mechanical model and discontinuity layout

optimization," *International Journal for Numerical Analytical Methods in Geomechanics,* vol. 43, no. 16, pp. 2551-2564, 2019.
[30] *Assessment, design and repair of fire-damaged concrete structures*, 2008.
[31] *Fire design of concrete structures – structural behavior and assessment*, 2008.
[32] L. Bisby, H. Mostafaei, and P. Pimienta, "White paper on fire resistance of concrete structures," US Department of Commerce, National Institute of Standards and Technology2014.
[33] *Report on nondestructive test methods for evaluation of concrete in structures* 2013.
[34] Joakim Albrektsson, Mathias Flansbjer, J. E. Lindqvist, and R. Jansson, "Assessment of concrete structures after fire," SP Technical Research Institute of Sweden2011, vol. 19.
[35] V. M. Malhotra and N. J. Carino, *Handbook on nondestructive testing of concrete*. CRC press, 2003.
[36] *ASTM C805-18 Standard test method for rebound number of hardened concrete*, 2018.
[37] *ASTM C597-16 Standard test method for pulse velocity through concrete*, 2016.
[38] R. Felicetti, "Assessment methods of fire damages in concrete tunnel linings," *Fire Technology,* no. 49, pp. 509–529, 2013.
[39] N.-D. Hoang, Q.-L. Nguyen, and X.-L. Tran, "Automatic Detection of Concrete Spalling Using Piecewise Linear Stochastic Gradient Descent Logistic Regression and Image Texture Analysis," *Complexity,* vol. 2019, p. 5910625, 2019/07/16 2019.
[40] J. Ingham, "Forensic engineering of fire-damaged structures," *Proceedings of the Institution of Civil Engineers – Civil Engineering,* no. 162, pp. 12-17, 2009.
[41] *ASTM C856M - 20 Standard test method for petrographic examination of hardened concrete*, 2020.
[42] J. Gehandler, H. Ingason, A. Lönnermark, H. Frantzich, and M. Strömgren, "Performance-based design of road tunnel fire safety: Proposal of new Swedish framework," *Case Studies in Fire Safety,* vol. 1, pp. 18-28, 2014.
[43] R. O. Carvel, A. N. Beard, and P. W. Jowitt, "The influence of longitudinal ventilation systems on fires in tunnels," *Tunnelling and Underground Space Technology,* vol. 16, no. 1, pp. 3-21, 2001/01/01/ 2001.
[44] M. K. Cheong, M. Spearpoint, and C. Fleischmann, *Design fires for vehicles in road tunnels*. 2008.
[45] Q. Meng and X. Qu, "A probabilistic quantitative risk assessment model for fire in road tunnels with parameter uncertainty," *Int. J. of Reliability and Safety,* vol. 5, pp. 285-298, 07/01 2011.
[46] K. McGrattan, S. Hostikka, R. McDermott, J. Floyd, C. Weinschenk, and K. Overholt, "Fire dynamics simulator user's guide," *NIST special publication,* vol. 1019, no. 6, 2013.
[47] H. Ingason, Y. Z. Li, and A. Lönnermark, *Tunnel fire dynamics*. New York, NY: Springer, 2014.
[48] P. C. o. R. Tunnels;, "Fire and smoke control in road tunnels," Paris, France05.05.BEN, 1999.
[49] G. T. Atkinson and Y. Wu, "Smoke control in sloping tunnels," *Fire safety journal,* vol. 27, no. 4, pp. 335-341, 1996.

[50] W. Chow, K. Wong, and W. Chung, "Longitudinal ventilation for smoke control in a tilted tunnel by scale modeling," *Tunnelling and Underground Space Technology,* vol. 25, no. 2, pp. 122-128, 2010.
[51] Y. Oka and G. T. Atkinson, "Control of smoke flow in tunnel fires," *Fire Safety Journal,* vol. 25, no. 4, pp. 305-322, 1995.
[52] K. McGrattan and A. Hamins, *Numerical simulation of the Howard Street Tunnel fire, Baltimore, Maryland, July 2001*. Spent Fuel Project Office, Office of Nuclear Material Safety and Safeguards, 2003.
[53] K. McGrattan and A. Hamins, "Numerical simulation of the Howard Street Tunnel fire," *Fire Technology,* vol. 42, no. 4, pp. 273-281, 2006.
[54] (Jan, 20, 2019). *CSX Transportation tunnels*. Available: https://en.wikipedia.org/wiki/Category:CSX_Transportation_tunnels
[55] (Jan, 20, 2019). *Amtrak tunnels*. Available: https://en.wikipedia.org/wiki/Category:Amtrak_tunnels
[56] R. O. Carvel, "Fire size in tunnels," Doctor of Philosophy, School of the Built Environment, Division of Civil Engineering, Heriot-Watt University, Riccarton, Edinburgh, UK, 2004.
[57] R. O. Carvel, A. N. Beard, and P. W. Jowitt, "Fire spread between vehicles in tunnels: effects of tunnel size, longitudinal ventilation and vehicle spacing," *Fire Technology,* vol. 41, no. 4, pp. 271-304, 2005.
[58] A. Lönnermark and H. Ingason, "Recent achievements regarding heat release and temperatures during fires in tunnels," in *Safety in Infrastructure-Svédületes!, Budapest 20th-21st October 2004*, 2004.
[59] B. Y. Lattimer and M. McKinnon, "A review of fire growth and fully developed fires in railcars," *Fire and Materials,* vol. 42, no. 6, pp. 603-619, 2018.
[60] A. Lönnermark, A. Claesson, J. Lindström, Y. Z. Li, M. Kumm, and H. Ingason, "Full-scale fire tests with a commuter train in a tunnel," in "SP Report," SP Technical Research Institute of Sweden2012.
[61] S. Stahlanwendung, "Fires in transport tunnels: report on fullscale tests," *EUREKA Project EU 499 FIRETUN,* vol. 549, 1995.
[62] D. Lee, W.-H. Park, J. Hwang, and G. Hadjisophocleous, "Full-Scale Fire Test of an Intercity Train Car," *Fire Technology,* vol. 52, 04/08 2015.
[63] Y. Li and H. Ingason, "A new methodology of design fires for train carriages based on exponential curve method," *Fire Technology,* vol. 52, 02/28 2015.
[64] P. C. o. R. Tunnels;, "Road tunnels: operational strategies for emergency ventilation," Paris. France2011R02EN, 2011.
[65] P. C. o. R. Tunnels;, "Design fire characteristics for road tunnels ", Paris, France2017R01EN, 2017.
[66] S. R. Lee and H. S. Ryou, "An experimental study of the effect of the aspect ratio on the critical velocity in longitudinal ventilation tunnel fires," *Journal of Fire Sciences,* vol. 23, no. 2, pp. 119-138, 2005.
[67] Y. Z. Li, B. Lei, and H. Ingason, "Study of critical velocity and backlayering length in longitudinally ventilated tunnel fires," *Fire safety journal,* vol. 45, no. 6-8, pp. 361-370, 2010.

[68] J. S. Roh, H. S. Ryou, D. H. Kim, W. S. Jung, and Y. J. Jang, "Critical velocity and burning rate in pool fire during longitudinal ventilation," *Tunnelling and Underground Space Technology,* vol. 22, no. 3, pp. 262-271, 2007.

[69] F. Tanaka, K. Takezawa, Y. Hashimoto, and K. A. Moinuddin, "Critical velocity and backlayering distance in tunnel fires with longitudinal ventilation taking thermal properties of wall materials into consideration," *Tunnelling and Underground Space Technology,* vol. 75, pp. 36-42, 2018.

[70] M. Weng, X. Lu, F. Liu, X. Shi, and L. Yu, "Prediction of backlayering length and critical velocity in metro tunnel fires," *Tunnelling and Underground Space Technology,* vol. 47, pp. 64-72, 2015.

[71] Y. Wu and M. A. Bakar, "Control of smoke flow in tunnel fires using longitudinal ventilation systems–a study of the critical velocity," *Fire Safety Journal,* vol. 35, no. 4, pp. 363-390, 2000.

[72] H. Ingason, Y. Z. Li, and A. Lönnermark, "Runehamar tunnel fire tests," *Fire Safety Journal,* vol. 71, pp. 134-149, 2015.

[73] T. Lemaire, "Runehamar tunnel fire tests: radiation, fire spread and back layering," in "International Symposium on Catastrophic Tunnel Fires (CTF), SP Report ", Borås, Sweden0284-5172, 20–21 November, 2003 2004, vol. 2004:05.

[74] Y. Z. Li, H. Ingason, and A. Lönnermark, "Numerical simulation of Runehamar tunnel fire tests," presented at the 6th International Conference Tunnel Safety and Ventilation, Graz, Austria, 2012.

[75] A. Andreini, R. Da Soghe, B. Facchini, and A. Giusti, "Fire scenarios modelling for the safe design of a passenger rail carriage," in *9th World Congress of Railway Research*, Lille, France, 2011.

[76] G. P. Forney, "Smokeview (version 5)-a tool for visualizing fire dynamics simulation data, volume I: User's guide," 2017.

[77] K. A. Giblin, "The memorial tunnel fire ventilation test program," *ASHRAE Journal,* vol. 39, no. 2, p. 26, 1997.

[78] S. F. Luchian. (1997) Memorial Tunnel Fire Test Program. *TR News*.

[79] Massachusetts Highway Department and Federal Highway Administration, "Memorial Tunnel Fire Ventilation Test Program: test report," in "Central Artery/ Tunnel Project," 1995.

[80] Ministry of Transportation and Public Works of the Netherlands, "Evaluation of Memorial Tunnel CFD simulations " Ministry of Transportation and Public Works of the Netherlands, Netherlands1999.

[81] J. Risher and S. Rhodes, "Toxicological profile for fuel oils," U.S. Department of Health and Human Services, Public Health Service, Agency for Toxic Substances and Disease Registry, Atlanta, Georgia, USJune 1995 1995.

[82] E. Kim, J. P. Woycheese, and N. A. Dembsey, "Fire dynamics simulator (version 4.0) simulation for tunnel fire scenarios with forced, transient, longitudinal ventilation flows," *Fire Technology,* vol. 44, no. 2, pp. 137-166, 2008.

[83] M. J. Hurley *et al.*, *SFPE handbook of fire protection engineering*. Springer, 2015.

[84] (Dec. 2018). *Superliner (railcar)*. Available: https://en.wikipedia.org/wiki/Superliner_(railcar)
[85] *Tunnel Operations, Maintenance, Inspection, and Evaluation (TOMIE) Manual*, 2015.
[86] *Assessing the condition and repair alternatives of fire-exposed concrete and masonry members*, 1994.
[87] S. Du, Y. Zhang, Q. Sun, W. Gong, J. Geng, and K. Zhang, "Experimental study on color change and compression strength of concrete tunnel lining in a fire," *Tunnelling and Underground Space Technology,* vol. 71, pp. 106-114, 2018/01/01/ 2018.
[88] I. Hager, "Colour change in heated concrete," *Fire Technology,* vol. 49, 07/01 2013.
[89] G. Khoury, "Effect of fire on concrete and concrete structures," *Progress in Structural Engineering and Materials,* vol. 2, pp. 429-447, 10/01 2000.
[90] F. Ali, D. O'Connor, and A. Abu-Tair, "Explosive spalling of high-strength concrete columns in fire," *Magazine of Concrete Research,* vol. 53, no. 3, pp. 197-204, 2001.
[91] M. Dwaikat and V. Kodur, "Response of restrained concrete beams under design fire exposure," *Journal of Structural Engineering,* vol. 135, no. 11, pp. 1408-1417, 2009.
[92] R. Jansson and L. Boström, "Factors influencing fire spalling of self compacting concrete," *Materials and structures,* vol. 46, no. 10, pp. 1683-1694, 2013.
[93] V. Kodur, "Spalling in high strength concrete exposed to fire: concerns, causes, critical parameters and cures," in *Advanced Technology in Structural Engineering*, 2000, pp. 1-9.
[94] V. Kodur, T. Wang, and F. Cheng, "Predicting the fire resistance behaviour of high strength concrete columns," *Cement and Concrete Composites,* vol. 26, no. 2, pp. 141-153, 2004.
[95] L. T. Phan, J. R. Lawson, and F. L. Davis, "Effects of elevated temperature exposure on heating characteristics, spalling, and residual properties of high performance concrete," *Materials and structures,* vol. 34, no. 2, pp. 83-91, 2001.
[96] D. Gawin, F. Pesavento, and B. Schrefler, "Towards prediction of the thermal spalling risk through a multi-phase porous media model of concrete," *Computer methods in applied mechanics and engineering,* vol. 195, no. 41-43, pp. 5707-5729, 2006.
[97] B. Lottman, E. Koenders, C. Blom, and J. Walraven, "Spalling of concrete due to fire exposure: A coupled fracture mechanics and pore pressure approach," in *MATEC Web of Conferences*, 2013, vol. 6, p. 05002: EDP Sciences.
[98] J. Ožbolt and J. Bošnjak, "Modelling explosive spalling and stress induced thermal strains of HPC exposed to high temperature," in *MATEC Web of Conferences*, 2013, vol. 6, p. 05003: EDP Sciences.
[99] M. B. Dwaikat and V. Kodur, "Hydrothermal model for predicting fire-induced spalling in concrete structural systems," *Fire safety journal,* vol. 44, no. 3, pp. 425-434, 2009.
[100] Q. Ma, R. Guo, Z. Zhao, Z. Lin, and K. He, "Mechanical properties of concrete at high temperature—A review," *Construction and Building Materials,* vol. 93, pp. 371-383, 2015.
[101] L. Boström and R. J. McNamee, "Proceedings of the 5th International Workshop on Concrete Spalling due to Fire Exposure," Borås, Sweden, 2017: RISE Research Institutes of Sweden.
[102] E. Klingsch, A. Frangi, and M. Fontana, "Explosive spalling of concrete in fire " Institut für Baustatik und Konstruktion der ETH Zürich2013, vol. 351.

[103] M. Maier and R. Lackner, "Experimental investigation on spalling behavior of concrete: damage level and moisture movement," presented at the 5th International Workshop on Concrete Spalling due to Fire Exposure, Borås, Sweden, 12-13 October 2017, 2017.
[104] K. H. Mróz, Izabela; Tekieli,Marcin, "Effect of cold rim on extent and type of concrete fire spalling," presented at the 5th International Workshop on Concrete Spalling due to Fire Exposure, Borås, Sweden, 12-13 October 2017, 2017.
[105] S. Buch and U. Kumar Sharma, "Fire resistance and spalling performance of eccentrically loaded reinforced concrete columns," presented at the 5th International Workshop on Concrete Spalling due to Fire Exposure, Borås, Sweden, 12-13 October 2017, 2017.
[106] M. J. L. M. Miah, Francesco; Felicetti, Roberto, "Experimental investigation on fire spalling behaviour of concrete: effect of biaxial compressive loading and cement type," presented at the 5th International Workshop on Concrete Spalling due to Fire Exposure, Borås, Sweden, 12-13 October 2017, 2017.
[107] F. Lo Monte, R. Felicetti, A. Meda, and A. Bortolussi, "Influence of the test method in the assessment of concrete sensitivity to explosive spalling," presented at the 5th International Workshop on Concrete Spalling due to Fire Exposure, Borås, Sweden, 12-13 October 2017, 2017.
[108] R. J. McNamee *et al.*, "Screening test methods for determination of fire spalling of concrete – an international comparison," presented at the 5th International Workshop on Concrete Spalling due to Fire Exposure, Borås, Sweden, 12-13 October 2017, 2017.
[109] M. Ozawa, T. Tanibe, M. Kanematsu, and T. Morita, "Screening-test analysis of fire spalling behavior with various concrete samples," presented at the 5th International Workshop on Concrete Spalling due to Fire Exposure, Borås, Sweden, 12-13 October 2017, 2017.
[110] M. Schneider and A. Šajna, "Experimental study of the spalling behaviour of ultra-high performance fibre reinforced concrete during fire," presented at the 6th International Workshop on Concrete Spalling due to Fire Exposure, Sheffield, United Kingdom, 19–20 September 2019, 2019.
[111] *Eurocode 2: Design of concrete structures*, 2004.
[112] T. Gernay and J. M. Franssen, "A formulation of the Eurocode 2 concrete model at elevated temperature that includes an explicit term for transient creep," *Fire Safety Journal,* vol. 51, pp. 1-9, 2012/07/01/ 2012.
[113] N. Elhami-Khorasani, J. Billittier, and A. Stavridis, "Structural performance of a railway tunnel under different fire scenarios," in *2018 Joint Rail Conference*, 2018, pp. V001T06A006-V001T06A006: American Society of Mechanical Engineers.
[114] C. Pichler, R. Lackner, and H. A. Mang, "Safety assessment of concrete tunnel linings under fire load," *Journal of Structural Engineering,* vol. 132, no. 6, pp. 961-969, 2006.
[115] O. Arioz, "Effects of elevated temperatures on properties of concrete," *Fire Safety Journal,* vol. 42, no. 8, pp. 516-522, 2007/11/01/ 2007.
[116] Y. N. Chan, G. F. Peng, and M. Anson, "Residual strength and pore structure of high-strength concrete and normal strength concrete after exposure to high temperatures," *Cement and Concrete Composites,* vol. 21, no. 1, pp. 23-27, 1999/01/01/ 1999.

[117] T. Gernay, "Fire resistance and burnout resistance of reinforced concrete columns," *Fire Safety Journal,* vol. 104, pp. 67-78, 2019/03/01/ 2019.
[118] J.-C. Mindeguia, P. Pimienta, H. Carré, and C. L. Borderie, "Experimental analysis of concrete spalling due to fire exposure," *European Journal of Environmental and Civil Engineering,* vol. 17, no. 6, pp. 453-466, 2013/06/01 2013.
[119] C. Féron, P. Autuori, and D. Joyeux, "Vers des moyens de prévenir l'écaillage du béton en [Means for preventing concrete spalling in tunnels]," *Tunnels et Ouvrages Souterrains,* vol. 196, pp. 228-235, 2006.
[120] G. Lee, D. Han, M.-C. Han, C.-G. Han, and H.-J. Son, "Combining polypropylene and nylon fibers to optimize fiber addition for spalling protection of high-strength concrete," *Construction and Building Materials,* vol. 34, pp. 313-320, 2012/09/01/ 2012.
[121] M. R. Bangi and T. Horiguchi, "Effect of fibre type and geometry on maximum pore pressures in fibre-reinforced high strength concrete at elevated temperatures," *Cement and Concrete Research,* vol. 42, no. 2, pp. 459-466, 2012/02/01/ 2012.
[122] M. Ozawa and H. Morimoto, "Effects of various fibres on high-temperature spalling in high-performance concrete," *Construction and Building Materials,* vol. 71, pp. 83-92, 2014/11/30/ 2014.
[123] X. H. Wang, S. Jacobsen, J. Y. He, Z. L. Zhang, S. F. Lee, and H. L. Lein, "Application of nanoindentation testing to study of the interfacial transition zone in steel fiber reinforced mortar," *Cement and Concrete Research,* vol. 39, no. 8, pp. 701-715, 2009/08/01/ 2009.
[124] V. K. R. Kodur and L. Phan, "Critical factors governing the fire performance of high strength concrete systems," *Fire Safety Journal,* vol. 42, no. 6, pp. 482-488, 2007/09/01/ 2007.
[125] K. D. Hertz, "Limits of spalling of fire-exposed concrete," *Fire Safety Journal,* vol. 38, no. 2, pp. 103-116, 2003/03/01/ 2003.
[126] F. Ali, A. Nadjai, and A. Abu-Tair, "Explosive spalling of normal strength concrete slabs subjected to severe fire," *Materials and Structures,* vol. 44, no. 5, pp. 943-956, 2011/06/01 2011.
[127] Y. Li, K. H. Tan, and E.-H. Yang, "Influence of aggregate size and inclusion of polypropylene and steel fibers on the hot permeability of ultra-high performance concrete (UHPC) at elevated temperature," *Construction and Building Materials,* vol. 169, pp. 629-637, 2018/04/30/ 2018.
[128] Efectis, "Fire testing procedure for concrete tunnel linings and other tunnel components," Efectis Netherland BV, Netherland2020, vol. R0695:2020.
[129] EFNARC, "Specification and guidelines for testing of passive fire protection for concrete tunnels linings," EFNARC2006.
[130] *ASTM A 615/A 615M - Standard Specification for Deformed and Plain Billet Steel Bars for Concrete Reinforcement*, 2002.
[131] *ASTM A416 / A416M-18, Standard Specification for Low-Relaxation, Seven-Wire Steel Strand for Prestressed Concrete*, 2018.
[132] J. Chabronova, M. Bednar, and J. Snopko, "Analysis of Permanent Lining of Branisko Tunnel," in *Key Engineering Materials*, 2017, vol. 738, pp. 249-260: Trans Tech Publ.

[133] M. Briffaut, F. Benboudjema, and L. D'aloia, "Effect of fibres on early age cracking of concrete tunnel lining. Part II: numerical simulations," *Tunnelling and Underground Space Technology,* vol. 59, pp. 221-229, 2016.

[134] M. Corigliano, L. Scandella, C. G. Lai, and R. Paolucci, "Seismic analysis of deep tunnels in near fault conditions: a case study in Southern Italy," *Bulletin of Earthquake Engineering,* vol. 9, no. 4, pp. 975-995, 2011.

[135] X. Cui *et al.*, "Dynamic responses and damage analyses of tunnel lining and errant large vehicle during collision," *Tunnelling and Underground Space Technology,* vol. 50, pp. 1-12, 2015.

[136] N. A. Do, D. Dias, P. Oreste, and I. Djeran-Maigre, "A new numerical approach to the hyperstatic reaction method for segmental tunnel linings," *International Journal for Numerical Analytical Methods in Geomechanics,* vol. 38, no. 15, pp. 1617-1632, 2014.

[137] N.-A. Do, D. Dias, P. Oreste, and I. Djeran-Maigre, "2D numerical investigation of segmental tunnel lining behavior," *Tunnelling and Underground Space Technology,* vol. 37, pp. 115-127, 2013.

[138] G. D. Hatzigeorgiou and D. E. Beskos, "Soil–structure interaction effects on seismic inelastic analysis of 3-D tunnels," *Soil Dynamics and Earthquake Engineering,* vol. 30, no. 9, pp. 851-861, 2010.

[139] P. Spyridis and K. Bergmeister, "Analysis of lateral openings in tunnel linings," *Tunnelling and Underground Space Technology,* vol. 50, pp. 376-395, 2015.

[140] C. Zhao, A. A. Lavasan, T. Barciaga, C. Kämper, P. Mark, and T. Schanz, "Prediction of tunnel lining forces and deformations using analytical and numerical solutions," *Tunnelling and Underground Space Technology,* vol. 64, pp. 164-176, 2017.

[141] R. Tiwari, T. Chakraborty, and V. Matsagar, "Dynamic analysis of tunnel in weathered rock subjected to internal blast loading," *Rock Mechanics and Rock Engineering,* vol. 49, no. 11, pp. 4441-4458, 2016.

[142] T.-H. Lee, D. Park, D. D. Nguyen, and J.-S. Park, "Damage analysis of cut-and-cover tunnel structures under seismic loading," *Bulletin of Earthquake Engineering,* vol. 14, no. 2, pp. 413-431, 2016.

[143] G. P. Kouretzis, K. I. Andrianopoulos, S. W. Sloan, and J. P. Carter, "Analysis of circular tunnels due to seismic P-wave propagation, with emphasis on unreinforced concrete liners," *Computers and Geotechnics,* vol. 55, pp. 187-194, 2014.

[144] S. Kontoe, V. Avgerinos, and D. Potts, "Numerical validation of analytical solutions and their use for equivalent-linear seismic analysis of circular tunnels," *Soil Dynamics and Earthquake Engineering,* vol. 66, pp. 206-219, 2014.

[145] K. Lin, H. Hung, J. P. Yang, and Y. Yang, "Seismic analysis of underground tunnels by the 2.5 D finite/infinite element approach," *Soil Dynamics and Earthquake Engineering,* vol. 85, pp. 31-43, 2016.

[146] P. Spyridis, S. Konstantis, A. J. G. Gakis, and Tunnelling, "Performance indicator of tunnel linings under geotechnical uncertainty," *Geomechanics and Tunnelling,* vol. 9, no. 2, pp. 158-164, 2016.

[147] H.-w. Huang and D.-m. Zhang, "Resilience analysis of shield tunnel lining under extreme surcharge: Characterization and field application," *Tunnelling and Underground Space Technology*, vol. 51, pp. 301-312, 2016/01/01/ 2016.

[148] Y. Shen, B. Gao, X. Yang, and S. Tao, "Seismic damage mechanism and dynamic deformation characteristic analysis of mountain tunnel after Wenchuan earthquake," *Engineering Geology*, vol. 180, pp. 85-98, 2014.

[149] W. Zhang, X. Jin, and Z. Yang, "Combined equivalent & multi-scale simulation method for 3-D seismic analysis of large-scale shield tunnel," *Engineering Computations*, 2014.

[150] H. Yu, Y. Yuan, Z. Qiao, Y. Gu, Z. Yang, and X. Li, "Seismic analysis of a long tunnel based on multi-scale method," *Engineering Structures*, vol. 49, pp. 572-587, 2013.

[151] M. Bakhshi and V. Naeri, "Design of segmental tunnel linings for serviceability limit state," presented at the "SEE Tunnel: Promoting Tunneling in SEE Region" ITA WTC 2015 Congress and 41st General Assembly, Dubrovnik, Croatia, May 22-28, 2015.

[152] E. W. Klingsch, "Explosive spalling of concrete in fire," Institut für Baustatik u. Konstruktion / Institute of Structural Engineering2014, vol. 356.

[153] P. Kalifa, G. Chéné, and C. Gallé, "High-temperature behaviour of HPC with polypropylene fibres: From spalling to microstructure," *Cement and Concrete Research*, vol. 31, no. 10, pp. 1487-1499, 2001/10/01/ 2001.

[154] C. Maluk, L. Bisby, and G. P. Terrasi, "Effects of polypropylene fibre type and dose on the propensity for heat-induced concrete spalling," *Engineering Structures*, vol. 141, pp. 584-595, 2017/06/15/ 2017.

[155] G. Khoury, "Polypropylene fibres in heated concrete. Part 2: Pressure relief mechanisms and modelling criteria," *Magazine of Concrete Research - MAG CONCR RES*, vol. 60, pp. 189-204, 01/04 2008.

[156] *Eurocode: Design of Concrete Structures – Parts 1–2: General rules –Structural Fire Design (EN 1992-1-2)*, 2004.

[157] CCAA., "Fire Safety of Concrete Buildings. Cement Concrete & Aggregates," Australia (CCAA), Australia2013.

[158] M. Ozawa, M. Sukekawa, and H. Akasaka, "Investigation of the preventive effect on fire spalling of natural jute fibre in high performance concrete through ring-restrained specimen tests," in *6th International Workshop on Concrete Spalling due to Fire Exposure*, Sheffield, United Kingdom, 2019.

[159] J. Kirnbauer, "Spalling behaviour of UHPC with modified microstructure due to fire load," in *6th International Workshop on Concrete Spalling due to Fire Exposure*, Sheffield, United Kingdom, 2019.

[160] Y. Du and H. Qi, "Prevent high strength concrete from spalling subject to ISO834 fire," presented at the 6th International Workshop on Concrete Spalling due to Fire Exposure, Sheffield, United Kingdom, 19–20 September 2019, 2019.

[161] J. Reiners and C. Müller, "Influence of the chemical and physical properties of hardened cement paste on the fire-induced spalling of concrete," presented at the 6th International Workshop on Concrete Spalling due to Fire Exposure, Sheffield, United Kingdom, 19–20 September 2019, 2019.

[162] L. Stelzner, F. Weise, T. Oesch, R. Dlugosch, and B. Powierza, "Transport and reconfiguration of moisture in HPC due to unilateral heating," presented at the 6th International Workshop on Concrete Spalling due to Fire Exposure, Sheffield, United Kingdom, 19–20 September 2019, 2019.
[163] F. Sultangaliyeva, C. Leang, H. Carré, C. La Borderie, and N. Roussel, "Experimental and numerical study of the influence of the PP fiber diameter on spalling behaviour of concrete," presented at the 6th International Workshop on Concrete Spalling due to Fire Exposure, Sheffield, United Kingdom, 19–20 September 2019, 2019.
[164] (Jan, 20, 2020). *Baltimore Harbor Tunnel*. Available: https://en.wikipedia.org/wiki/Category:CSX_Transportation_tunnels
[165] P. B. Knuvers, "Crack width in Tunnels," Delft University of Technology2018.
[166] B. Chen, C. Li, and L. Chen, "Experimental study of mechanical properties of normal-strength concrete exposed to high temperatures at an early age," *Fire Safety Journal*, vol. 44, no. 7, pp. 997-1002, 2009/10/01/ 2009.